

For New Technology Network

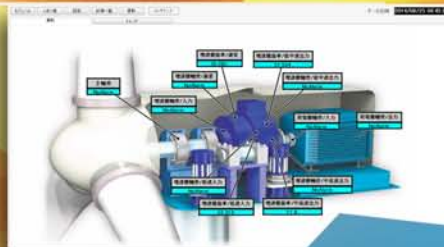
NTN®

TECHNICAL REVIEW

No.
82

**Special Issue; Composite Material,
Technology and Products
for Industrial Machines**

October 2014



Introduction of “WIND LAB.” - Test equipment for ultra-large main shaft bearings for wind power generators

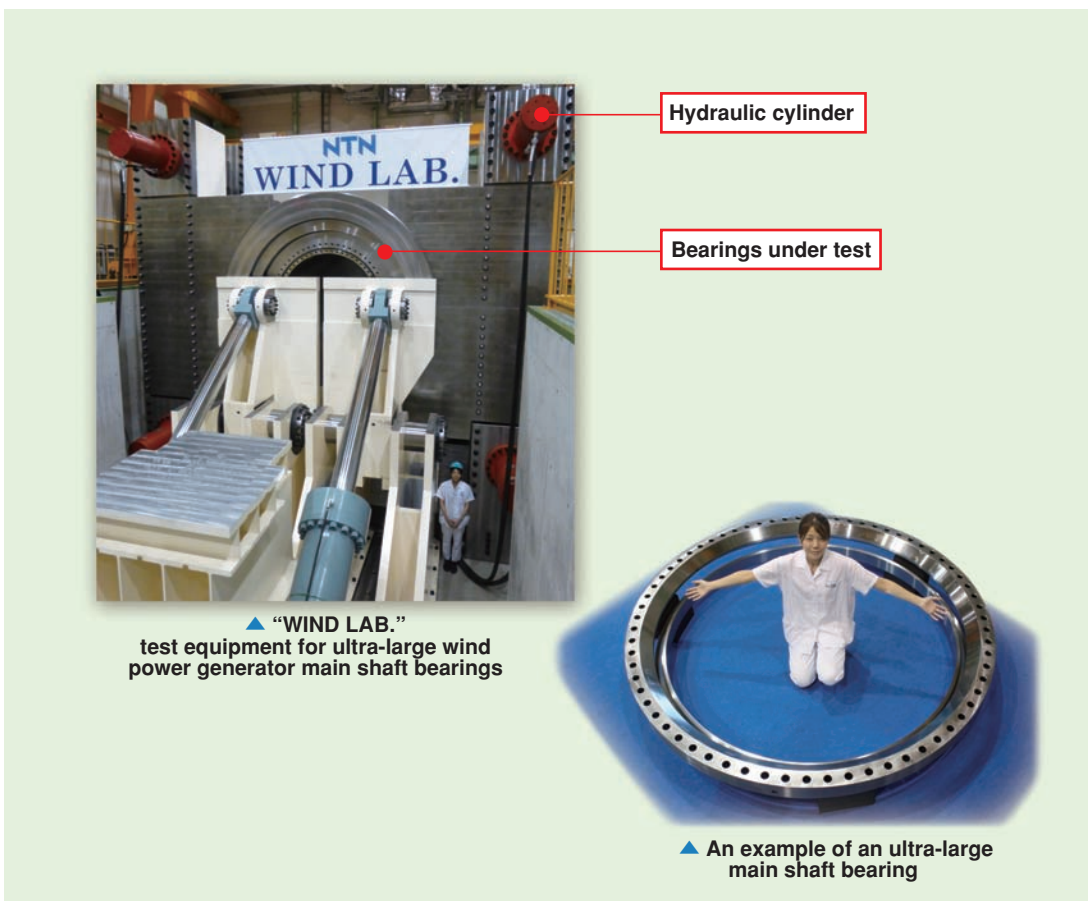
For New Technology Network

NTN has developed the world's largest large-bearing-test apparatus (“WIND LAB.”) which allows evaluation of off-shore wind power generator main shaft bearings with an outer diameter of up to 4.2m. This will enhance our ability to develop technology to cope with increasing demand around the world. NTN introduced the equipment at the Advanced Technology R&D Center (Kuwana-shi, Mie-ken).

“WIND LAB.” applies loading to the bearings with a total of 6 hydraulic cylinders, in vertical and horizontal directions, to simulate the actual conditions experienced by a wind turbine. This enables detailed technological analysis and specification review of bearings selected for large wind power generator applications. In addition to enabling evaluation of the load conditions in the stationary or extreme state, it can also support various types of bearings, such as self-aligning roller bearings and tapered roller bearings, so that the customers can conduct tests tailored to their needs.

NTN develops and provides all kinds of bearings used in the components of wind power generators including main bearings, final gears, step-up gears, and generators. Wind power generators, including those for off-shore use, are increasing in size, and main shaft bearings require advanced technology to support rotation of blades, which can exceed 100 m in diameter. Therefore, evaluating the actual ultra-large bearings will help accelerate development and improve bearing reliability. In addition, we will aim to monitor the bearing conditions during the test by integrating the condition monitoring system (CMS) for wind power generators developed by NTN (“WindDoctor®”- page 74). Our objective is to improve the functionality of the bearings while continuing to further enhance the equipment diagnostic technology of CMS.

We will strive to enhance our advantage as a bearing manufacturer by using “WIND LAB.” and further grow our business for wind power generation equipment.





TECHNICAL REVIEW

No.82

**Special Issue: Composite Material,
Technology and Products
for Industrial Machines**

NTN TECHNICAL REVIEW No.82

CONTENTS

Preface	Natsuhiko MORI	1
Contribution	Advanced Powders Processing – Recent Powder Metallurgy Techniques and It's Trend – Hideshi MIURA Professor, Department of Mechanical Engineering, Kyushu University	2
● Special Issue for Composite Material Products and Technology		
	Product Introduction and Complex Technology of Resin,Sintered Metal and Magnet for Growth Markets Yoshio OKI	12
	The Improvement in Strength of Sintered Machine Parts Takahiro OKUNO and Naoki YASHIRO	21
	High Performance Magnetic Core for Induction Hardening Devices Takuji HARANO	26
	The Copper-Iron-based Material Equivalent to Bronze-based Material for Sintered, Oil-impregnated Bearings Tomonori YAMASHITA	30
	High Load Sliding Bearing Unit For Use in Copier and Printer Fusers Kei HATTORI and Takuya ISHII	34
● Special Issue for Manufacturing Technology		
	Machine Tool Main Spindle Bearings with Air Cooling Spacer Yushi ONDA, Kikuo FUKADA, Yohei YAMAMOTO and Masato YOSHINO	38
	New Engineering Plastic Cage of High Speed Angular Contact Ball Bearings for Machine Tools Wakana INOUE, Mineo KOYAMA and Soichiro ONITSUKA	44
	Bearing Technical Calculation System for Machine Tool Spindles Keiichi UEDA, Yushi ONDA and Shouhei HASHIZUME	49
	Estimation Method for Friction Torque of Air-oil Lubricated Angular Contact Ball Bearings Hiroki FUJIWARA	54
	Real-time Monitoring of the Superfinishing Process Kohei HIGASHI, Hajime ISA, Takakazu KITAGAWA, Takashi ONISHI and Kazuhito OHASHI	61
	Lightweight Bearing for Robot Sebastien BRISSON	68
● Special Issue for CMS Supertechnology New Products		
	Development of Condition Monitoring System Keisuke HASHIZUME, Akitoshi TAKEUCHI and Yuzuru TANAKA	74
	Introduction of "ULTAGE" series : High Functionality Roller Bearings Shogo TABATA, Kouhei TODA and Yasuhiko SHIMIZU	78
	Technical Trend of Aircraft Bearings Takashi NISHIKAWA, Nao HAYASHI and Akiko HAYAKAWA	83
● Technical Papers		
	The Influence of the Humidity and Quantity of Hydrogen into Steel under the Abrasive Wear Motohiro ITO	88
	Evaluation of Shear Fatigue Properties of Medium Carbon Steels and Rolling Bearing Steels up to Giga-cycle Regimes Noriaki MIWA	94
● Our Line of Award Winning Products		
	"2013 'CHO' MONODZUKURI Innovate Components Awards" NIPPON Brand Award Parallel Link High Speed Angle Control Equipment Hiroshi ISOBE, Yukihiro NISHIO, Seigo SAKATA, Naoya KONAGAI and Hiroyuki YAMADA	98
	"The Japan Powder Metallurgy Association Awards 2013" New Materials Development of the Oil Seal Made of Sintered Metal for Variable Valve Timing Device Yosuke SUGAI and Toshihiko MOURI	99
	"The Japan Powder Metallurgy Association Awards 2013" Effort Prize Sintered Hydrodynamic Bearing for Super Thin Fan Motor Tadahiro UCHIYAMA and Shinji KOMATSUBARA	100
	"The Japanese Society of Tribologists 2013" Encouragement Award Development of Ultrasonic Torsional Fatigue Tester for Rapid Shear Fatigue Property Evaluation of Rolling Bearing Steels Noriaki MIWA	101
Our Line of New Products		102

*A Message for the Special Issue:
Composite Material, Technology and Products
for Industrial Machine*



Natsuhiko MORI
Executive Officer

As the manufacturing industry is globalized and both the market and demand of products are expanding throughout the world, maximizing the effective use of the minimum resources and paying attention to the global environment has become an urgent issue. In Japan, development and utilization of advanced technologies and materials are accelerating in order to maintain sustainable and constructive competitiveness. Therefore, methods for utilizing materials and some manufacturing methods are about to change significantly. Some examples are the expanded application of CFRP and use of 3D printers.

In view of these circumstances, NTN has formed a new division, the Composite Material Product Division in April, 2011. The purpose of this division is to consolidate and enhance the resin, sintered metal and magnetic material technologies to develop and introduce composite products and unit module products into the market. Then, they can contribute to the fuel efficiency and electric drive of automobiles and high-performance industrial machine components.

At the 27th Japan International Machine Tool Fair (JIMTOF2014), which took place from October 30 to November 4, with the theme “Mono-Zukuri DNA’ connects to the Future and the World”, NTN Technical Review No. 82 was published featuring NTN’s composite material, technology and products for industrial machines.

In this Technical Review, we had a contribution entitled, “Advanced Powders Processing – Recent Powder Metallurgy Techniques and Its Trend” from Professor Hideshi Miura. Professor Hideshi Miura is from the Department of Mechanical Engineering, Kyushu University, and is an authority on powder and powder metallurgy.

In the “Special Issue for Composite Material Products and Technology”, we introduce high-strength sintered metal, magnetic material and resin as well as hybrid products. In the “Special Issue for Manufacturing Technology”, we introduce technology and products that were exhibited at JIMTOF2014, manufactured with our proprietary technology. Finally, in “Special Issue for CMS Supertechnology New Products” we introduce base technology/products and monitoring technology for industrial machines.

At NTN we will celebrate our 100th anniversary in fiscal year 2017. Following our theme, “For New Technology Network: We shall contribute to international society through creating new technologies and developing new products,” we are striving to contribute to development of the industry by utilizing our proprietary technology development capabilities.

For New Technology Network

Advanced Powders Processing

– Recent Powder Metallurgy Techniques and It's Trend –



Hideshi MIURA

Professor, Department of Mechanical Engineering, Kyushu University

Advanced powder processing techniques such as metal injection molding (MIM) are hoped to be suitable for fabricating complex shaped components with low cost. So far, we have applied MIM process to produce various types of industrial materials such as ferrous and Ti alloys, especially heat treated Fe-6Ni-0.4C showed the super high strengthened properties of 2000MPa tensile strength and 8% elongation which are superior to wrought materials. On the other hand, direct laser forming (DLF) technique is another advanced powder processing technique. Recently, much effort has been made to apply this process to automobile, aerospace and medical fields due to the potential of producing complex shaped Ti alloy structures. In this paper, the above two techniques are introduced as recent powder metallurgy techniques.

1. Introduction

Powder metallurgy (P/M) is a metal processing method using a phenomenon called sintering, a process which bonds particles by heat (temperature lower than the melting point) for extracting particular properties from the metal and ceramics powder and plays an important role as one of the manufacturing processes of materials and products in high-industrialized society. Liquid-phase sintering also exists depending on the components. The biggest advantage of P/M is to be able to shape the powder directly into the end product (near net or net shaping) having a significant degree of freedom in material properties, composition, thermal processing and microstructure. This provides properties that cannot be achieved by the melting method. In addition, there is an economical benefit allowing volume production. With these properties, P/M is used to produce various components for machine structural use such as gears, bearings and connecting rods (for automobiles) P/M is also used to produce cutting/abrasion resistant tooling materials such as cemented carbide tip and molding, high melting point metal materials such as W and Mo, porous materials such as filters and implants for living bodies, electric contacts/power collecting materials such as switches and materials for pantograph contact strips, and magnetic materials such as magnetic cores and sensor rings.

Improvement of conventional processes from production of powder, shaping, sintering and post-

processing, as well as development of new technology are well underway for P/M products with high density and high performance. However, recent P/M technologies are focused on machining and composite processing technologies in the boundary areas with other material processing technologies, among others, as shown in [Table 1](#)¹⁾. For example, the powder injection molding is a combination of P/M and plastic molding, and powder lamination 3D printing is a combination of P/M and laser machining (CAD/CAM). Acquiring knowledge and applications of these new technologies should be very useful for manufacturing/development of new materials and products for NTN. In this paper, I will focus on the above two innovative and unique molding/sintering methods, providing an overview of the technologies and introduce you to the recent outcomes of our research as an alternative to providing you with a perspective into the future.

2. Metal Injection Molding

A molding technique that allows both a high degree of freedom for shaping and high density in a relatively easy process has been desirable in P/M. One such technique is the metal injection molding (MIM) process with binder developed in the 1970s.

MIM process is used in many forms however the basic steps are similar to the ones shown in [Fig. 1](#)¹⁾. The typical raw material is nearly round particles of carbonyl and powder produced from oxide reduction

Table 1 Recent applications of various P/M processings

Use	Required properties	Process and materials
Anticorrosive component	True density uniform alloy	HIP, titanium
Thermal process equipment	Carburizing resistance and creep resistance	Reaction sintering, extrusion, nickel aluminide
Fine jewelry/accessories	Good appearance, complex shape	Injection molding, precious metal, titanium
Pipe, thick plate, rod, plate	True density, net shape	Spray forming, steel, super alloy
Magnetic component	Magnetic functionality, ambient resistance	Sintering, injection molding, rapidly solidified powder
Covering material	Oxidation resistance and corrosion resistance	Spray forming, intermetallic compound
Microelectronics board	Adjustment of thermal property, absorption of microwave	Injection molding, W-Cu, Mo-Cu, Al-SiC, Al-AlN
High melting-point metal	Complex shape	Complete densification method such as HIP, special alloy
Aircraft structural material	High relative strength	Complete densification method, rapidly solidified Al alloy
Structural material	Fatigue strength and fracture strength	Powder forging, iron alloy
Dynamic membranel filter	Small pore size, corrosion resistance	CIP, stainless steel
Abrasion-resistant structural material	Lightweight, high abrasion resistance	Hot press, boride, Al based composite material

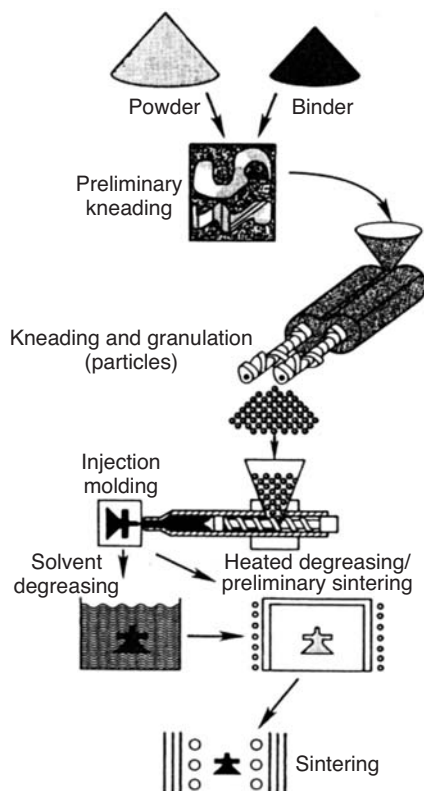


Fig.1 Conceptual sequence of MIM steps

and gas atomization with the average grain size of 0.5 to 15 μm to facilitate densification during sintering. Generally, thermoplastic polymer materials are used as the binder however; water and diverse inorganic materials are also often used. The typical binder consists of 70% of paraffin wax and 30% of polypropylene with an appropriate lubrication and wetting agent to provide adhesiveness to the binder and the powder. This type of binder completely melts at approximately 150°C. The amount of the binder is about 40 vol% of the kneaded material, which is

equivalent to approximately 6 wt% in case of ferrous metal, although the percentage depends on the filling characteristics of the powder. The best shaping can be attained when the viscosity of the kneaded material is 100 Pa · s or less however, the viscosity depends not only on the viscosity of the binder itself but also the temperature of the kneaded material, shear rate, volume of the solids and type of surface wetting agents included in the binder. Good uniformity is required for the kneaded material to maintain good process control. The viscosity, which is sensitive to the composition and variations may also prevent good flow into a mold cavity. Usually, the viscosity of the kneaded material can be kept within the desirable range by slightly adding more binder.

The device used for molding is the same as those used for plastic injection molding. The reciprocal-type screw driven by a motor is used for mixing/kneading the raw material so that the kneaded material becomes uniform, producing the required pressure to fill the kneaded material into the mold. The raw material, in the form of pulverized particles at normal temperature, is introduced from the charging hopper and heated over the melting temperature of the binder as it passes the barrel. The kneaded material of melted powder and binder is pushed forward to instantaneously fill in the mold cavity. After being sufficiently cooled down, the compact is removed and the process is repeated. For better molding, higher pressure or lower viscosity is required. Since the pressure that can be used for the molding machine is limited and the viscosity is governed by the temperature, the main control factors are temperature and pressure for the molding process.

After molding, the binder is removed from the compact by a process called debinding. Many debinding techniques and processes related to different binders have been developed which, together

with the composition of the binders, account for the majority of the patents. **Table 2**²⁾ shows various debinding techniques.

In the industry, thermal decomposition and solvent degreasing are mainly used, however the former still has issues such as long debinding time (slow heating up to 600°C) and possible deformation of the product. The latter has significantly overcome those issues but, many of the solvents such as acetone and ethylene are hazardous to humans and the environment and their handling involves additional problems. Therefore, new binders soluble in ethanol and water are actively under development. At any rate, long debinding time is disadvantageous for production, which considerably limits the permissible thickness of the MIM products. Up until a few years ago, it was considered that a thickness of around 10 mm was the limit from the economical point of view however, with the evolution of debinding technology it is now possible to allow a thickness of around 25 mm. In addition, there are other special techniques such as debinding by catalyst³⁾ and a kind of water freezing technique called Quickset process⁴⁾.

The next step, sintering, is processed under inert, or reduction, atmosphere or vacuum atmosphere, similar to the conventional P/M technique. Sintering creates strong bonding of particles and voids are removed by densification. Isotropic powder filling results in uniform contraction (15–20%) as can be predicted. Therefore, initial compacts are made a little larger so that the final compacts fit the desirable size. After sintering, the compacts show superior strength and uniform composition compared to the characteristics possible with many other manufacturing processes. **Table 3** shows an example of the comparison of mechanical properties of various ferrous sintered materials with this process and other manufacturing processes. The mechanical properties of the MIM process not only exceed the properties of the conventional P/M materials but are also equivalent or superior to the molten materials in any steel types⁵⁾⁻⁹⁾. This indicates that the MIM process is effective for forming materials with hard machining properties, as well as for improving the material properties. The following indicates some of the typical examples from the results of our research.

2.1 Ultra-high strengthening of ferrous sintered materials by MIM process

The author group, from our research, proposed a new precise controlling method of the amount of carbon by atmosphere control in the MIM process. This developed sintered low alloy steel (Fe-2%Ni-0.5%Mo-0.4%C thermal processed material) by the mixed

Table 2 Various debinding techniques

Process name	Binder content	Debinding condition
Heated degreasing		
MACPHERSON process	PE, camphor	Vacuum
WITEC process	WAX, PE	Turbulence, absorber
VI process	WAX, PE, PP	High vacuum, evaporation
(volatile)		
RIVERS process	Water, methyl cellulose	Anhydration within the mold
QUICKSET process	Water, PEG	Freeze dry
Solvent extraction		
WITEC process	PE, PS, PEG	Water, methylene chloride
MACPHERSON process	PE, PS	Trichlene
AMAX process	WAX, PE, PP Peanut oil	Methylene chloride
Chemical decomposition		
BASF process	Modified Polyacetal	Nitric acid, oxalic acid vapor
UV decomposition process	WAX, acryl	UV irradiation

PE: polyethylene, PP: polypropylene, PEG: Polyethylene glycol, PS: polystyrene, POM: polyacetal

Table 3 Mechanical properties of various alloy steels by different material processings

Steel type	Mechanical properties	MIM	P/M	Melting method
High-speed steel SKH10 (tempered material)	Deflecting strength (MPa)	3200	2500	2500
	Hardness (H _{RC})	70	71	67
Maraging steel 18Ni-8Co-5Mo (aged material)	Tensile strength (MPa)	1640	1500	1800
	Elongation (%)	2~3	1~2	8
	Hardness (H _{RC})	47	35	
Martensitic stainless steel SUS440C (17Cr-1C) (tempered material)	Tensile strength (MPa)	1600	SUS410 900	1950
	Elongation (%)	1~2	4	2
	Hardness (H _{RC})	53	30	57
17-4PH stainless steel SUS630 (aged material)	Tensile strength (MPa)	1340	970	1370
	Elongation (%)	11	2	14
	Hardness (H _{RC})	44	24	45

powder technique which indicates extremely high mechanical properties (equivalent to sinter forging material) of 1800 MPa tensile strength and elongation of 3-4% which cannot be achieved by the conventional P/M technique (tensile strength of ordinary sintered low alloy steel by press molding is around 1000 MPa and elongation is 1-2%)¹⁰⁾. We conclude that this is a manifestation of superior properties of fine heterogeneous structure with locally gradient nature of contents unique to sintering material of mixed powder. This structure is the martensite phase (in case of high concentration, retained austenitic phase), which appears according to the Ni concentration gradient, particularly due to insufficient diffusion of aggregated Ni powder in the Fe matrix powder, and is surrounded in mesh by the tempered martensite

phase. As the above properties were only obtained by using the natural phenomenon of aggregation of Ni powder and composition of Fe-2% Ni-0.5%Mo, further superior properties (targeting more than 2000 MPa of tensile strength, more than 5% of elongation, and more than 600 MPa of rotational bend fatigue strength) could be sufficiently expected by artificially changing the size and content of the Ni powder or sintering/thermal processing conditions based on this steel type. Therefore, we examined the optimum structure on the micro-level such as the composition and percentage of each phase that composes the heterogeneous structure and their dispersion state.

2.2 Method of Experiment

We used carbonyl iron powder (Fe-OM, average grain size: 4.4 μm , made by Fukuda Metal Foil & Powder Co., Ltd.) as the powder for this experiment. We also used water atomization powder (AKT-Ni, made by Mitsubishi Steel Mfg. Co., Ltd.) as the Ni to be added, classified into 3 grain sizes. The average grain sizes were 6, 16 and 24 μm , which we called fine, medium and coarse, respectively, and added 4, 6 and 8 mass% in the mixture. As the binder, we blended 69 mass% of paraffin wax, 20 mass% of atactic polypropylene, 10 mass% of carnauba wax and 1 mass% of stearin acid. The powder and the binder were kneaded so that the powder ratio became 65 vol% and a tensile test plate the shape of a dumbbell was created by injection molding using the obtained raw material. Paraffin wax was first removed from the compact using the solvent degreasing method in the heptane gas phase, then heated degreasing and sintering were conducted successively. Sintering was conducted in a vacuum atmosphere of 10^{-1} Pa and a sintering temperature of 1200-1350 $^{\circ}\text{C}$ was maintained for 1 hour. The sintered compact was thermal processed in the Ar atmosphere.

After maintaining 900 $^{\circ}\text{C}$ for 30 minutes, quenching was performed in oil and then after maintaining 200 $^{\circ}\text{C}$ for 120 minutes, tempering was performed by air cooling. The test piece was then tested for relative density measured by the Archimedes method, carbon content, structure observation, and Ni distribution by EPMA and tensile test.

2.3 Test Results and Observations

The density of the obtained sintered compacts was 95% or more of the relative density in any Ni powder grain sizes and Ni contents. The carbon content of any thermal processed materials was about 0.4 mass%.

Fig. 2 shows the pictures of the structure of the typical thermal processed materials.

The specimens show that white Ni-rich phases exist

in any structure, highlighted by the arrows and are surrounded by tempered martensite phases, seen as a network structure. It is observed that the bigger the Ni powder grain size and the more the Ni content, the larger the Ni-rich phases.

Fig. 3 shows the distribution of Ni by EPMA. As it shows the areas of high and low Ni concentration, it is clear that this is the heterogeneous structure with Ni content gradient. It was found that when Ni powder of small grain size is used, Ni is dispersed within an Fe matrix resulting in a smaller difference in concentration. It was also revealed that when Ni content is large, the difference in concentration also becomes larger.

Fig. 4 shows the tensile strength obtained from the tensile test. All the test pieces show a very high value of around 2000 MPa.

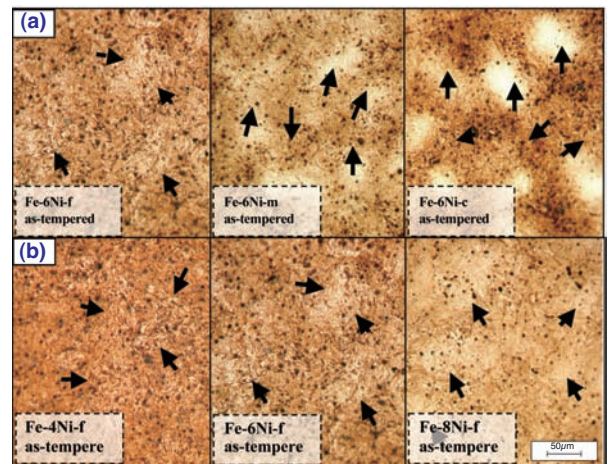


Fig. 2 Representative of optical microstructures for various Fe-Ni steel compacts sintered at 1250 $^{\circ}\text{C}$ for 1 hour in vacuum atmosphere. The arrow shows the bright martensite region. (a) As-tempered compacts of different Ni particle size, (b) As-tempered compacts of different Ni content (mass%)

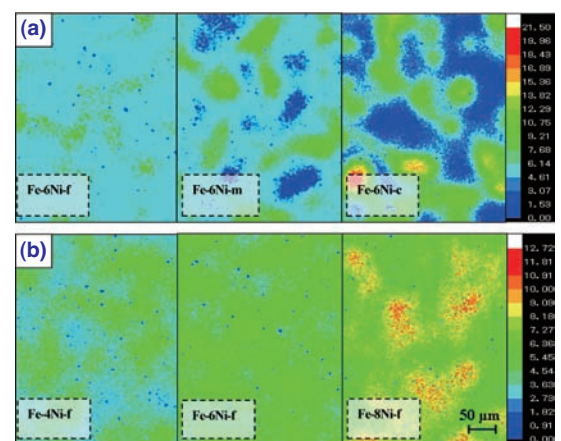


Fig. 3 Representative of Ni element mappings by EPMA analysis for as-tempered Fe-Ni steel compacts changing (a) Ni mean particle size, (b) Ni content (mass%)

Higher strength and elongation are seen in samples with smaller Ni powder grain size and the test pieces with Ni content of 6% show the maximum values. Fig. 5 shows the elongation, showing that the smaller the Ni powder grain size, the greater the elongation and the Ni content of 6% again shows the largest value. The test piece with fine Ni and 6% content showed a very strong property of 2040 MPa of tensile strength and 8.1% elongation. This is the highest level among the reported sintered low alloy steels ¹¹⁻¹⁴⁾ by MIM. It is concluded that such ultra high strength properties were obtained because of the fine heterogeneous structure.

Fig. 6 shows the hardness of the test pieces of fine powder with Ni content of 6% before and after the tensile test. The Ni-rich phase showed a lower value than the tempered martensite phase before the tensile test.

However, hardness of the Ni-rich phase increased nearly 20% from before the test showing an even higher value than the tempered martensite phase. On the other hand, little change was observed in the hardness of the martensite phase.

We also attempted to quantify the retained austenite before and after the tensile test by X-ray diffractometry (XRD). Fig. 7 shows the retained austenite amount before and after the tensile test. The retained austenite existed nearly 17% before the test and decreased to 6% after the test. From the above, it is concluded that the stress-induced martensitic transformation (TRIP) occurred in the Ni-rich phase resulting in improved hardness. It was found that this also caused ultra-strong tensile properties in the thermal processed materials of sintered low alloy steel with heterogeneous structure ¹⁵⁾.

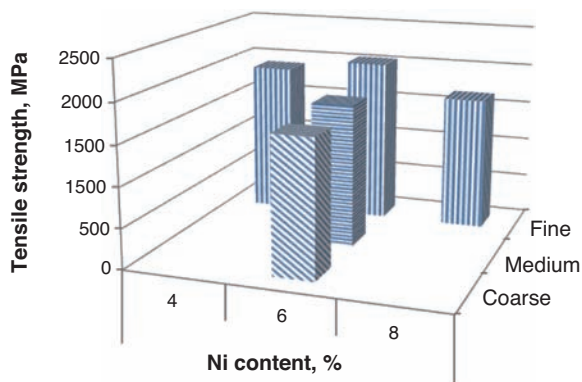


Fig.4 Tensile strength of different Ni content and particle size

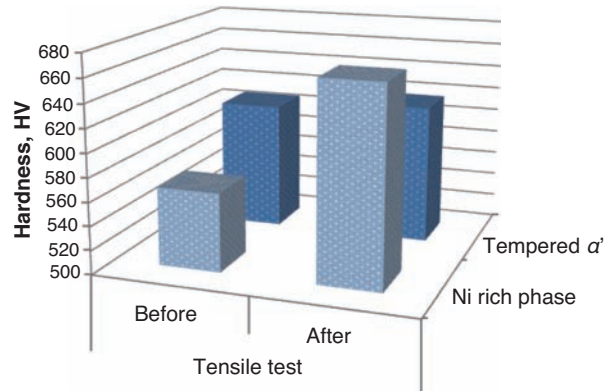


Fig.6 Micro vickers hardness of each region at before and after tensile testing

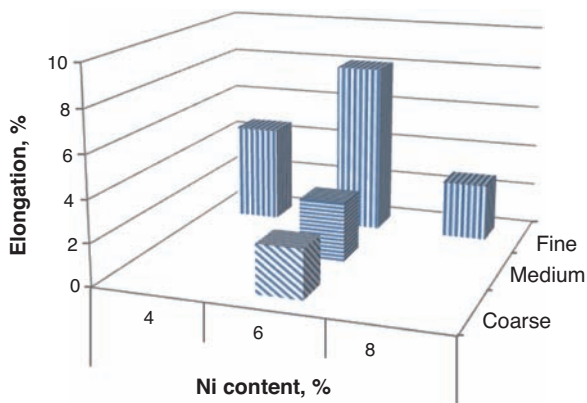


Fig.5 Elongation of different Ni content and particle size

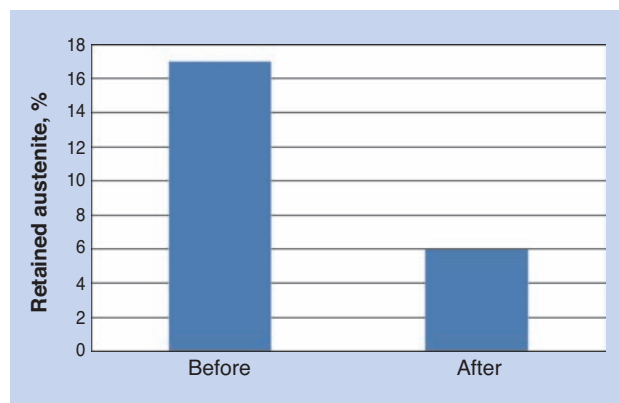


Fig.7 Retained austenite at before and after tensile testing

3. Powder Lamination 3D Printing

CAD has become a common practice for development and design of components and products. Particularly, as component shapes are stored as 3D CAD data, a new additive manufacturing (AM) has been developed to shape the actual body from the data. The most representative method is stereolithography which forms thin layers of light curing liquid resin by laser light scanning, to shape the products by adding layers as needed. This is applied to the metallic and ceramic powder in a technique called powder bed fusion (PBF; the former is called “laser forming” hereinafter). The following methods are available as AM:

- **Material extrusion (ME) method:** The most popular method of additive manufacturing uses continuous extrusion of melted thermal plastic resin from a nozzle.
- **Sheet lamination (SL) method:** An additive manufacturing method that uses adhering sheet-like material such as paper and film.
- **Directed energy deposition (DED):** An additive manufacturing method that injects droplets of metallic powder liquefied by plasma or laser from a nozzle.

Recently, material development and manufacturing techniques have evolved so that AM is not only used simply for creating a mold to check the shape design but also for manufacturing products of rich functionality with a certain degree of precision. We are mainly focusing on laser forming here.

Several techniques for supplying powder for laser forming have been researched for laser forming using powder¹⁶⁾. Initial techniques consisted of the use of binder content mixed with or coated on the powder where only the binder was melted and used for binding. Some require further sintering and others do not. The former required degreasing and both frequently used impregnation. With a larger amount of resin binder, the forming speed is faster. Therefore, with green body forming, the time is significantly reduced. However, in instances where the resin binder is not used, the forming time tends to be longer. In the former case, the processes are shortened from 2 processes of degreasing/sintering and infiltration to one process of degreasing/sintering/infiltration by changing blending of resin (thermosetting phenol and paraffin wax) and the coating method, as well as the property of the base material. There are also improvements of strength and dimensional accuracy by HIP processing instead of infiltration, or by applying impregnation and infiltration after liquid phase sintering of nickel phosphor bronze and completely melting it

controlling laser output. In the case of Fe-Ni mixed powder, development of improving dimensional accuracy is also conducted by sealing the remaining pores with shot peening however, those methods require many processes and the strength is not sufficient.

Therefore, a method to directly irradiate by the laser only metallic powder for melting and binding to build products is under research and development. Its principle is shown in Fig. 8¹⁷⁾. First, a layer of powder is placed on the manufacturing table (cylinder) and the laser irradiates the powder based on the CAD data so that the powder melts and solidifies. Next, the following layer is placed on the manufacturing table from the powder supplying cylinder with a roller then the laser irradiates the sample, fusing and solidifying the powder. By repeating this lamination process, the desired 3D shape can be obtained. In this case, the dimensional accuracy and surface roughness are not at the industrially satisfactory level. Due to this, metal stereolithography composite machining technology was developed where accurate cutting technology is added as an additional machining process to produce molding with short delivery time and low cost.

The following describes the recent outcome of research of the author group¹⁷⁻²²⁾, as they have been focusing on biomaterial and Ti as aircraft component material and conducting basic research of laser forming using Ti powder in the degas/Ar gas atmosphere as the net shape machining technology of complex structure.

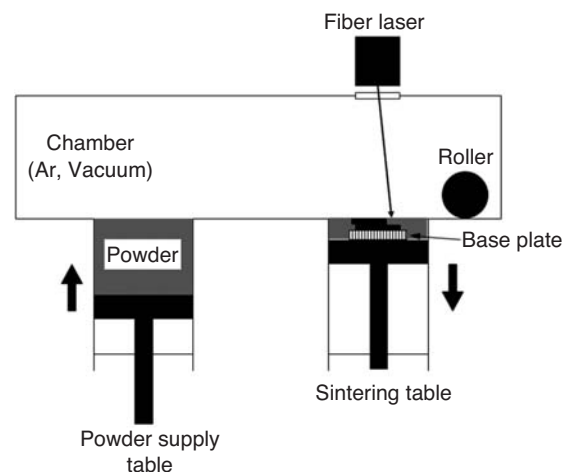


Fig.8 Sketch of laser forming equipment

3.1 Ti Powder Laser Forming

An important aspect of laser 3D forming is the high density and high accuracy of the product. In our research, we have improved the relative density of the compact up to 97.8% through the improvement of the powder supply process. In this research, we have created high density compacts by improving laser conditions, evaluating their mechanical properties and examining the impact of the powder grain size on the side surface accuracy. This is done with the intent of creating compacts of even higher density and higher accuracy.

3.2 Experiment Method

We used Ti-6Al-4V alloy powder (TILOP64 made by Osaka Titanium technologies Co., Ltd.) by gas-atomized technique as the raw material powder. The grain size is under 45 μm and the average grain size is 33.4 μm. In addition, we prepared finer powder with the grain size under 25 μm (average grain size of 18.8 μm) to evaluate the impact of the powder grain size on the side surface accuracy. We used ytterbium fiber laser of the continuous oscillation method with maximum output of 330 W for the laser oscillator. The laser beam from this oscillator scans the powder with a final beam diameter of 50 μm using the scanning system including galvanometer mirror. The manufacturing chamber is filled with high-purity argon (600 Pa) after being degassed.

3.3 Test Results and Observations

First, a single layer was created changing laser parameters and the surface roughness was measured with a laser microscope (OLS-4000 from Olympus) in order to evaluate the impact of laser parameters on the surface roughness. Fig. 9 shows the measurement of the surface roughness of the single layer compact over energy density E_p [J/mm²] indicated by equation (1).

$$E_p = P / (s \cdot v) \dots\dots\dots(1)$$

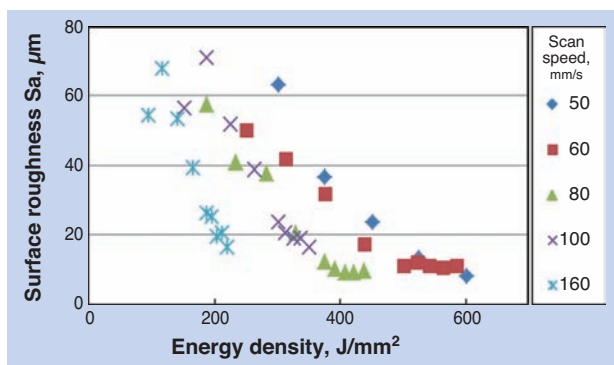


Fig.9 Surface roughness of single layers in function of volumetric laser energy density

The energy density is the energy input on the unit area, P [W] is the laser output, s [mm] is the scanning interval and v [mm/s] is the scanning speed. The surface roughness decreases as the energy density increases and converges at around $Sa=10 \mu\text{m}$. It is reported that the surface tension of the melted metal decreases as the temperature increases²³⁾, therefore, it is considered that the wettability of the melted part increases on the board as the temperature increases along with the increase of energy density to form a smooth layer on the surface.

Next, we conducted a lamination experiment. We decided that the shape of the laser formed compacts would be the same as the test pieces for the tensile test (14B test piece). For the forming parameters, we used 260 W and 80 mm/s, which were the conditions to make the lowest surface roughness in the single layer manufacturing experiment in the previous section.

The annealing process was applied to some laser formed compacts. Annealing consisted of maintaining the pieces at 700°C for 2 hours then cooling them in a furnace. Fig. 10 shows the cross-section image of a laser formed compact. This is a high density compact with a relative density of 99.8% with almost no voids. Fig. 11 shows the corrosion structure. Generation of acicular martensite by laser forming can be observed. In addition, epitaxial growth where the said structure grew vertically on the direction of formation was also observed. This structure did not change between before and after the annealing process.

Fig. 12 shows the tensile test results of the high density compacts. The JIS Standard for 60 types of titanium alloy specifies that the tensile strength and elongation to e 895 MPa and 10% respectively. The



Fig.10 Cross sectional microstructure of laser formed Ti compact

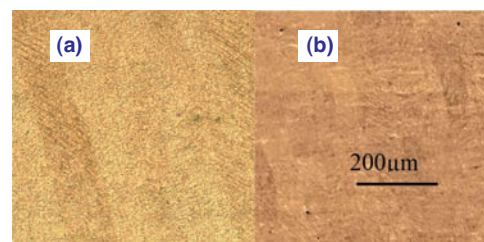


Fig.11 Etched microstructures of laser formed Ti compacts (a) As – formed (b) After heat treatment

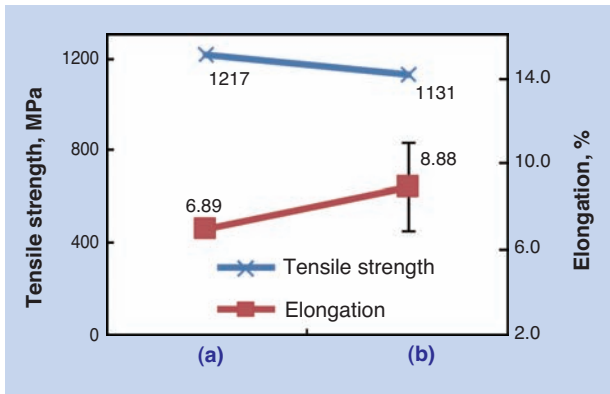


Fig.12 Tensile properties of laser formed Ti compacts
(a) As – formed (b) After heat treatment

tensile strength of the laser formed compacts is a sufficiently higher value than the standard.

The elongation indicates a lower value, but it is improved by the annealing process by over 10% in some samples. The fusion and solidification of the surface of the compacts is repeated by the laser scanning during laser forming, which generates residual stress within the formed compacts. This residual stress is considered to be one of the causes of the reduced elongation. We assume that by applying the annealing process, the residual stress was removed and the elongation was improved with a closer value to the JIS Standard.

Next, we also evaluated the dynamic mechanical properties. We introduced fatigue using the pulsating tension test with a frequency of 30 Hz and stress ratio of $R=0.1$ using an electro-hydraulic servo testing machine. Fig. 13 shows the fatigue test results. The vertical axis indicates fatigue strength under pulsating tension (twice the stress amplitude). The fatigue strength estimated from the tensile test result is more than 600 MPa and the fatigue strength of this test was 260 MPa, a significantly lower value than the estimated

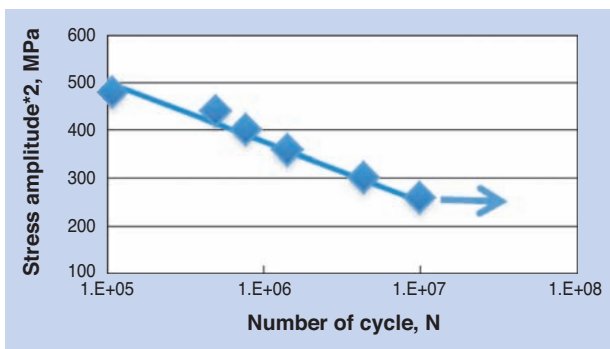


Fig.13 S-N curve of laser formed Ti compacts after heat treatment

value. One of the causes was assumed to be the impact of small voids still present within the material even with high density however; the details are to be examined in the foregoing review.

When laser scan is applied linearly on the evenly placed metallic powder layer, the metallic powder forms one linear compact as the metallic powder melts and solidifies as shown in Fig. 14. At that time, granular residues are generated around the formed compact. Fig. 15 shows the graph indicating the diameter of the residues. It was found that the diameter of residues became smaller by increasing the laser output and was halved when fine powder was used. Fig. 16 shows the side surface roughness of the laser formed compacts. Improvement of around 60% in surface roughness was confirmed in the compact using fine powder. A change in side surface properties was verified by using fine powder even with the same forming parameters however, the stable supply of uniform powder layer is difficult with fine powder. Therefore, further study is required for the improvement of side surface accuracy.



Fig.14 Appearance of a laser formed line

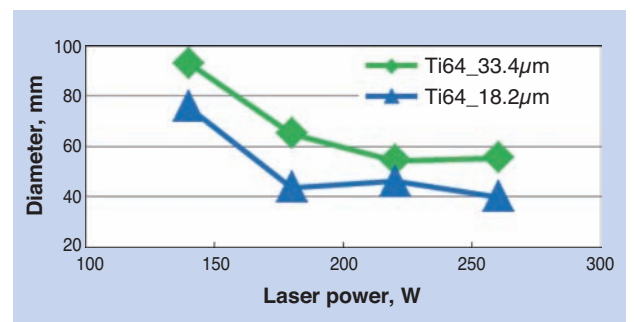


Fig.15 Diameter of adhered particles

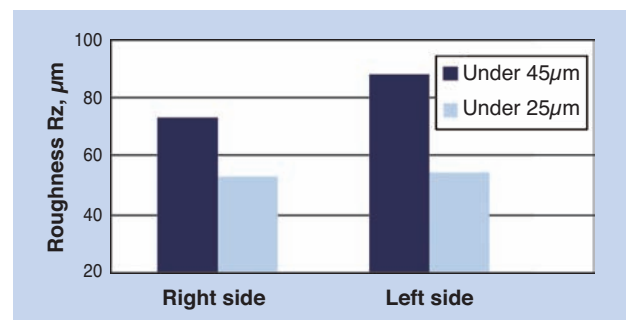


Fig.16 Side surface roughness of laser formed Ti compacts using different Ti particle powders

4. Conclusion

Metal injection molding (MIM) and powder lamination 3D printing by laser are introduced as new powder forming methods from our research and the former MIM is already recognized as an industrially useful forming method. However, creating large products is still difficult because of deformation due to their own weight during the debinding process and long processing time. If these problems are resolved, the scope of application is expected to be greatly expanded.

On the other hand, metallic powder lamination 3D printing has just begun with the ability of forming complex structure on the outside, as well as the inside. However, as the powder is melted and laminated, particularly roughness of the side surface and the entire dimensional accuracy need to be improved. There are also issues associated with volume production but, this is unique from the manufacturing viewpoint and attracting a lot of attention. Based on this, further development is very much expected.

References

- 1) R. M. German, Powder metallurgy science, translated by Hideshi Miura et al. Uchida Rokakuho (1996).
- 2) Kazuo Okamura et al. Plastic molding technology, 27 (1996) 235.
- 3) D Weinand et al. Plastic molding technology, 13 (1996) 19.
- 4) C. Quichand : Proc. of Powder Met, World Congress, EPMA, 2 (1996) 1101.
- 5) Hideshi Miura et al. Powder and powder metallurgy, 40 (1993) 393.
- 6) Hideshi Miura et al. Powder and powder metallurgy, 42 (1995) 353.
- 7) Hideshi Miura et al. Powder and powder metallurgy, 41 (1994) 1071.
- 8) Takeharu Baba et al. Powder and powder metallurgy, 42 (1995) 1119.
- 9) Hideshi Miura et al. Powder and powder metallurgy, 40 (1993) 988.
- 10) Hideshi Miura et al. Powder and powder metallurgy, 42 (1995) 378.
- 11) H. Miura, M. Matsuda, Material Transactions, 43 (2002) 343.
- 12) Materials Standards for PM Structural Parts, 2009 Edition, MPIF, Princeton, NJ, (2009) 48-49.
- 13) Materials Standards for Metal Injection Molded Parts, 2007 Edition, MPIF, Princeton, NJ, (2007) 16-17.
- 14) Metals Handbook, 10th ed., 1, ASM Int., Materials Park, OH, (1990) 430-448 and 793-800.
- 15) W. Harun, H. Miura et al. J. Japan Soc. Pow. & Pow. Met., 59 (2012) 677.
- 16) Masato Imamura, Powder and powder metallurgy, 48 (2001) 415.
- 17) Hideshi Miura et al. Powder and powder metallurgy, 53 (2006) 740.
- 18) Hideshi Miura et al. Powder and powder metallurgy, 54 (2007) 707.
- 19) Hideshi Miura et al. Powder and powder metallurgy, 55 (2008) 738.
- 20) H. Miura, et al. Proceedings of the MPIF/APMI International Conference on Powder Metallurgy & Particulate Materials (CD-ROM), (2009) 708.
- 21) H. Miura, et al. Materials Science Forum, 654-656, (2010) 2057.
- 22) H. Miura, et al. Proceedings of the 2012 Powder Metallurgy World Congress & Exhibition(CD-ROM), (2012).
- 23) Akio Sasama, et al. : Journal of The Japan Institute of Metals, 40 (1976) 1030.

<Author biography>

Hideshi Miura

Professor, Doctor of Engineering, Department of Mechanical Engineering, Kyushu University

- 1997 Steel Metallurgy Course (Master) completed, Department of Mechanical Engineering, Kyushu University, Assistant
- 1985 Doctor of Engineering received from Kyushu University, Assistant Professor, Department of Materials Development Engineering, Kumamoto University
- 1992-1993 Visiting Researcher, Rensselaer Polytechnic Institute, USA
- 1995 Professor, Faculty of Engineering, Kumamoto University
- 2004 Professor, Mechanical Engineering, Graduate School of Engineering, Kyushu University
- 2011- present President, Education and Research Center of Manufacturing, Kyushu University

[Specialty]

Material processing, powder metallurgy, metallic injection molding, laser powder lamination 3D printing

[Academic society and committee affiliations]

- Japan Society of Powder and Powder Metallurgy: Board Director (1996-2010), Vice President (2003-2010), President (2012-2014), Adviser (2014-)
- The Japan Institute of Metals and Materials: Subcommittee V, Manager (1995, 1996), Vice Chairman (1997, 1998), Chairman (1999, 2000)
- The Iron and Steel Institute of Japan: Division Steering Committee Member (Powder/Particle Forum Chair) (1998-2012), Division Vice Chair (2012-2014), Division Chair/Board Director (2014-2016)
- American Powder Metallurgy Institute: Powder Injection Molding International Symposium Organization Committee Member (1995, 1996, 1998-) P/M Sci. & Tech. Briefs Editorial/Review Member (1999-2005), International Conference Program Committee Member (2004-)
- The Japan Society of Mechanical Engineering: Materials and Processing Division, 81st Period Steering Committee Member (2nd Technical Committee Chair) (2003-2004), Division Vice Chairman (2005-2006), Division Chair (2006-2007), Fellow (2010-)
- The Japan Society for Technology of Plasticity: Board Director/Publishing Business Committee Chair (2007-2009), Kyushu District Head (2010-2012) Conference Steering Committee Chair, Publication Editorial/Review Committee Member, Award Selection Committee Member, Representative, Council Member, Program Committee Member of Powder Metallurgy International Conferences, Organizing Committee Member, Chair of the above academic societies

NTN Celebrates 50 years with Shinkansen. Our challenges for "Monozukuri" will continue.

It has been 50 years since the inauguration of the Shinkansen Tokaido line in 1964. NTN's bearings have been adopted by every generation of Shinkansen from the 0-Series to N700A, supporting its evolution. For example, the bearings for the wheel axles of the most recent N700A are about 70% lighter and 60% smaller compared with the original 0-Series, contributing to lightweight and high-speed railcars. For a faster, safer, more comfortable Shinkansen, our challenges for "Monozukuri" will continue.



Axle bearings

First generation
Axle bearings for
0-Series Shinkansen

^①

Newest model
Axle bearings for
N700A Shinkansen

^①

Recognized as the "1st Tribology Heritage" ^②

▲

Approx. 70% lighter

■

Approx. 60% smaller

^① Picture of a cutaway model where bearings are contained in the housing (bearing case).
^② Japanese Society of Tribologists recognizes technologies and materials which have contributed to the development of science and technology throughout the history of Japan.

**Congratulations
on the 50-year anniversary
of the inauguration of the
Tokaido Shinkansen!**



Product Introduction and Complex Technology of Resin, Sintered Metal and Magnet for Growth Markets

Yoshio OKI*



NTN Composite Material Products Division has developed the mechanical parts and bearings, and the unit module products by a wide range of materials and technology such as resin material, sintered metal, magnetic material and fluid dynamic pressure technology.

In order to meet the market to be diversified, NTN is working to develop the future markets while creating new material properties by promoting fusion of each technology and Composite Materials which are applying tribology, bearing material, high-precision processing technology and magnetic materials.

This paper reports the Developed Products of Composite Products for the further growth markets.

1. Introduction

NTN's Composite Material Products Division consolidates and integrates fluid dynamic pressure technology and technologies of NTN's related companies, which include NTN Engineering Plastics Corp., NTN Powder Metal Corporation and Nippon Kagaku Yakin Co., Ltd., to develop unit module products to be used in the automotive and industrial industries. Currently, NTN is working specifically on the following activities, focusing on the growing markets such as electric vehicles and energy:

- 1) Development and proposal of not only components but unique unit products by combining resin and sintered metal
- 2) Development of light and compact sliding bearings as an alternative to rolling element bearings
- 3) Sintering of machine parts which require high strength
- 4) Product development for industrial and automotive industries applying magnetic material technologies
- 5) Proposal of "only one" technology including amorphous magnetic material into growing markets

2. Product line and production system of Composite Material Products Division

NTN's composite material products include mainly resin, sintered metal, and magnetic materials. These products are produced by the NTN's four related companies shown in Fig. 1. Key products developed by the NTN companies are introduced in Section 3 and the subsequent sections. Various technologies/products are also covered by different articles.

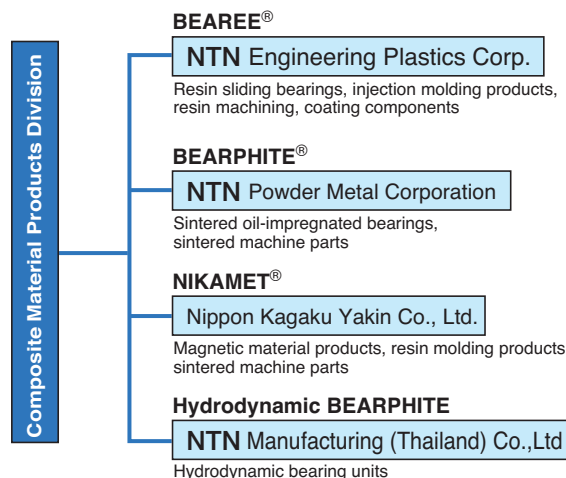


Fig. 1 Products and production system of composite material products

* Composite Material Products Division

3. Resin material products

Resin components have a high degree of freedom for design and are used in diverse fields as alternatives to metal components since they are inexpensive and can be made lightweight, compact, and corrosion resistant. NTN develops and designs resin materials, specifically working toward higher product functionality by leveraging the resin properties and improving bearing load properties by creating composite material with metal. The following is the recent resin material:

(1) Resin sliding bearings¹⁾ for electric water pump

Use of electric and hybrid vehicles is increasing because of to the reduction in CO₂ emissions. Conventional vehicles driven by internal combustion engines are equipped with centrifugal pumps for circulation of radiator water for engine cooling. These are driven by the engine rotation which is transmitted to the pump shafts through the engine belts. Contrary to this, electric vehicles do not have engines and hybrid vehicles stop engines with a start/stop function. Therefore, electric pumps are required for inverters or engine cooling systems. These electric water pumps are mainly high-efficient and compact centrifugal pumps with magnetic drives.

Fig. 2 shows the structure of the magnetic-drive centrifugal pump. This structure allows fluid, such as antifreeze liquid, to flow by rotating impellers integrated with magnetic casing using the magnetic force of the magnet installed on the motor shaft as it rotates. As shown in Fig.3, BEAREE AS5704 made of polyphenylene sulfide (PPS) resin with special filler blended in is used as the bearings in the center of the impeller. These bearings have sliding contacts between the internal bore of the bearing and the stationary shaft and the bearing side face and the thrust pad. These sliding contacts support the radial and axial loads respectively.

[Features]

- (1) Friction in the water is 1/5 or less compared with sliding bearings made of universal PPS resin
- (2) Reduced friction damage to mating material, such as stainless steel
- (3) Larger degree of freedom for design due to injection molding
- (4) Compatible with antifreeze, acid, and alkaline fluid

Table 1 shows a comparison of performance among typical sliding bearings used in fluid. Bearings made of carbon excel in wear resistance in fluid; however, they show a lower degree of freedom in shape because they are machined from formed materials and possess

inferior crack resistance against impact. The cost is also a challenge. Since BEAREE AS5704 bearings are mainly made of PPS resin, they have superior properties in self-lubricity, chemical resistance, and a high degree of freedom in design using injection molding. It is easy to provide lubrication grooves on the internal surface of the bearing bores, end faces, and retainers (D-cut, projection, etc.) on the outer surface of the bearings which can be molded into a single piece without the machining process.

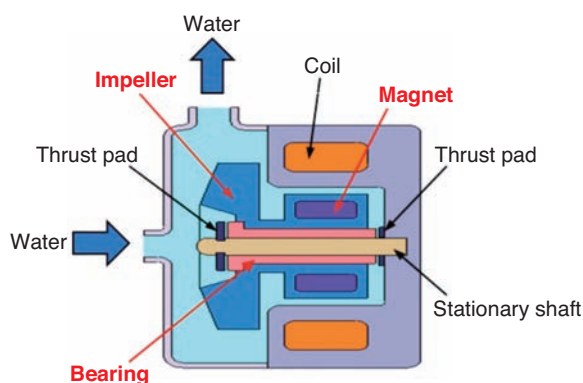


Fig. 2 Structure of magnet drive centrifugal pump



Fig. 3 Plastic sliding bearings for electric water pump (BEAREE AS5704)

Table 1 Comparison of features various bearings

Types of bearings	BEAREE AS5704	Carbon	Phenol resin (graphite blended)	PTFE (graphite blended)
Machining method	Injection molding	Machining	Injection/compression molding	Machining
Wear resistance (under water)	◎	○	△	×
Chemical resistance	◎	◎	△	◎
Water absorption dimensional stability	○	×	△	○
Crack by impact	○	×	×	○
Deformation by impact	○	○	○	×
Degree of freedom for design	◎	×	○	×
Price	◎	×	○	×

◎ Excellent ○ Good △ Fair × Poor

Fig. 4 shows the specific wear rate of BEAREE AS5704 and various PPS resin materials with glass fiber, carbon fiber, and PTFE resin blended in.

AS5704 is superior in wear resistance when compared to other PPS materials because it has special filler materials added to the PPS resin.

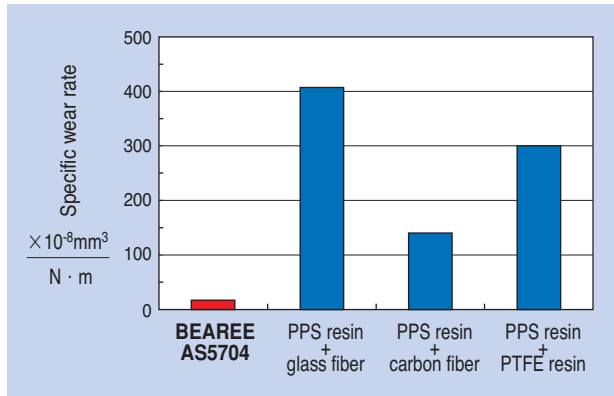


Fig. 4 Wear factor of PPS bearings

(2) Resin sliding screws for high load ²⁾

Feed screws, which convert rotational motion of the motor to linear motion, are used for carrying units of medical and food equipment. Feed screws include ball screws and resin sliding screws.

Table 2 shows the comparison of their performance. Ball screws are superior in load capacity and screw efficiency, although they are an expensive option. In addition, as they are lubricated with grease, they are not suitable for use where dispersion of grease and deterioration due to high temperatures are a concern. On the other hand, resin sliding screws have lower load capacity but they do not require lubrication allowing for use in a broader range of applications, including vacuum or high-temperature ambient. They are also less expensive and quieter during operation.

NTN's sliding screws made of precision resin consist of PPS resin nuts and stainless steel screw shafts as shown in **Fig. 5**. Due to the PPS resin having improved wear/friction property by blending solid lubricant, it also

results in a longer life when compared to general-purpose resin sliding screws.

NTN has recently developed resin sliding screws for high load, which have been limited to lower load applications, and proposing them for a cleaner production environment and increased load capacity. NTN has created a composite nut applying PPS resin sliding material onto the surface of threads of a brass nut as indicated in **Fig. 6**, by injection molding, and increased the heat transfer and load capacity. The brass has a special surface treatment to improve adhesion with the resin. This composite structure improved not only the bearing load capacity but also durability.

The resin sliding screws for high load have twice the axial load capacity and 9-times higher nut static breaking load when compared to the conventional resin sliding screws. In addition, the life under high load condition is 3 times longer than the conventional resin sliding screws.

[Features]

Comparison with conventional products (NTN resin sliding screw)

- (1) Permissible axial load: 2 times**
- (2) Nut static breaking load: 9 times**
- (3) Friction: 1/3**

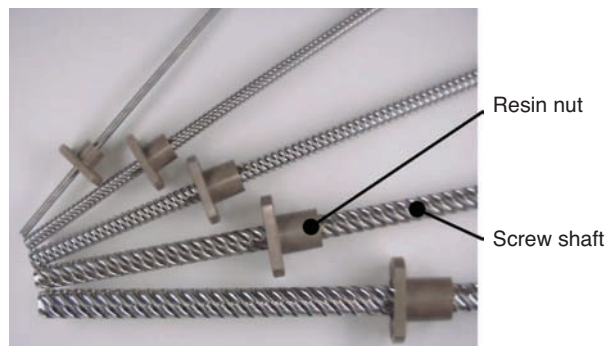


Fig. 5 Resin sliding screws

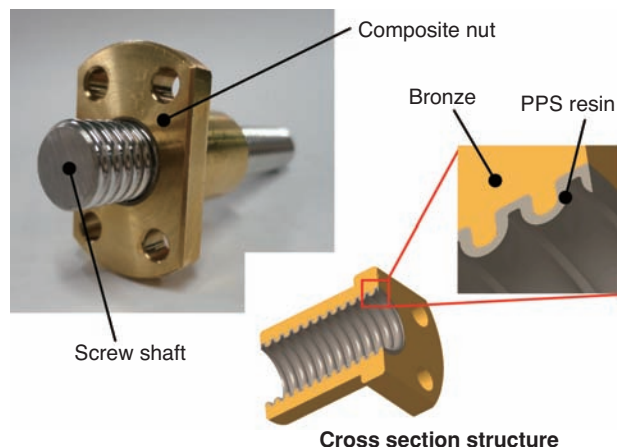


Fig. 6 Resin composite sliding screws for high load

Table 2 Comparison of features various sliding screws

Item	Ball screw	Resin sliding screw	Resin sliding screw for high load
Lubrication	Required (grease)	Not required (can also be used with lubrication)	Not required (can also be used with lubrication)
Load resistance	◎	△	○
Screw efficiency	◎	△ ~ ○	○
Noise	△	○ ~ ◎	◎
Heat resistance	△	△ ~ ○	○

◎ Excellent ○ Good △ Fair

(3) Hybrid PEEK bearings²⁾

The majority of power consumption of an air conditioner is occupied by the compressor. Therefore, higher efficiency is required to reduce energy consumption of an air conditioner. Fig. 7 shows the structure of a compressor and the installation positions of the bearings. The bearings are required to have improved friction/wear properties and resistance against heat (the refrigerant liquefied by over-compression can make the refrigerant oil leak from friction).

Therefore, NTN is developing hybrid PEEK bearings with improved friction/wear properties and resistance against being burnt using composite material of sintered alloy and PEEK resin.

Fig. 8 shows the structure of hybrid PEEK bearings. Different from polytetrafluoroethylene resin wrapped bushings made by the impregnation/sintering process on the sintered intermediate layer of a steel plate, these bearings are made with a layer of 0.5 mm thick PEEK resin applied on the internal surface of the sintered alloy bushing by injection molding. PEEK resin is suitable for injection molding and excels in heat, wear, chemical, and fatigue resistance. In addition, it also considerably improved heat transfer properties in the composite structure with metal compared to the bearings with only PEEK resin material.

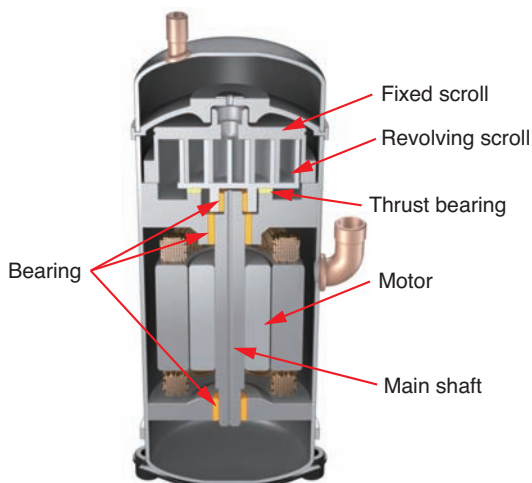


Fig. 7 Structure of air conditioner compressors

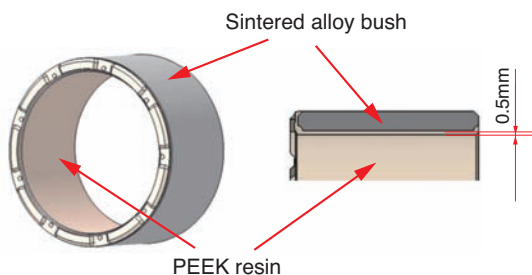


Fig. 8 Structure of hybrid PEEK sliding bearing

The hybrid PEEK bearings have the following features compared to conventional PTFE resin wrapped bushings:

[Features]

Compared to conventional products (PTFE resin wrapped bushing)

- (1) Friction coefficient: 2/3, wear: 1/3**
- (2) Heat resistance: more than 5 times**

4. Sintered metal products

NTN Powder Metal Corporation works on high functionality of conventional oil-impregnated sintered bearings and develops high-strength machine parts mainly for automotive applications. In the automotive applications, sintered products are increasingly used as a part of the component cost reduction, which accounts for approximately 60% of the sintering market or approximately 9.2 kg per vehicle. The following is the introduction of high-strength sintered materials and various types of sintered bearing products developed for this growing market:

(1) High-strength sintered materials⁴⁾

Sintered machine parts for automotive applications include engines, drive components, and in-vehicle oil pumps and starter motors. Fig. 9 shows an example of sintered gears. In addition, Fig. 10 shows the results from a comparison test of ring compressive fatigue strength of high-strength sintered materials. The fatigue strength of the developed products is about 2.3 times that of the conventional products. The sintered machine parts require not only high-strength but also support for high precision and the ability for complex shaping. Additionally, we are optimizing material composition, manufacturing method, and thermal processing to expand applications starting from replacement of cold forging materials.

[Features]

- (1) True density ratio: achievement of 96%**
- (2) Fatigue strength: 2.3 times compared to the conventional products**
- (3) Young's modulus: achievement of 180 GPa**

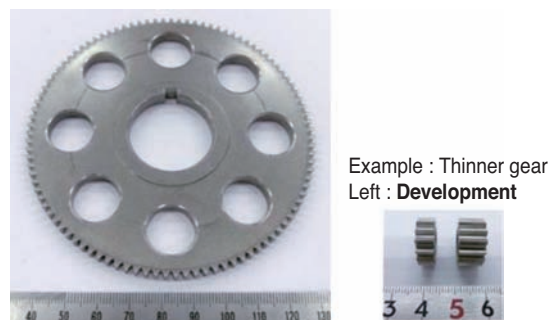


Fig. 9 High strength sintered gear

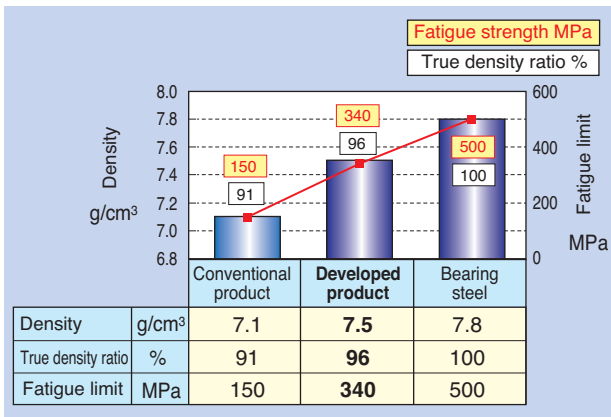


Fig. 10 Ring compressive fatigue strength

(2) Multi-layer sintered oil-impregnated bearings⁵⁾

With increased infrastructure development in the world including emerging markets, demand for construction machines, such as hydraulic shovels, is also increasing. For joints of these hydraulic shovels, use of sintered oil-impregnated bearings is increasing for longer oiling intervals. Higher strength is also required due to severe operating conditions. Conventionally, oil content is secured in low density to prolong oiling intervals while strength and hardness are improved by thermal processing, then dimensional accuracy is achieved by machining the bearings.

The multi-layer sintered oil-impregnated bearings shown in Fig. 11 have two types of powders with different properties molded simultaneously into one piece so that the inner layer has sliding and wear resistant properties while the outer layer has a high strength property. This process can eliminate the need for thermal processing such as carburized hardening and the machining process to achieve a significant reduction of the manufacturing workload.

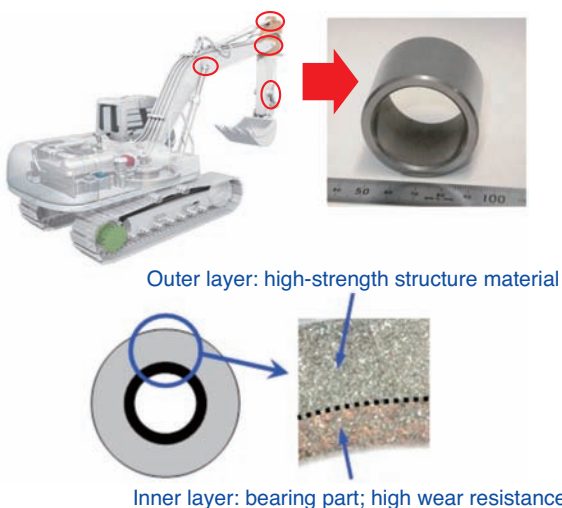


Fig. 11 Multi-layer BEARPHITE for joints of hydraulic excavators

[Features]

- (1) Simultaneous forming of two types of powder materials
- (2) Different properties between the inner layer and outer layer

Fig 12 shows comparison of the friction coefficients between this newly developed product and conventional product (bearings that use the inner layer material of the newly developed product only).

This developed product uses the high-wear resistant material in the inner layer only but has the equivalent friction property as the conventional product, which uses the same material for the entire product.

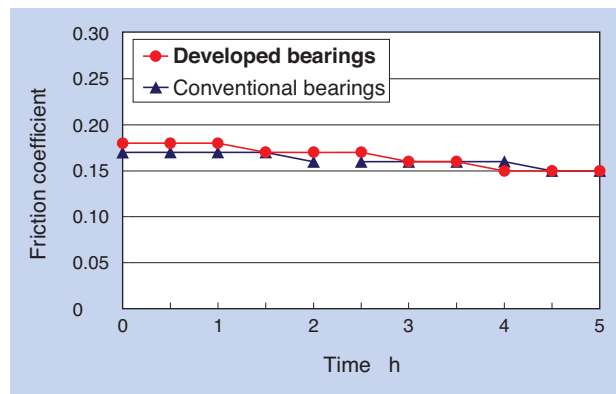


Fig. 12 Friction coefficient measurements

(3) Corrosion resistant sintered bearings⁴⁾

Bearings for valves in fuel pumps and exhaust gas recirculation (EGR) systems require high corrosion resistance as they are in contact with fuel, etc. The typical material for this is cupronickel-based materials. However, this material contains a rare metal, nickel, with the requirement for high corrosion resistant bearings without rare metal increasing. NTN has focused on aluminum bronze which exhibits good corrosion resistance resulting in corrosion resistant bearings with better corrosion resistance and sliding property than cupronickel-based sintered bearings.

Fig. 13 shows an example of bearings for a fuel pump.

[Features]

- (1) Corrosion resistance equivalent or superior to cupronickel-based material
- (2) Improved corrosion resistance without using rare metal
- (3) Significant improvement of wear resistance over cupronickel based material

Table 3 shows the test results of corrosion resistance against organic acid and sulfur. The test piece was

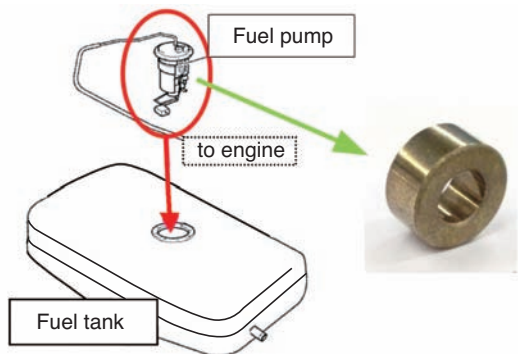


Fig. 13 Sintered bearing for fuel pump

Table 3 Result of anti-corrosion examination

	Weight change rate %	
	Developed material	Cupronickel based material
(1) Corrosion resistance test against organic acid	0.14	0.15
(2) Corrosion resistance test against sulfur	0.10	0.40

immersed in test fluid at the set temperature and time and the variation was calculated from the weight difference before and after test.

<Test condition>

(1) Corrosion resistance test against organic acid

- Test fluid: Organic acid concentration 2%
- Temperature: 50°C
- Test time: 100 hours

(2) Corrosion resistance test against sulfur

- Test fluid: Gasoline with 300 ppm of sulfur
- Temperature: 80°C
- Test time: 300 hours

The comparison between the newly developed material and cupronickel based material revealed favorable results, with an equivalent friction coefficient and the specific wear rate approximately 1/10 of the cupronickel based material.

5. Magnetic material products

Nippon Kagaku Yakin Co., Ltd. develops and promotes magnetic material products aiming at the converting mechanical components into functional components.⁶⁾

In this article, we are introducing products for growing the market, particularly by applying its unique technologies.

(1) Reactors for automobiles⁷⁾

The motor drive of the recent hybrid vehicles use dedicated batteries. These vehicles have achieved drive performance equivalent to fuel-driven engines in

acceleration/deceleration, which requires step-up (amplification) of the dedicated battery output voltage.

Therefore, step-up reactors are used for the system circuit components, which should support large current/high frequency as well as have a compact size for reducing electric cost. The current hybrid vehicles use Fe-Si (ferrite-silicon alloy powder) with the compression manufacturing method. In addition, for larger current to be applied with higher EV output, Fe (pure iron powder) products with high saturation magnetic flux density manufactured using the compression method are being considered. However, these materials have large iron loss with large heat generation and the step-up reactor tends to become larger in order to avoid this.

Fig. 14 shows the performance comparison of different core material for step-up reactors. The Fe-Si and Fe products made by the above mentioned compression method exhibit large iron loss. In comparison, the amorphous products by Nippon Kagaku Yakin Co., Ltd. have smaller iron loss and can be manufactured by injection and compression molding.

The newly developed “hybrid amorphous core”, in particular, is a combination of injection amorphous core and compression amorphous core. Fig. 15 shows the structure of hybrid amorphous core. Compression

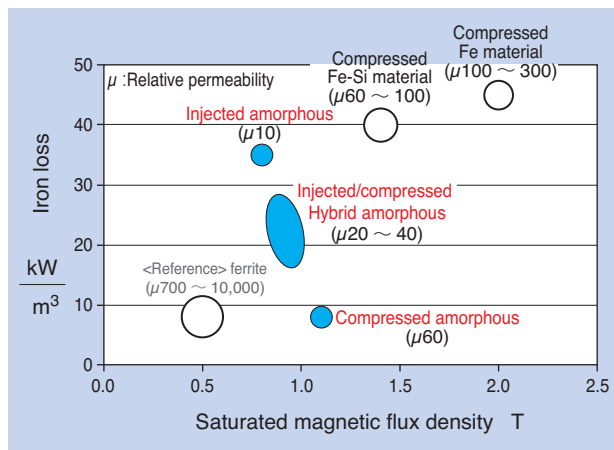


Fig. 14 Comparison of features various core material

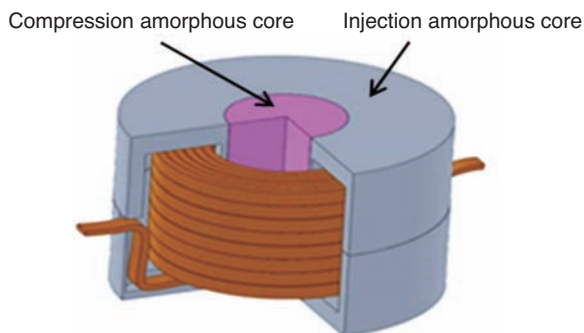


Fig. 15 Structure of hybrid core

amorphous with small iron loss is used for the area of electric-magnetic conversion for lower heat generation and injection amorphous with superior shaping flexibility is used for the magnetic conduit for retransmitting the converted magnet to the coil. **Fig. 16** shows an analytical example of heat generation of the hybrid core, which indicates appropriate placement of the respective cores. In addition, **Table 4** shows a comparison of hybrid core performance against injection and compression amorphous cores, respectively. The hybrid core exhibited favorable results in any property enabling manufacturing of pod-shaped core, which is difficult with compression amorphous core.

[Features]

- (1) Can be used in applications where large current or high frequency is required
- (2) Compact and low heat generation by composite structure
- (3) Higher degree of freedom for reactor shape design by injection molding

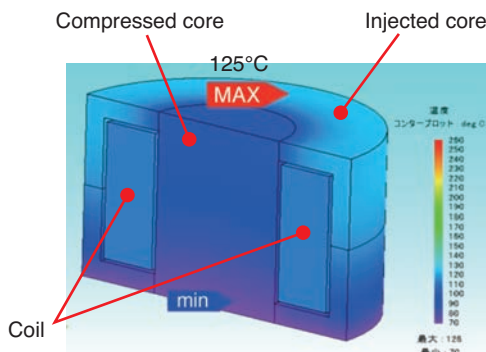


Fig. 16 Temperature distribution analysis of hybrid core

Table 4 Comparison of features various reactor core

	Single core coil (conventional product)		Hybrid core coil (newly developed product)
	Compression core	Injection core	Hybrid core
For large current	△ (large press required)	○ (DC bias: good)	○
For high frequency (low loss)	○	△ (Permeability: low)	○
Compact	○ (Permeability: high)	×	○
Heat suppressed	○ (Heat transfer: good)	×	○
Flexible shaping	△ (CNC press required)	○ (Injection molding: allowed)	○

(2) Dual track magnetic encoder

Industrial machine robotics require high positioning accuracy and use high-resolution absolute angle sensors which requires a highly accurate encoder.

NTN is introducing our newly developed dual track magnetic encoder. **Fig. 17** shows the structure of this newly developed product. Hard magnetic material is injected on the core metal of compressed ferrous soft magnetic material. This diagram shows an axial type dual track encoder with inner and outer ring patterns of a different number of accurately magnetized poles. The following are the features of the developed product:

[Features]

- (1) Supports opposite angle detection
- (2) Angle accuracy: $\pm 0.2^\circ$
- (3) Supports hollow structure

In addition, **Fig. 18** shows an absolute angle measurement method using this developed dual track magnetic encoder. Two sensors facing inside and outside magnetized rings, respectively, detect the signals. The absolute angle can be accurately measured by calculating the relative displacement of the patterns from the magnetic sensor signals, using a principle called caliper or Vernier principle.

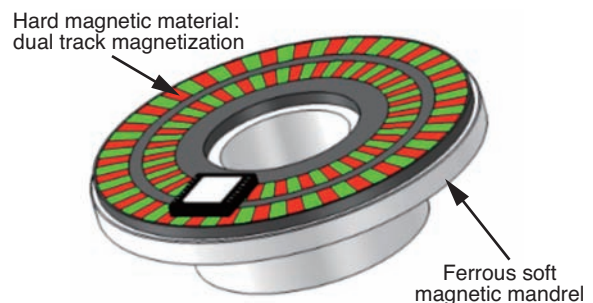


Fig. 17 Structure of dual-track magnetic encoder

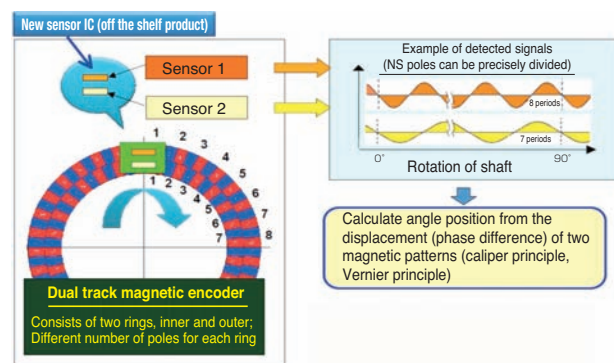


Fig. 18 Absolute angle measurement system

(3) Choke coil for MRI ⁶⁾

The MRI shown in Fig. 19 is a medical device used to provide images of sections of the human body using large magnetic energy. The choke coil integrated in this device is an electronic component to generate large current for creating a gradient magnetic field during testing.

Fig. 20 shows the components used for the developed choke coils. The coil, covered by an insulating case, is incorporated in the injection amorphous core to make the choke coil shown in Fig. 21.

Fig. 22 shows the inductance deviation rate (DC bias characteristic), which serves as a measure of the magnetic field generation capability when applied current is swept for amorphous soft magnetic material.

This is used in this developed product and the generally-used ferrite/iron-silicon (Fe-6.5Si) soft magnetic material.

In addition, Fig. 23 shows the frequency response of the inductance when weak current is applied. From these properties, the following features can be pointed out and this choke coil is suitable for this application which requires large current and stable high-frequency response characteristics:

[Features]

- (i) Inductance deviation rate is small even when high current is applied compared to the conventional ferrite and Fe-6.5Si.
- (ii) Change rate of inductance in the high frequency range is smaller than ferrite.



Fig. 19 Medical magnetic resonance imaging



a) Coil b) Case c) Injection amorphous

Fig. 20 Parts of choke coil



Fig. 21 Choke coil for MRI power supply

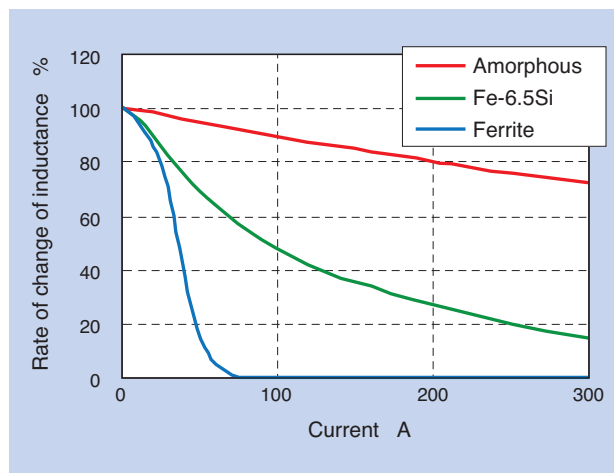


Fig. 22 DC bias characteristics

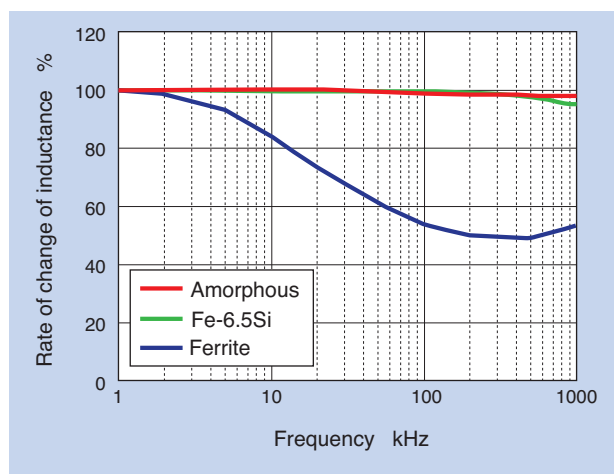


Fig. 23 Frequency characteristics

6. Conclusion

In this article, new products with composite materials for growing markets are mainly introduced.

With increased fuel efficiency and use of electric drive components in automobiles, being lightweight is a focal point in the development of components and composite material products.

In addition, NTN is also proposing new products to contribute to the development of our customers in the broad field of industrial machines, including medical devices, food equipment, robotics, etc.

NTN is poised to actively develop products by integrating a wide range of materials and technologies in response to the trend of the consistently growing markets and contributing to these markets.

References

- 1) Norio Itoh, Takuya Ishii: Plastic Bearings of Electric Pump for the Next Generation Cell, NTN TECHNICAL REVIEW, No. 77 (2009) 51-55.
- 2) Takuya Ishii, Yoshihide Himeno: Functional Improvement of Resin Sliding Bearing Through the Combination with Metal, Journal of the Japan Society of Polymer Processing, 25 (2), 73, 2013
- 3) Takuya Ishii, Ken Yasuda: Hybrid PEEK Sliding Bearing, NTN TECHNICAL REVIEW, No. 79 (2011) 125-129.
- 4) Tomonori Yamashita, Tomokazu Sonozaki: The Introduction of Sintered New Products for Automobile, NTN TECHNICAL REVIEW, No. 81 (2013) 74-77.
- 5) Yosuke Sugai, Toshihiko Mouri: Multi Layer BEARPHITE, NTN TECHNICAL REVIEW, No. 80 (2012) 83-86.
- 6) Takuji, Harano, Shinji Miyazaki, Hajime Katsuura: Introduction of Magnetic Material Products, NTN TECHNICAL REVIEW No. 80 (2012) 87-91
- 7) Takayuki Oda, Shinji Miyazaki, Eiichiro Shimazu: The Reactor Core for HEV Boost Converter, NTN TECHNICAL REVIEW No. 81 (2013) 46-51

Photo of author



Yoshio OKI
Composite Material
Products Division

The Improvement in Strength of Sintered Machine Parts

Takahiro OKUNO*

Naoki YASHIRO*



Sintered machine parts are used in many industrial fields. Especially, these are widely used for automotive parts. It is essential for the increasing use to improve mechanical properties of sintered parts. However, the pores in the sintered body are dominant factor for the strength of sintered parts. Therefore, various kinds of trial to decrease pores in the sintered body, or to increase sintered density were reported.

This article introduces the method of improvement of density and strength, and the mechanical properties of high-density sintered machine parts.

1. Introduction

Sintered machine parts have been adopted in diverse fields as they can be made into complex shapes and are suitable for inexpensive, large volume production.

The production volume of sintered machine parts in Japan amounted to approx. 90,000 tons in 2013 and more than 90% of that volume was for transportation machines.

Recently, in particular, sintered machine parts have been actively used in the automotive industry, with 9.0 kg used per vehicle; 50% of these are for the engine.¹⁾

In order to expand the scope of sintered machine part applications, improvement in their mechanical properties is vital. However, since sintered compact is porous, ordinary sintered machine parts are not as strong as molten steel parts. Therefore, reduction of pores in the sintered compact, namely, by methods to increase density, is being attempted to improve mechanical properties.

In this paper, we will present methods to make the sintered machine parts higher density/higher strength through materials or compacting and machining processes and improvement in mechanical properties.

2. Sintered alloy steel

Sintered alloy steel is used in many sintered machine parts²⁾.

Powders for sintered alloy steel have a particle size of approx. 300 μm or less and include alloy elements such as copper (Cu), nickel (Ni), chromium (Cr) and molybdenum (Mo), in addition to iron (Fe). Other elements include those specified in JIS Z 2550, which complies with the ISO Standards that specify their chemical contents. The specification for sintered alloy steel is different from molten steel. For example, Cu, which is treated as an impurity in molten steel, is actively used in sintered alloy steel for improving sintering properties at low temperature and enhancing sliding properties. Also, carbon (C) is added as graphite powder to be solidified into iron during sintering. This is to avoid significant deterioration of formability if graphite is solidified into iron in the powder form as the powder becomes hardened. Material manufacturers are developing proprietary powders outside the specification so that the optimum materials can be selected depending on the intended use.

The base metal powder is either mixed powder with all the additive elements, completely alloyed powder with additive elements pre-alloyed and homogenized, or diffusion alloyed powder which uses pre-alloyed additive elements with no negative effect of compaction and the remaining additive elements diffusion bonded by thermal diffusion.

* Advanced Technology R&D Center

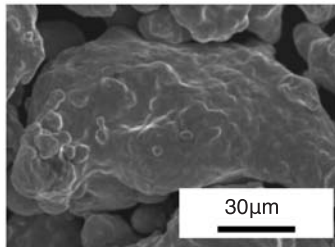
Table 1 shows the classification of metal powder of typical sintered alloy steel; Table 2 shows the features of completely alloyed powder and diffusion alloyed powder; Fig. 1 shows SEM micrographs. The following are typical sintered alloy steels used for machine parts.

Table 1 The classification of metal powder of typical sintered alloy steel

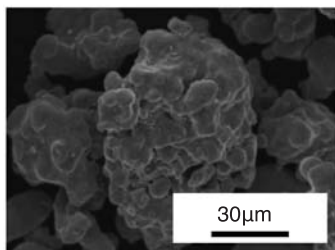
Powder type	Sintered alloy steel
Mixed powder	Fe-Cu-C base
Completely alloyed powder	Fe-Ni-Mo-C base Fe-Cr-Mo-C base
Diffusion alloyed powder	Fe-Ni-Mo-C base Fe-Cu-Ni-Mo-C base

Table 2 Feature of completely alloyed powder and diffusion-alloyed powder

	Completely alloyed powder	Diffusion alloyed powder
Homogeneity of powder	High	Low
Compaction property after forming process	Low	High



(a) Completely alloyed powder



(b) Diffusion alloyed powder

Fig. 1 SEM micrographs of completely alloyed powder and diffusion-alloyed powder

2.1 Fe-Cu-C base

Fe-Cu-C based material is widely used as sintered material for machine parts. Cu has a melting point of 1085°C and melts under the general sintering conditions of sintered alloy steel.

Therefore, Cu exists in the liquid phase between iron particles and is alloyed as sintering progresses. This results in high-strength. In addition, Cu is known for volume expansion when sintered with Fe powder³⁾. It can be used to control size change since the volume generally shrinks with sintering. Mixed powder is frequently used mixing pure iron powder with pure copper powder or graphite, etc.

2.2 Fe-Ni-Mo-C base

Fe-Ni-Mo-C based material is used to obtain high-strength sintered compact by various tempering and annealing processes after sintering. Wear resistance can also be obtained by applying a surface hardening process in addition to high-strength. Improvement of steel toughness can also be expected by Ni. Ni is frequently used with completely alloyed powder or diffusion alloyed powder.

2.3 Fe-Cu-Ni-Mo-C base

Fe-Cu-Ni-Mo-C based material is made by diffusion bonding of fine powders of Cu, Ni, Mo, etc. to pure iron powders. This is done to combine the features of the above two previous materials. It is currently widely used as high-strength sintering material since it has both high compaction and excellent mechanical properties.

2.4 Fe-Cr-Mo-C base

Cr, as an element for alloy, is generally used as machine structural parts in molten steel⁴⁾. On the other hand, when used as sintering material, it is difficult to reduce oxygen content as it has high affinity with oxygen. This means that high compaction and high density are difficult to obtain. However, with recent technological progress by material manufacturers, powders with low oxygen content are developed with improved compaction properties. Fe-Cr-Mo-C based material is used in completely alloyed powder due to the above mentioned affinity with oxygen.

3. Methods for densification/strengthening

Densification methods can be performed during molding, sintering and after sintering. **Table 3** shows those densification methods in each process.

Table 2 The method of densification at the production process

Process	Method
During molding	Warm forming Warm forming with mold lubrication, etc.
During sintering	2 forming 2 sintering Infiltration, etc.
After sintering	Sinter forging, etc.

3.1 Warm forming

Warm forming is a method to obtain high-density green compact by heating the powder and mold to 80-300°C during molding of metal powder. This reduces the yield strength of metal powder and increases compaction property⁵⁾.

Since this method is lower in cost compared with the 2-forming 2-sintering method and sinter forging method described later, it is used for sprockets of vehicle engines, etc.⁶⁾

3.2 Warm forming with mold lubrication

In general, metallic soap, such as Zn and Ca, or a resin based lubricant is added/mixed to reduce friction between the metal powder and mold when metal powder is molded; however, since the lubricant disappears during sintering, it inhibits densification. Warm forming with mold lubrication is a method to reduce lubricant by pre-applying the lubricant to the mold, in addition to the above warm forming method, to obtain high density green compact⁷⁾. Since it is possible to obtain higher density sintered compact than the warm forming method, it is used in reactors of hybrid vehicles, etc.⁸⁾

3.3 2-forming 2-sintering

Also called 2P2S (2Press-2Sinter). This is a method to obtain high density sintered compacts by first forming powder under a predetermined pressure and applying preliminary sintering with a relatively low temperature of 1000°C or below. Then the compact is formed under a predetermined pressure again and sintered with a higher temperature than the preliminary sintering. This is used in synchronizer hubs of vehicle transmission, etc. where strength is required⁹⁾.

3.4 Infiltration

Infiltration is a method to infiltrate melted material of a low-melting point into the pores of a sintered compact. Material is communicated from the surface using capillary phenomenon to fill in the pores¹⁰⁾. Specifically, the sintered compact and the green compact of low-melting point material are placed in contact with each other and heated to a temperature more than the melting point of the green compact and less than the melting point of the sintered compact for infiltration. Since it is possible to close the pores in the sintered compact, it is used in the applications where high air-tightness is required such as compressor components or hydraulic pressure resistant components.

3.5 Sinter forging

Sinter forging is a method to obtain product by forming and sintering metallic powder, and inserting the heated sintered compact into a mold for closed die forging¹⁰⁾. A regular forging method, such as hot forging of sintered compact, with a shape close to the formed product, is also adopted. Since it is possible to obtain a value close to the true density, it is used in connecting rods of vehicle engines, etc.

4. Development of high density sintered machine parts

NTN is working on development of high density sintered machine parts with potential for various applications. The following is an example of mechanical properties of the developed materials.

4.1 Method for making test piece

We made a 23.2 mm OD×16.4 mm ID×7 mm H ring-shaped test piece by warm forming of 80°C from the Fe-Ni-Mo-C based material. This was made of diffusion alloyed powder of Fe and diffusion bonded Ni and Mo with a predetermined amount of graphite mixed with lubricant, using floating die method. Next, the green compact was sintered in a mixed atmosphere of N₂ and H₂, then carburized tempering/annealing was applied. In addition, we prepared Fe-Cu-Ni-Mo-C based material as conventional high-density sintered compact as a control.

4.2 Mechanical properties

Fig. 2 shows sintered density and radial crushing strength. The sintering density of the developed material is 7.63 g/cm³ which is approx. 97% of true density of 7.8 g/cm³. The radial crushing strength is 2180 MPa which is an improvement of 30% or more from the 1630 MPa of the control. **Fig. 3** shows the cross section micrograph of the sintered compact. It

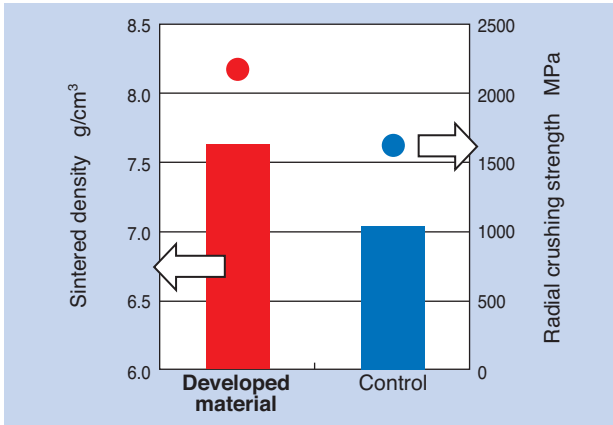


Fig. 2 Sintered density and radial crushing strength

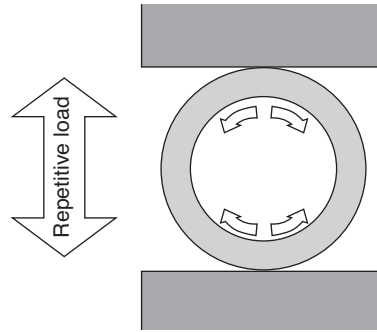
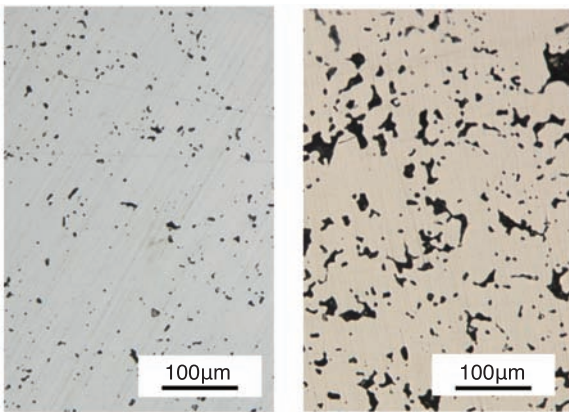


Fig. 4 Schematic the method of measuring ring compressive fatigue strength



(a) Developed material Density 7.63g/cm³ (b) Control Density 7.01g/cm³

Fig. 3 Optical micrographs of sintered part

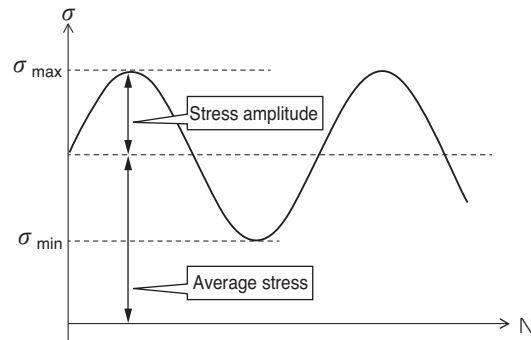


Fig. 5 The stress wave form at fatigue test

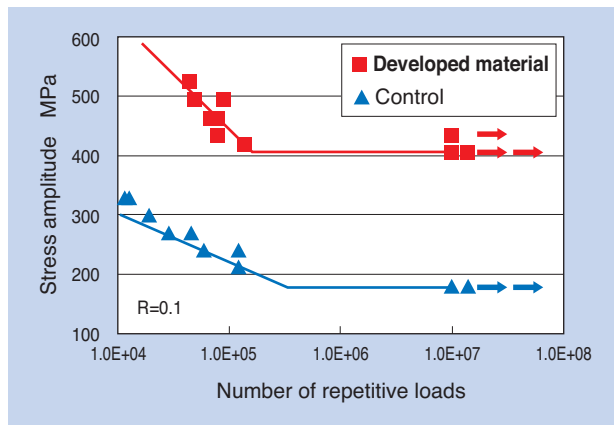


Fig. 6 Stress-endurance diagram

can be observed that the number and size of the internal pores are both reduced.

We evaluated the fatigue properties of the high-density sintered compact with the ring compression fatigue test. The ring compression fatigue test evaluates fatigue strength by repetitively applying compressive load on the ring outer surface which produces tensile stress on the inner surface of the ring in the direction of the load. Fig. 4 shows an overview of the measuring method. The test condition was set with a stress ratio $R=0.1$ and load frequency 50 Hz. The fatigue strength was defined as the stress amplitude when the repetitive load of 10^7 times did not break the test piece. Here, the stress ratio is a ratio of the minimum stress over the maximum stress and the stress amplitude is the amplitude of the variable stress waveform shown in Fig. 5. Fig. 6 shows the stress-endurance diagram of the fatigue test. The fatigue strength of the developed material was 405 MPa, which was 2.25 times the control (180 MPa). The fatigue strength of the developed product is equivalent to molten steel, SCM440 thermal refined steel.

4.3 Improvement of mechanical properties by cold working

We attempted to improve mechanical properties of the sintered compact made in Section 4.1 by applying cold working to reduce pores. The cold working was applied after sintering and before thermal processing. Fig. 7 shows an overview of cold working. The sintered compact is placed between the outer restraint jig and the compression jig. The sintered compact was rolled by 0.25 mm, pressing the sintered compact by rolling the compression jig; then carburized tempering/annealing was applied.

Fig. 8 shows the cross section micrograph. By this cold working, the compact was densified in the area 0.5 mm from the surface, which is twice the rolling amount with porosity of less than 0.5%. The fatigue strength after cold working was 450 MPa, which is more than a 10% improvement from 405 MPa before cold working.

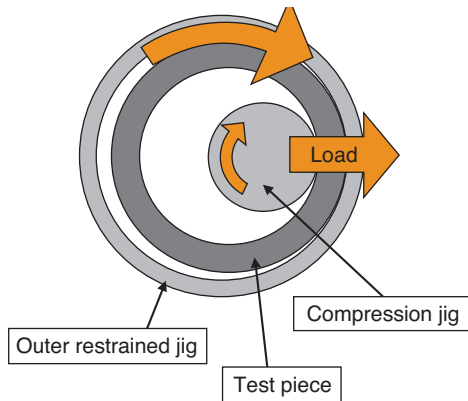


Fig. 7 Schematic cold working

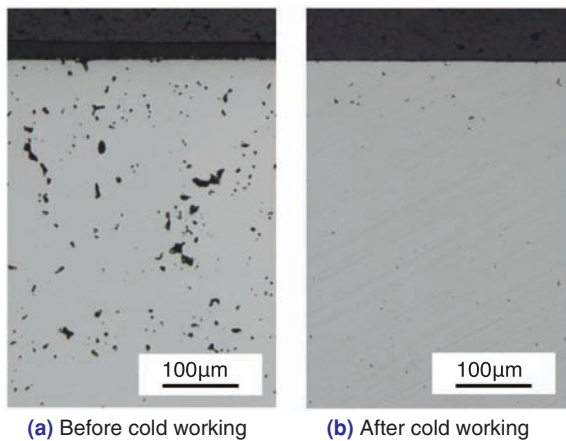


Fig. 8 Optical micrographs of sintered part

5. Conclusion

In this paper, we presented densification/strengthening methods of sintered machine parts and mechanical properties of high-density sintered machine parts. We have obtained high-density sintered compacts by applying optimum methods in each process and we have obtained fatigue strength equivalent to molten steel SCM440 thermal refined steel. In addition, it is possible to further improve strength by applying cold working, etc.

We are poised to expand application of this developed material to the machine parts that require high strength, as well as to continue developing materials with even higher performance and expanding their applications as well.

References

- 1) Kazunori Arai, Toru Shimizu: SOKEIZAI Industrial Yearbook 2013, 5. Powder Metallurgy, Sokeizai, 55, 5 (2014) 52-58.
- 2) Edited by: Japan Society of Powder and Powder Metallurgy: A Handbook of Powder and Powder Metallurgy, Uchida Rokakuho (2010) 236.
- 3) Hidenori Kuroki, Shinya Fujisawa: The Mechanism of Dimensional Changes of Iron-Copper Powder Compacts during Sintering, Powder and Powder Metallurgy, 38, 5 (1991) 571-576.
- 4) Edited by The Japan Society for Heat Treatment: Guidebook for Heat Treatment, Taiga Publishing (2008) 13.
- 5) Hironori Suzuki, Yoshikazu Seki, Kazuhisa Fujisawa: Properties of "KHD-Segless" Warm Compaction Steel Powder, R&D Kobe Steel Engineering Reports, 52, 3 (2002) 70-73.
- 6) Akira Fujiki, Yukihiko Maekawa, Yoshimi Sugaya, Takashi Shibano: Development of Warm Compacted P/M Sprocket for Automotive Engines, Journal of the Japan Society of Powder and Powder Metallurgy, 51, 7 (2004) 507-514.
- 7) Mikio Kondoh: Development of High Accuracy, High Density Powder Compaction Technology, Journal of the Japan Society of Powder and Powder Metallurgy, 54, 7 (2007) 506-512.
- 8) Takeshi Hattori, Shin Tajima, Mikio Kondoh, Masaki Sugiyama, Toshiya Yamaguchi, Hidefumi Kishimoto, Tomo Okochi, Takanobu Saito, Satoshi Takemoto, Yuichiro Fujita: Development of High-Density and Low-loss Powder Magnetic Core for Reactor in Hybrid Vehicles, (1) Si volume of Fe_Si based compact core and impact on molding pressure, Proceedings of Japan Society of Powder and Powder Metallurgy, Autumn 2009 Conference, Nagoya 2009, (2009) 99.
- 9) Edited by: Japan Society of Powder and Powder Metallurgy: A Handbook of Powder and Powder Metallurgy, Uchida Rokakuho (2010) 245.
- 10) Edited by: Japan Society of Powder and Powder Metallurgy: A Handbook of Powder and Powder Metallurgy, Uchida Rokakuho (2010) 154.

Photo of authors



Tadahiro OKUNO
Advanced Technology
R&D Center



Naoki YASHIRO
Advanced Technology
R&D Center

High Performance Magnetic Core for Induction Hardening Devices

Takuji HARANO*



Nihon Kagaku Yakin Co., Ltd. of the NTN group develops various magnetic materials satisfying demand properties. In this report, it is attached to the heating coil part of the induction hardening device and introduces about a high-performance magnetic core in a magnetism characteristic and a mechanical characteristic to be used for control of the quenching depth.

1. Introduction

Machine structural parts, such as bearings and gears, are strengthened by the thermal process for improving reliability. The drive parts for automobiles are required to have strength in certain areas of complex shapes; therefore, the best thermal process is applied to the required area with induction hardening.

Magnetic material called "core" is attached to the heating coil of induction hardening equipment ("magnetic core"). In this paper, we are presenting a high performance magnetic core that exhibits superior magnetic characteristics as well as mechanical strength developed for induction hardening.

2. Magnetic core for induction hardening heating coils

One of the induction hardening parts for automobiles is a drive shaft. **Fig. 1** shows some examples of its application.

A magnetic core installed on the back of the heating coil of induction hardening equipment can accelerate induction heating by concentrating magnetic flux on the work.

On the other hand, if it is installed on the front of the heating coil, it can block the magnetic flux to prevent heating where hardening is not needed. Therefore, it is an essential component for heating coil of induction hardening equipment.

When the target work has a complex shape and the depth of hardening area needs to be adjusted, induction heating can be completed by adjusting the shape, size,

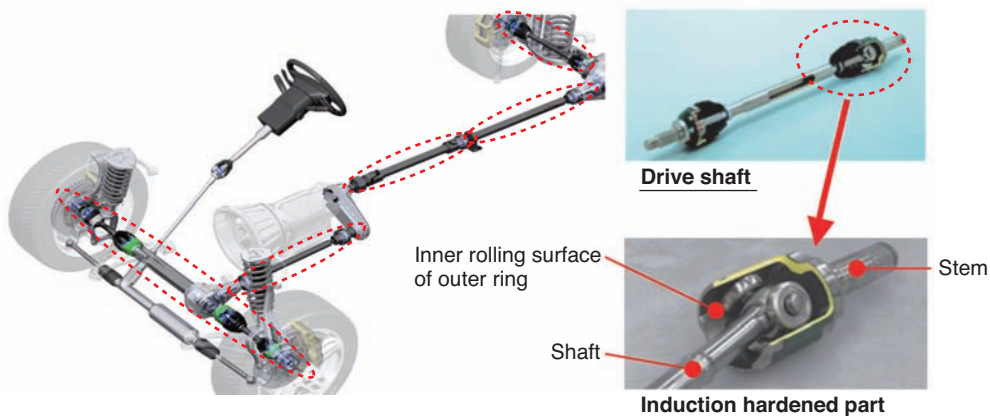


Fig. 1 Example of induction hardened parts (Drive shaft)

* Engineering Dept., Nihon Kagaku Yakin Co, Ltd.

number, direction and position of the installed magnetic cores. This controls the hardening depth of the work.

Nihon Kagaku Yakin Co., Ltd. developed high performance magnetic core by combining iron powder and thermosetting resin as shown in Fig. 2.

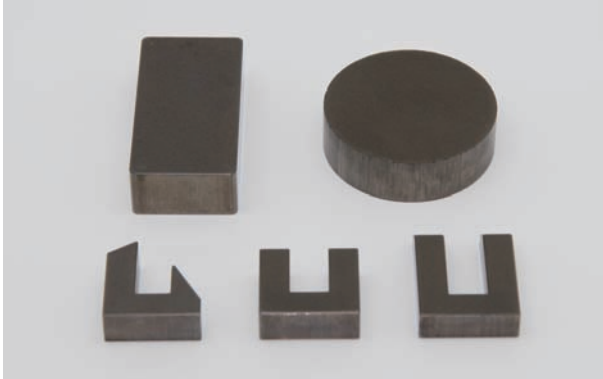


Fig. 2 High performance magnetic core

3. Development of high performance magnetic core

3.1 Background of the development

Commonly used ferrite based magnetic core has relatively small iron loss even in the high frequency range. However, a larger size may be required to maintain hardening performance due to its low saturation magnetic flux density. Magnetic steel sheet cannot be used, even if it has high magnetic flux density, because the iron loss becomes larger in the higher frequency range.

Commercially available cores or base material of powder compact based cores manufactured by powder metallurgy are frequently used as magnetic cores installed on heating coils of induction hardening equipment. They are expensive, exhibit low material strength, and are challenging to machine and handle.

Therefore, our task was to develop magnetic cores that have better characteristics than the conventional material, can be produced with a simple manufacturing process, and are suitable for volume production.

3.2 Development concept

Since the magnetic cores for heating coils of induction hardening equipment are used in the high frequency range (several kHz to 100 kHz), the following characteristics are required:

- (1) High saturation magnetic flux density
- (2) High relative permeability
- (3) Good frequency response (small variation of inductance against variation of frequencies)
- (4) Low iron loss
- (5) Superior mechanical strength

3.3 Features and performance of developed magnetic cores

3.3.1 Structure and features

Fig. 3 shows the structure of the developed high performance magnetic cores.

We used iron powder for powder metallurgy as the magnetic powder, added a small amount of thermosetting resin with high adhesive effect, and applied insulating layer on the iron powder surface by granulation process. This is a composite material which reduces the damage to the insulation layer by applying compaction molding at low pressure and thermal hardening.

This process brought a magnetic material that is strong yet has low contacts among magnetic powders. It has low iron loss, even in the high frequency range, so that the material can be used in a broad frequency range.

The features of the developed high performance magnetic cores are as follows:

- Saturation magnetic flux density: 1300 mT
- Relative permeability: 54
- Iron loss [10KHz/200mT]: 1480 kW/m³
- Radial crushing strength: 150 MPa

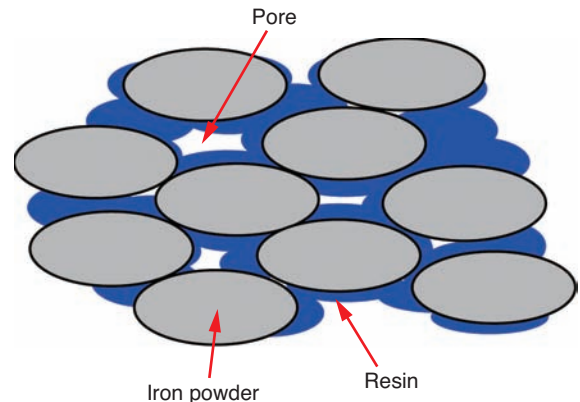


Fig. 3 Structure of the high performance magnetic core (Image)

3.3.2 Performance

(1) Magnetic characteristics

(i) Saturation magnetic flux density, relative permeability

Table 1 shows a comparison of the saturation magnetic flux density and relative permeability of the developed and conventional products. Fig. 4 shows the graph indicating the relation between the magnetic flux density B and magnetic field strength H (B-H curve).

The developed product improved approximately 10% in saturation magnetic flux density and approximately 30% in relative permeability over the conventional product. In addition, the rise of the magnetic flux density B is faster over the magnetic field strength H indicating its high efficiency. When the developed magnetic core is installed on the back of the heating coil of the induction hardening equipment introduced at the beginning of this paper, it can accelerate induction heating by concentrating magnetic flux on the work.

Table 1 Saturation magnetic flux density and relative permeability

Material	Saturation magnetic flux density mT	Relative permeability
Developed material	1300	54
Conventional material	1200	40

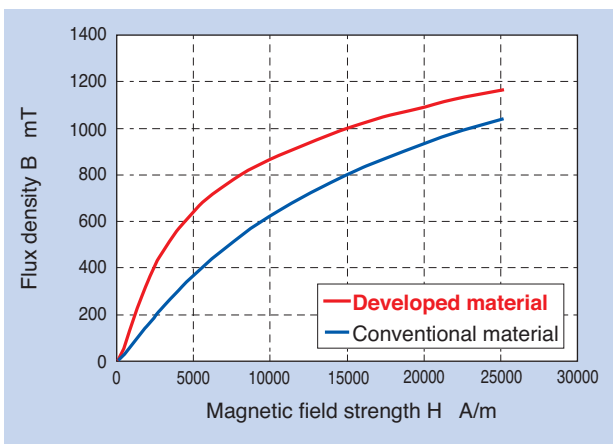


Fig. 4 B-H curve

(ii) Variation of inductance

Fig. 5 shows the rate of inductance variation, which serves as a measure of the magnetic field generation capability in the high frequency range, among the frequency characteristics of the magnetic material.

The rate of inductance variation of the developed material is equivalent to the conventional material in all ranges, including the high frequency range, with both materials showing small inductance variation up to about 100 kHz.

As a result, it was revealed that this characteristic is stable up to the high frequency range.

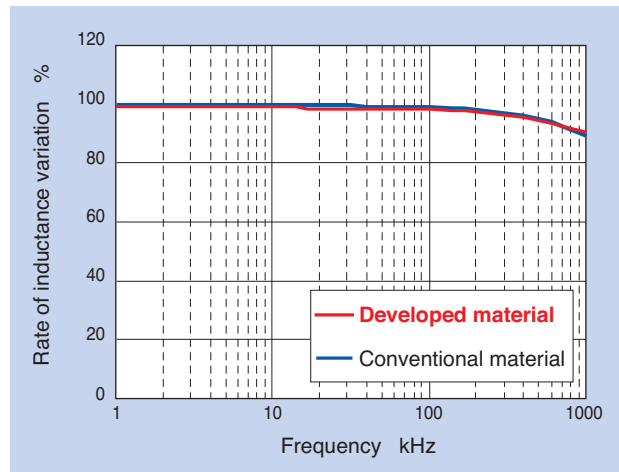


Fig. 5 Frequency characteristics

(iii) Iron loss

Fig. 6 shows iron loss of the developed and conventional materials in the high frequency range (10 kHz) equivalent to the induction hardening condition.

The iron loss of the developed product at 200 mT was approximately 15% smaller than the conventional material indicating less energy loss; a favorable result.

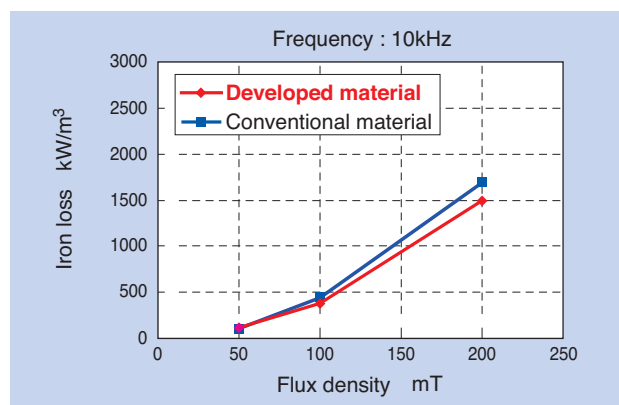


Fig. 6 Iron loss

(2) Mechanical strength

The developed magnetic core is a strong material, where iron powders are adhered with thermosetting resin and hardened, as mentioned above. The mechanical strengths of the developed and conventional materials were compared by obtaining radial crushing strength (Fig. 7), applying compressive stress on the annular test piece, and using the following equation:

$$K = \frac{F(D-e)}{L \cdot e^2}$$

K : Radial crushing strength (MPa)
 F : Maximum load at break (N)
 L : Length of hollow cylinder (mm)
 D : Outer diameter of hollow cylinder (mm)
 e : Wall thickness of hollow cylinder (mm)

The result is shown in Table 2. The radial crushing strength of the developed material is approximately 5 times stronger than the conventional material.

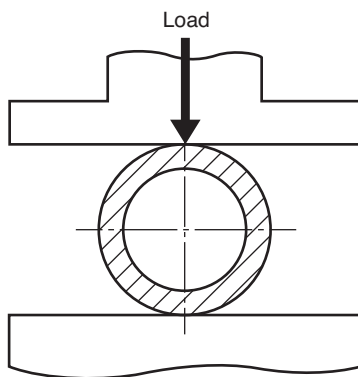


Fig. 7 Method for radial crushing strength measurement

Table 2 Mechanical strength

Material	Density g/cm ³	Radial crushing strength MPa
Developed material	6.1	150
Conventional material	6.4	30

4. Conclusion

In this paper, we presented the high performance magnetic core with superior magnetic and mechanical characteristics to be installed on the heating coil of inductance hardening equipment.

The developed magnetic core showed superior magnetic characteristics compared to the conventional product and significantly improved mechanical strength. By applying this high performance magnetic core to inductance hardening equipment, we believe we can achieve not only stable quality and improved reliability of inductance hardened components but also reduced size of these materials through enhanced strength and hardness of the structural components. This will contribute to manufacturing lighter vehicles.

References

- 1) Takayuki Oda, Shinji Miyazaki, Eiichiro Shimazu: The Reactor Core for HEV Boost Converter, NTN TECHNICAL REVIEW No. 81 (2013) 46-51
- 2) Takuji, Harano, Shinji Miyazaki, Hajime Katsuura: Introduction of Magnetic Material Products, NTN TECHNICAL REVIEW No. 80 (2012) 87-91
- 3) Shin Tomogami: Technical Trends in Constant Velocity Universal Joints and the Development of Related Products, NTN TECHNICAL REVIEW, No. 75 (2007) 10-15.
- 4) Japan Electronics and Information Technology Industries Association: Soft Magnetic Metal Materials

Photo of author



Takuji HARANO
 Engineering Dept.,
 Nihon Kagaku Yakun Co, Ltd.

The Copper-Iron-based Material Equivalent to Bronze-based Material for Sintered, Oil-impregnated Bearings

Tomonori YAMASHITA*



The materials of the sintered oil-impregnated bearing are classified into bronze-based, copper iron-based and iron-based in general. Bronze based materials are superior in sliding and acoustic feature, the problem is the copper powder is high cost compared with iron powder, so it was necessary to reduce its quantity. By adopting special copper powder, we developed new materials having same or surpassing sliding and acoustic features as in the existing bronze-based materials, even with the small amount of copper inside. This report introduces the sintered oil-impregnated bearing using developed materials.

1. Introduction

Sintered, oil-impregnated bearings are widely used in automobiles and industrial machines and their materials are broadly classified into bronze-based, iron-based and copper-iron-based, which combines the former two materials. When superior sliding performance is required in a bearing application, such as electric parts (power windows, fan motors, etc.), copying machines, or laser printers, bronze-based material is suitable. However, because of the recent increase in the cost of copper, NTN has developed a new material as an alternative to bronze for sintered bearings. In this paper, we present the properties of this copper-iron-based material equivalent to bronze sintered material for sintered, oil-impregnated bearings.

2. Material of Sintered, Oil-impregnated Bearings

Among sintered, oil-impregnated bearings, bronze-based material is superior in its sliding properties, iron-based material is superior in its durability, and copper-iron-based material has both properties.

On the other hand, since the price of iron is less expensive than copper, the sliding properties, durability, and cost are in a trade-off situation. NTN determined the correct composition of copper and iron based on the applicable use and conditions considering the balance

between sliding properties, durability, and cost, from the base copper-iron-based material.

3. Features of Special Copper Powder

Table 1 shows the composition of the developed material and **Fig. 1** shows the cross section of a bearing using a special copper powder based on this developed material composition. The upper side of the figure is the bearing bore surface, where a thin layer of copper can be observed. The special copper powder tends to aggregate on the surface of the powder compact; therefore, a green compact can be produced in the regular molding process without needing any special processes, such as plating. On the other hand, many general copper and iron powders added in the blending process are contained inside the compact.

Fig. 2 shows the bearing bore surface. Copper is exposed on approx. 60% or more of the bore surface which contributes to the excellent sliding properties.

*Engineering Dept., NTN Powder Metal Corporation

Table 1 Chemical components of the developed product

Developed material	Chemical components wt%			
	Cu	Sn	C	Fe
	15~22	0.5~2.5	0.5~2.5	Remainder

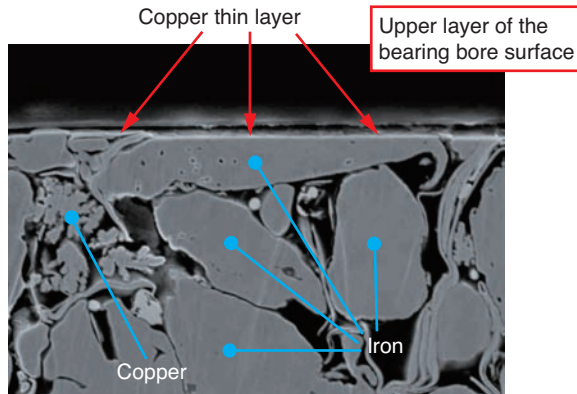


Fig. 1 Section of the developed material

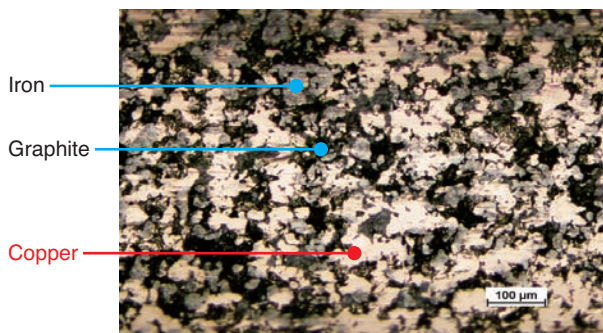


Fig. 2 Macro photograph of bearing bore

4. Performance of the Developed Bearings

We considered initial fitness, limiting PV value, wear resistance, and low temperature properties when evaluating the performance of the developed products.

4.1 Initial Fitness

The sintered, oil-impregnated bearings have a high friction coefficient at the beginning of operation which gradually decreases. This phenomenon is called initial fitness.

Since motors are required to have stable operation characteristics, a low friction coefficient from the beginning of operation and early stabilization is required. Therefore, we evaluated the initial fitness of the developed product.

In addition to the developed product, we also evaluated bronze-based material and copper-iron-based material containing 20% copper, equivalent to the developed product. The result is shown in **Fig. 3**.

The friction coefficient of the developed material was the lowest at the beginning of operation and it was the same as the bronze-based material at the time before stabilization. In addition, the friction coefficient 10 minutes later was at the same level as the bronze-based material and even lower than the copper-iron-based material containing an equivalent amount of copper.

From these results, it was found that the developed product has excellent initial fitness and that its friction properties are equivalent or superior to the bronze-based material.

<Test condition>

- Peripheral speed: 75 m/min
- Contact pressure: 1.2 MPa
- Bearing size: φ6×φ12×6J
- Shaft material: SUS420J2
- Test temperature: Room temperature
- Test time: 10 min.

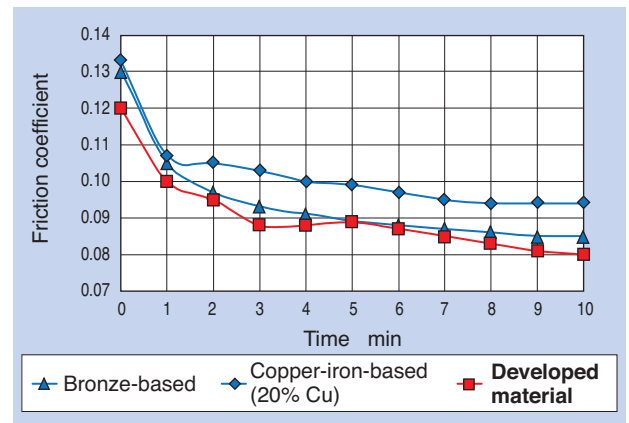


Fig. 3 Result of initial fitness evaluation

4.2 Limiting PV Value

PV value, which is an index to determine the operation limit of the bearings, is indicated by the product of the contact pressure applied to the bearings P and peripheral speed V.

The larger the value, the tougher the operation condition.

Fig. 4 shows the measurement results of the limiting PV value of different bearings. This test is conducted by maintaining a constant rotational speed and applying a load on the bearings. After a predetermined time, if the friction coefficient becomes stable, the weight of the load is increased. This is repeated. If the friction coefficient does not stabilize after the predetermined time, the PV value at that time is considered as the limiting PV value.

The friction coefficient of the developed material behaved the same way as the bronze-based material and was lower than the copper-iron-based material containing an equivalent amount of copper. In addition, the limiting PV value of the developed material was significantly higher than the bronze-based product and equivalent with the copper-iron-based material.

From this result, it can be determined that the developed material has an equivalent friction coefficient as the bronze-based material in the low PV value range and maintains a low friction coefficient in the high PV value range, as well. Therefore, it can be used in the broad PV value range.

<Test condition>

- Shaft material: SUS420J2
- Bearing size: $\phi 6 \times \phi 12 \times 6$
- Test temperature: Room temperature

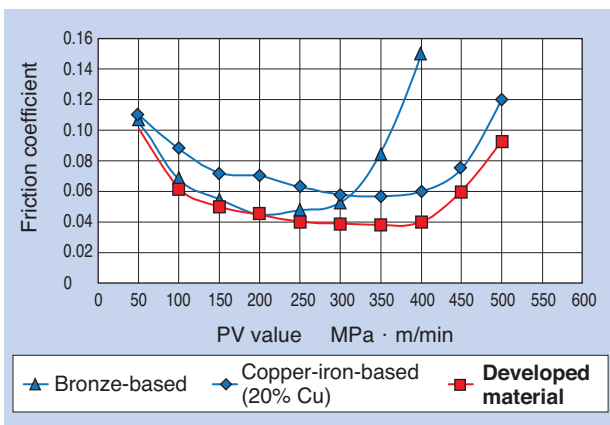


Fig. 4 Result of limiting PV value measurement

4.3 Wear Resistance

For the evaluation of wear resistance, the wear was estimated from the difference of the bearing bore diameter before and after the operation test. Fig. 5 shows the evaluation results.

It was found that the wear amount of the developed product is less than that of the bronze-based material and copper-iron-based material, presenting excellent wear resistance.

<Test condition>

- Peripheral speed: 38 m/min
- Contact pressure: 4.0 MPa
- Bearing size: $\phi 6 \times \phi 12 \times 6$
- Shaft material: SUS420J2
- Test temperature: Room temperature
- Test time: 8 hours

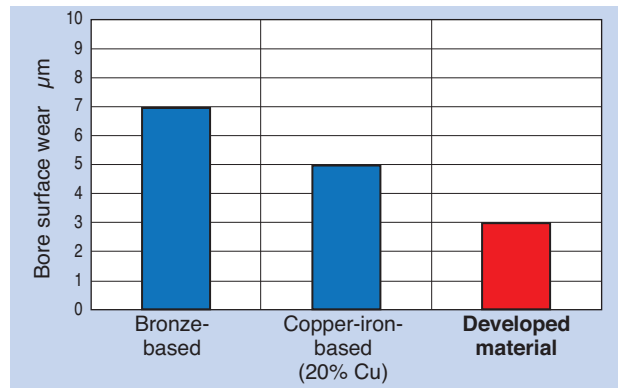


Fig. 5 Result of wear resistant evaluation

4.4 Low Temperature Properties

When used in an automotive application, a noise may be produced at the beginning of operation in low ambient temperatures - (abnormal noise at a low temperature). The cause of this noise is considered to be the metal-on-metal contact between the shaft and the bearings.

With sintered, oil-impregnated bearings, the rotational shaft is supported by the oil film formed between the shaft and the bearings which may contract in low temperatures, causing less lubrication and resulting in metal-on-metal contact.

Fig. 6 shows the measurement result of oil film forming rates in low temperature, as an evaluation of oil film forming behavior. As a comparison, the measurement result in room temperature is also shown. The oil film forming rate of 100% indicates non-contact and 0% indicates full contact.

In Fig. 6 (1), it was found that the oil film forming rate of the bronze-based product was poor, indicating metal-on-metal contact even 30 minutes later. On the other hand, the developed product showed a good oil film forming rate right after the beginning of the test, transitioning to a non-contact state in an early stage. As a result, we consider that the developed product has superior oil film forming properties to bronze-based product in low temperatures, contributing to low noise and vibration in a low-temperature environment. In addition, as shown in Fig. 6 (2), the developed product indicates better oil film forming properties than the bronze-based product suggesting superior operational life and wear resistance.

<Test condition>

- Shaft material: S45C
- Contact pressure: 0.51 MPa
- Peripheral speed: 93.4 m/min
- Shaft material: SUS420J2
- Test time: 30min.
- Test temperature: room temperature, -40°C

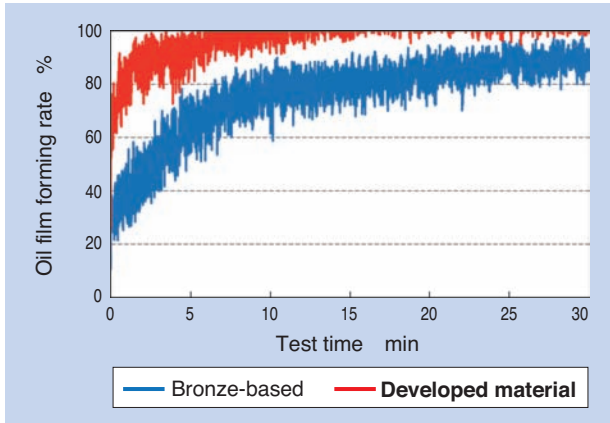


Fig. 6 (1) Result of oil film forming evaluation (-40°C)

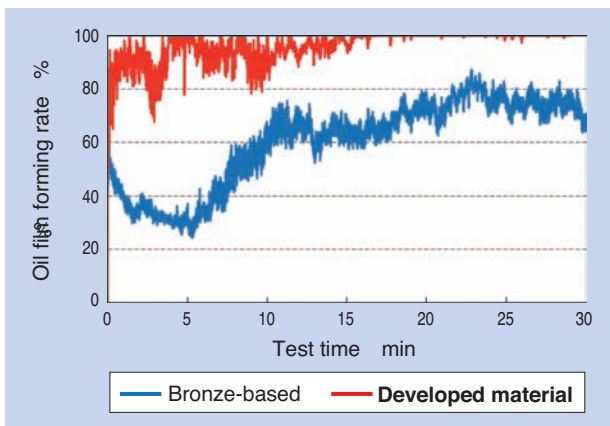


Fig. 6 (2) Result of oil film forming evaluation (Room temperature)

5. Expansion of Applications of the Developed Product

The features of the developed product as observed in the evaluation results of the previous section are as follows:

- (1) Equivalent friction properties as the bronze-based product
- (2) Equivalent limiting PV value properties as the copper-iron-based product
- (3) Superior wear resistance
- (4) High oil film forming properties in low temperatures

Because of these features, the application of the developed material can be expanded into diverse areas as an alternative to bronze-based material. In particular, its application in electric motors, such as the starter motor, is expected due to its good low-temperature characteristics.

In industrial machines, it can also be applied to the small diameter motors where large loads are applied, such as vibration motors and stepping motors.

6. Conclusion

In this paper, we presented the newly developed copper-iron-based material equivalent to bronze sintered material for sintered, oil-impregnated bearings. We are poised to expand our sales by leveraging the unique features of these products and continue our development aiming at further enhancement.

Photo of author



Tomonori YAMASHITA
Engineering Dept.,
NTN Powder Metal Corporation

High Load Sliding Bearing Unit For Use in Copier and Printer Fusers

Kei HATTORI*
Takuya ISHII**



As one of the cost reduction for business machine typified in copiers and printers, rolling bearings is required replaceable from sliding bearings. Because of using bearing conditions at fuser roller of medium and high-speed models are very hard, it is difficult to apply the sliding bearing. Therefore, NTN developed “High Load Sliding Bearing Unit”, that combined the metal inner ring and PPS resin outer ring, has twice load capacity, lower friction and wear properties in comparison with conventional resin sliding bearings. This article introduces the characteristic and performance of “High Load Sliding Bearing Unit”.

1. Introduction

With the increased demand for lower cost copiers and printers manufacturers are examining replacing rolling bearings in the fuser roller with sliding bearings. However the operating conditions in the fuser roller is demanding and the use of sliding bearings is not always possible. The use of either rolling bearings or resin sliding bearings 1) is determined depending on the specification of the model. Since resin sliding bearings have inferior load carrying capacity when compared with rolling bearings, the use of resin sliding bearings is limited to relatively light-load models.

In this paper, we will present a “High Load Sliding Bearing unit” with improved load carrying capacity. This bearing combines an outer ring made of polyphenylen sulfide (PPS) resin and an inner ring made of metal.

into the paper. The heat from the heating roller is transferred to the fuser roller through the belt. This makes the fuser roller hotter than the pressure roller. The bearings support both the fuser roller and the

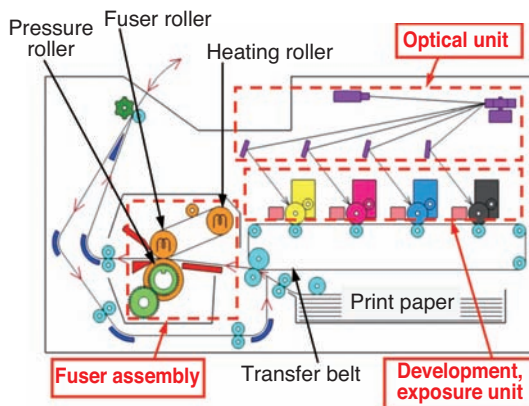


Fig. 1 Laser beam printer

2. Bearing specifications and issues for the fuser roller

2.1 Bearing specifications for the fuser roller

Fig. 1 shows the design of a laser beam printer while Fig. 2 shows the design of a fuser assembly. The image captured in the optical unit is replicated onto the transfer belt with toner in the development and exposure unit. The replicated image is then moved from the transfer belt and fixed onto paper at the fuser roller. During this process, the paper passes between the fuser roller and the pressure roller, is heated to approximately 200°C and has the toner/image pressed

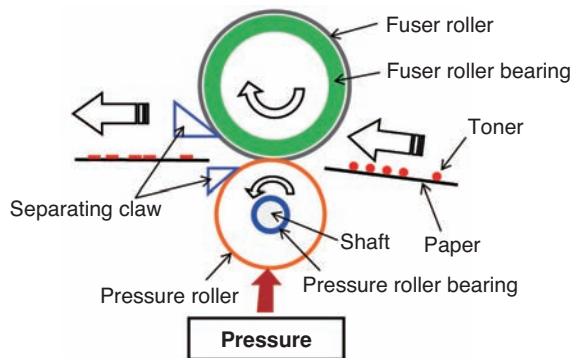


Fig. 2 Fuser assembly

*Composite Material Engineering Dept., Composite Material Products Division

**Engineering Dept. NTN Engineer Plastic Corp.

pressure roller are supported by. and In operation the pressure roller is pressed onto the fuser roller, usually by springs that transmit the force through the bearings. Therefore, the bearings of the fuser roller and pressure roller are always pressed in one direction and are used under shaft rotation.

2.2 Issues for bearings in the fuser roller

Resin sliding bearings are widely used in low-speed machines with maximum printing speeds of 30 sheets per minute, since the load on the pressure roller is relatively low. However as the printing speed increases both the temperature and pressure of the fuser roller increases in order to quickly print the toner. It becomes difficult for sliding bearings to survive under these operating conditions necessitating the move to, rolling bearings that possess higher load capacities.

There are other issues that a designer needs to consider when using resin sliding bearing in the application such as different friction/wear characteristics depending on the material of the bearing, the shaft fit, shaft surface roughness and uneven wear due to deflection and/or misalignment of the shaft.

3. Features of the high load sliding bearing unit

Fig. 3 shows the design of the high load sliding bearing unit while Fig. 4 shows a partial cross section. The high load sliding bearing unit is composed of two components, a PPS resin based outer ring and a metal based inner ring. The two components contact between the inner convex spherical surface of the outer ring and the outer concave spherical surface of the inner ring. Operating clearance is provided between the outer ring and the inner ring to accommodate thermal expansion while lubrication is supplied by grease applied to the sliding surface. By making the outer concave spherical surface of the inner ring larger than the inner convex spherical surface of the outer ring the contact area (and friction) is reduced. The clearance in the bearing allows for the formation of a grease sump resulting in stable friction condition.

Table 1 shows the materials of the outer ring, the inner ring and the grease. The electrical characteristics required for bearings mounted in copiers and printers vary depending on the design. To accommodate these different designs there are two types of high load sliding bearing units each with different materials for the outer ring and for the grease, namely, non-conductive and conductive. The respective outer rings use the BEAREE AS materials shown in Table 2. These are PPS resins with superior high temperature properties and special additives to improve friction/wear

properties. The material for the inner ring is common bearing steel while a fluoride based grease is used. With this design and materials, we have improved friction/wear properties of the bearing, made it usable under the high load conditions, and given the bearing a self-aligning property, as well.

Table 3 provides a comparison between resin sliding bearings, a high load sliding bearing unit and rolling bearings. The high load sliding bearing unit, which has a hybrid structure, has the following features compared with the resin sliding bearings:

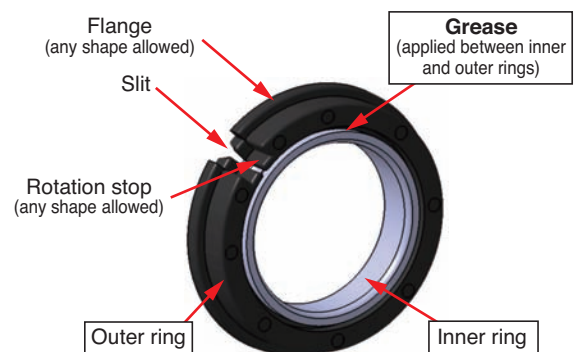


Fig. 3 Structure of high load sliding bearing unit

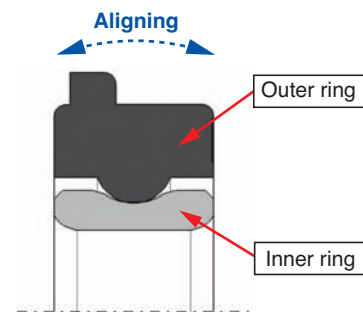


Fig. 4 Cross section of high load sliding bearing unit

Table 1 Constituent material

Component	Non-conductive type	Conductive type
Outer ring	BEAREE AS5056 (non-conductive)	BEAREE AS5965 (conductive)
Inner ring	Bearing steel	Bearing steel
Grease	Non-conductive fluoride based grease	Conductive fluoride based grease

Table 2 Basic properties of outer ring resin material

Item	Unit	BEAREE AS5056	BEAREE AS5965
Volume resistivity	$\Omega \cdot \text{cm}$	$\times 10^{14}$ or more	$\times 10^3$
Specific gravity	—	1.58	1.62
Tensile strength	MPa	58	43
Coefficient of thermal expansion	$\times 10^{-5}/^\circ\text{C}$	8.7	7.3
Thermal conductivity	W/(m · K)	0.32	0.38

Note: The above properties (room temperature) are the typical values.

(Features)

- (1) A superior friction/wear property in a high temperature environment
- (2) Twice the load carrying capacity
- (3) High degree of freedom for designing shafts (shaft material and surface roughness does not impact bearing performance)
- (4) Consistent sliding property with aligning design

Table 3 Comparison of features various bearings

Item	Resin sliding bearing	High load sliding bearing unit	Rolling bearing
Structure	Single resin	Resin based outer ring Metal based inner ring	Metal based outer ring Metal based inner ring Steel ball
Load carrying capacity	△	○	◎
Friction property	△	○	◎
Wear property	△	○	◎
Degree of freedom for shaft design	×	○	○
Aligning property	×	○	△
Thermal insulation	◎	◎	△
Cost	◎	○	△

◎ Excellent ○ Good △ Fair × Poor

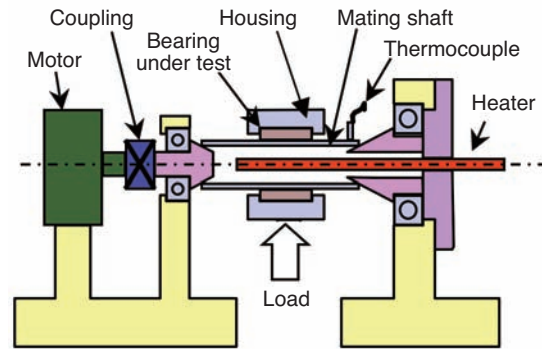


Fig. 5 Radial test machine

Table 4 Test condition

Item	Description
Shaft rotational speed	16.5 m/min (210min ⁻¹)
Contact pressure	0.95 MPa (166N)
Mating shaft	Aluminum alloy
Temperature	180°C (surface of mating shaft)
Time	20h

4. Performance of high load sliding bearing unit

4.1 Friction/wear property

Fig. 5 shows the test machine used for measuring the friction coefficient and wear amount. The bearing under test was installed in the housing, to which load was applied upward from underneath the housing. Then the shaft was rotated to measure the friction coefficient and resulting wear. The bearing under test had an inner diameter of 25 mm and width of 7 mm. The inside of the shaft was heated and the surface temperature was controlled using a thermocouple.

Table 4 shows the test conditions. The friction coefficient and amount of wear for both the high load sliding bearing unit (developed product) and the resin sliding bearing (conventional product) were measured. Both the developed product and the conventional product are of the non-conductive type. The conventional product is a sliding bearing made of PPS resin with polytetrafluoroethylene resin blended in.

Fig. 6 shows the amount of wear and dynamic friction coefficient for the bearings. We defined the amount of wear in the developed product by measuring the increase in the operating clearance between the inner and outer ring from the test. The amount of wear and the dynamic friction coefficient of the developed product were 1/3 and 1/2, respectively, when compared to the conventional product.

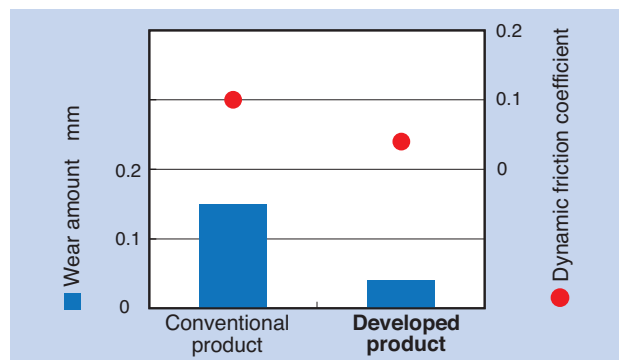


Fig. 6 Friction and wear property

4.2 Limiting PV property

One important operating condition of sliding bearings is known as the PV value. This is defined as a product of the contact pressure at bearing sliding surface P and the sliding velocity V. The limiting PV values were evaluated under the test condition shown in **Table 5**. We defined allowable contact pressure as the maximum contact pressure where the increase of the operating clearance between the inner and outer rings from the test was 0.1 mm or less, through a number of tests with different loads at the predetermined rotation speeds. Here, the contact pressure is a value of load divided by the product of the inner diameter and width of the bearing.

Fig. 7 shows the P-V curve, which shows the relation between the rotation speed of the shaft and allowable contact pressure of the developed product and compares this with the PV curve for conventional product. This test revealed that the developed product is superior in load carrying capacity as the allowable

contact pressure was twice that of the conventional product.

Fig. 8 shows the time-dependent change of dynamic friction coefficient of the developed product with the shaft rotation speed of 10 m/min and contact pressure of 1.66 MPa. This revealed that the dynamic friction coefficient was low and consistent at approximately 0.06.

We also evaluated bearings of the conductive type. The conductive type bearings showed equivalent friction/wear results and limiting PV values as the conductive type.

Table 5 Test condition

Item	Description
Shaft rotational speed	5m/min (64min ⁻¹) 10m/min (128min ⁻¹) 16.5m/min (210min ⁻¹)
Mating shaft	Aluminum alloy
Temperature	200°C (surface of mating shaft)
Time	100h

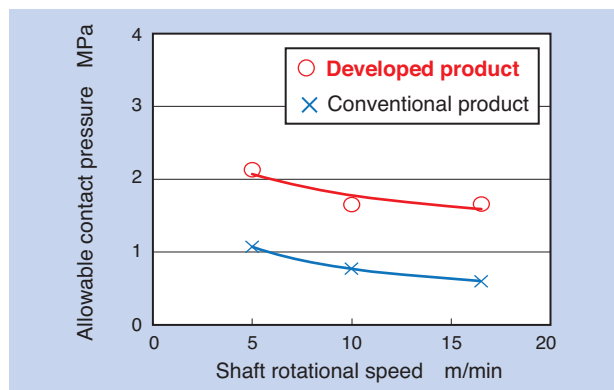


Fig. 7 Limiting P-V curve

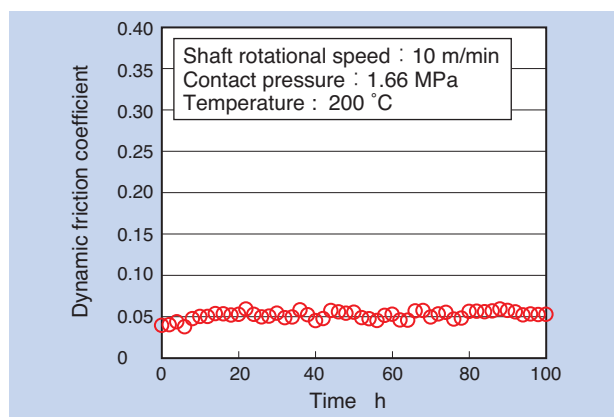


Fig. 8 Coefficient of dynamic friction

5. Dimension of bearings

Table 6 shows an example of dimensions for a high load sliding bearing unit mainly used in the fuser rollers for copiers and printers. This table shows bearings with

dimensions similar to those of equivalent rolling bearings. However it should be noted that it is also possible to provide thinner bearing units with smaller outer diameters. This is achieved by reducing the thickness of both the outer and inner rings. In addition, as the outer ring is manufactured by injection molding, the size and shape of the flange and rotation stop can be arbitrarily changed and the number of peripheral components, such as the retaining ring, may be reduced.

However, since the resin outer ring has a slit, a rotation stop needs to be provided on the outer ring .

Table 6 Dimensions of high load sliding bearing unit

Inner diameter	Main dimensions mm			Allowable aligning angle mm/mm
	Outer diameter	Flange outer diameter	Width	
20	32	34.8	7	1/100
25	37	39.8	7	1/100
30	42	44.8	7	1/100
35	47	49.8	7	1/100

Notice : Allowable misalignment is a reference level to vary according to condition of use.

6. Conclusion

We have developed a high load sliding bearing unit with significant improvement on the load carrying capacity and friction/wear properties in a high-temperature environment. Additionally the new bearing allows for a high degree of freedom in designing the shaft and alignment accuracy. With this development, we are able to provide an alternative to rolling bearings for the fuser rollers of copiers and printers.

In addition, the high load sliding bearing unit can be applied to various other applications by changing materials of the components. NTN is looking at expanding the use into food processing equipment and medical equipment.

References

- 1) Yoshio OKI, Takumi HAYASHI, Takuya ISHII: Characteristics and Applications of Super Engineering Plastics, Journal of Japanese Society of Tribologists 49 (7), (2004) 31.

Photo of authors



Kei HATTORI

Composite Material Engineering Dept.,
Composite Material Products Division



Takuya ISHII

Engineering Dept.
NTN Engineer Plastic Corp.

Machine Tool Main Spindle Bearings with Air Cooling Spacer



Yushi ONDA*
 Kikuo FUKADA*
 Yohei YAMAMOTO**
 Masato YOSHINO***

NTN developed “Machine Tool Main Shaft Bearing with Air Cooling Spacer” with the air cooling technology for machine tool main spindle bearings, which realizes high-speed and high-rigidity at the same time with higher level than ever. In this paper, bearing cooling effect through the technology and technical activities for practical use are introduced below with tests and analysis results.

1. Introduction

For machine tool main spindles, high rigidity and high precision are required for machining difficult-to-cut materials and parts with complex shapes. The characteristics of the machine tool main spindles vary depending on the machining content and the target workpiece because, for example, the machining of molding for machine parts and components for medical equipment requires high-speed and high-precision rotation. Therefore, the demand for equipment with multiple machining capabilities such as 5-axis processing machines and field-assisted machining equipment is increasing. The main spindles and bearings are required to have high-speed performance and high rigidity.

To increase rigidity of the bearings, it is effective to raise preload during assembly and to increase the payload capacity of the bearings. However, those measures may cause high heat during operation, preventing high speed operation and degrading machining accuracy due to thermal expansion of the main spindles. Therefore, it is important to reduce heat during operation in order to achieve high-speed operation with increased rigidity of the bearings.

NTN has been working on higher speed, higher rigidity and lower noise for the bearings of the main spindles by improving air oil lubrication^{1),2)}. We have

now developed a “cooling spacer³⁾” by applying cooling technology for bearings as a new approach. In this paper, we present the structure and mechanism of “machine tool main spindle bearings with air cooling spacer” which is an improved version of this development to the practical level.

2. Structure

Fig. 1 shows the structure of the bearings with air cooling spacer. NTN’s proprietary environment friendly air oil nozzle⁴⁾, which enables reduction of air volume, oil quantity and noise, is applied to the outer ring spacer installed between back-to-back angular contact ball bearings (DB arrangement), in addition, air cooling nozzles are installed independent from the air oil nozzle.

The air cooling nozzles are arranged offset from the center of the shaft at three locations on the circumference toward the direction of rotation. The room temperature air (hereafter, “cooling air”) injected from the air-cooling nozzles passes between the inner spacer and outer spacer and through the bearings swirling toward the direction of the rotation to cool the bearings.

*Machining Tool/Aerospace Engineering Dept., Industrial Machinery Division

**Industrial Machinery Engineering Dept., Industrial Machinery Division

***Advanced Technology R&D Center

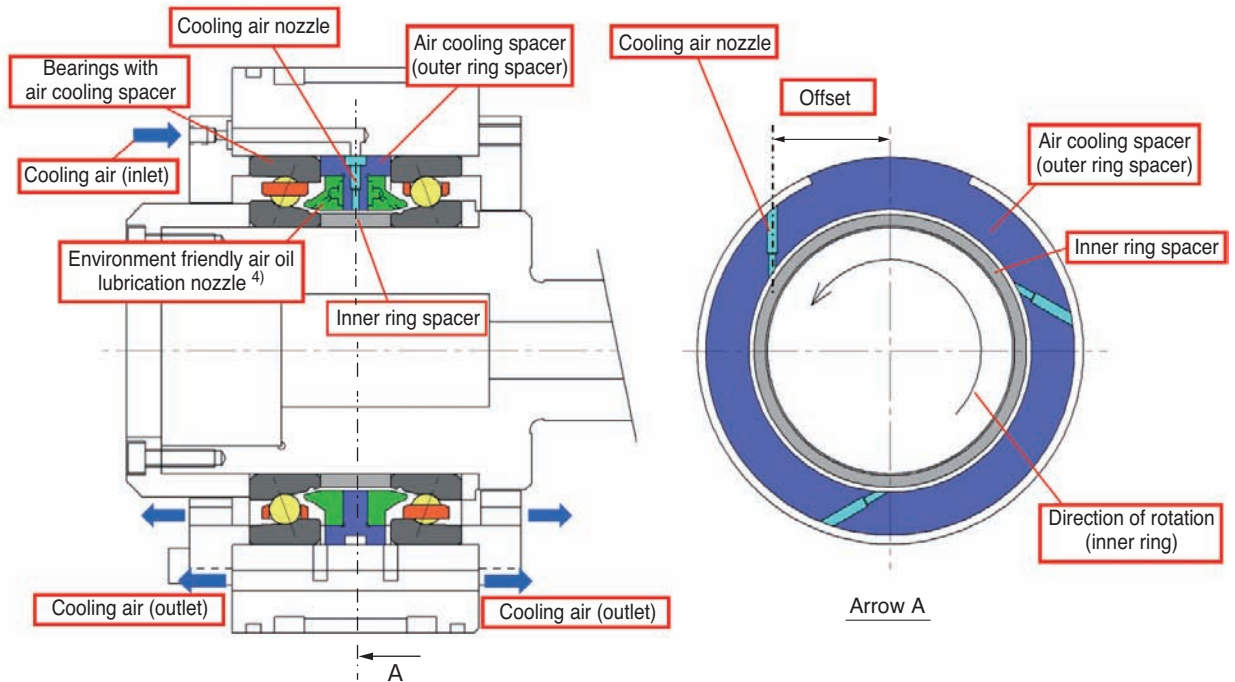


Fig. 1 Structure of the bearing with air cooling spacer

3. Cooling mechanism

The bearings with air cooling spacer take the heat generated from the bearings from the surface of the inner ring spacer with the cooling air. When the cooling air stays longer in the spacer, the heat exchanging time between the cooling air and the surface of the inner ring spacer increases, which improves the cooling effect of the bearings. In addition, faster air flow increases the heat taken out of the surface of the inner ring spacer per hour, increasing cooling efficiency of the inner ring spacer and the bearing inner ring.

We have modeled the cooling air flow inside the bearings with air cooling spacer by fluid analysis. The

result is shown in Fig. 2.

If the air cooling nozzles are not offset from the spindle center, the cooling air diffuses toward the axial direction after colliding against the outer surface of the inner ring spacer, and then the air is exhausted out of the spacer. Therefore, the bearing cooling effect from the cooling air is small.

On the other hand, when the nozzles are offset, the cooling air flows along the circumference of the outer surface of the inner ring spacer after its collision to the surface in high speed, remaining on the surface for a longer time.

Therefore, the bearing cooling effect from the cooling air is large.

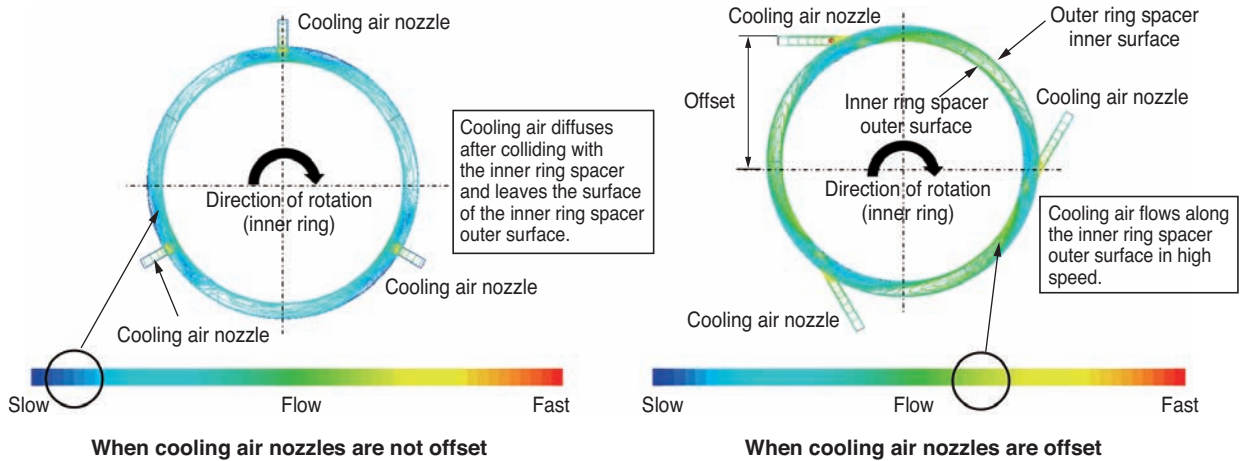


Fig. 2 Cooling air flow in bearing spacer (Fluid analysis results)

4. Cooling effect

We have conducted a high speed operation test of the bearings to verify the cooling effect of the bearings with air cooling spacer. Fig. 3 shows the structure of the tester, Table 1 shows the test conditions, and Fig. 4 and Fig. 5 show the rise of temperature and noise level of the bearings, respectively. The offset level of the nozzles is determined to be 80% of the outer radius of the inner ring spacer based on past test results¹⁾.

In Fig. 4, the temperature rise of the inner ring is small when cooling air is supplied, compared with no cooling air. From this result, we verified that the difference of the temperature between the inner and outer rings at the rotation speed of 23,000 min⁻¹ (d_{mn} value of 2,070,000) decreases approx. 14°C when the cooling air flow of 300 NL/min is supplied.

By this reduction of temperature difference between the inner and outer rings, the maximum contact pressure of the inner ring runway surface from inside the bearings during operation can be reduced by approx. 35% and the maximum rotational speed can be increased by approx. 20%. In addition, the bearing preload during assembly of the main spindle of 0 N can be increased up to approx. 1,300 N.

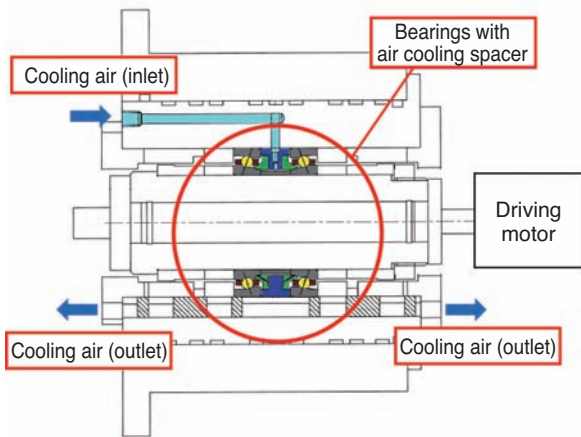


Fig. 3 Structure of test machine

Table 1 Test conditions

Bearings under test	φ70×φ110×20 Equivalent to 5S-2LA-HSL014
Pressurization method	Fixed location pressurization (pressurization after assembly ON)
Speed of rotation	0~23000min ⁻¹
Lubrication method	Air oil lubrication
Oil level	0.03ml/10min
Lubricant	ISO VG32
Lubrication air flow	30NI/min
Outer cylinder cooling	Yes, synchronized with room temperature (21±1°C)
Spindle position	Horizontal

In case of more practical cooling air flow of 100 NL/min, the temperature difference between the inner and outer rings can be reduced by approx. 4°C and the maximum contact pressure of the inner ring runway surface can be reduced by approx. 6% at 23,000 min⁻¹ (d_{mn} value of 2,070,000), therefore, the maximum rotation speed of the bearings can be increased by approx. 5%.

The bearing preload during assembly of the main spindle of 0 N can be increased up to approximately 150 N.

As a result, by adopting this technology we can achieve both high-speed and high-rigidity.

On the other hand, in Fig. 5, we verified that the noise becomes loud in the medium/low speed range, when the cooling air flow is 300 NL/min. We discuss this reduction of noise in the following section.

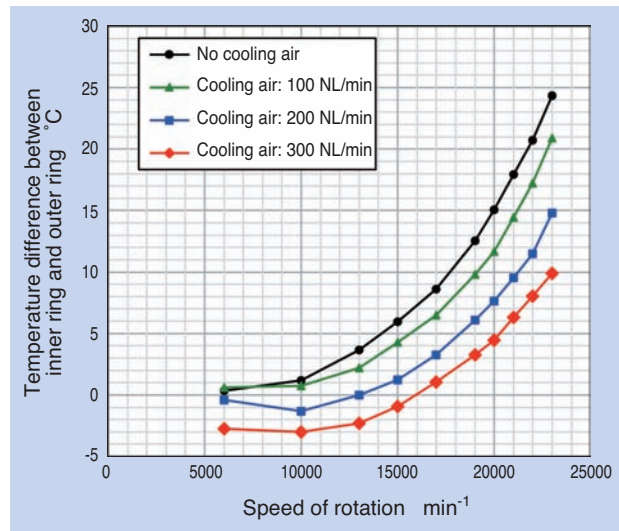


Fig. 4 Cooling air amount and temperature difference between inner ring and outer ring

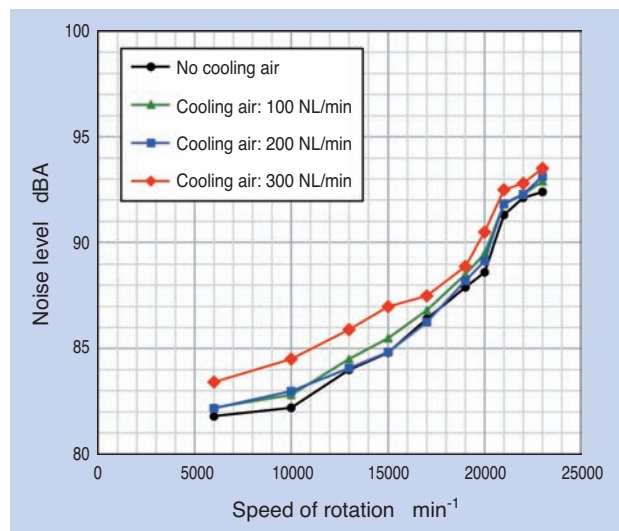


Fig. 5 Cooling air amount and noise level

5 Initiatives of noise reduction

In order to investigate the cause of the louder noise with increased cooling air flow, we modeled the cooling air flow by fluid analysis.

The analysis result when the air cooling spacer width of 22 mm is shown in Fig. 6. A part of the cooling air diffuses to the axial direction also, immediately after being injected from the air cooling nozzles flowing into the bearings maintaining the fast flow speed. It is considered that this cooling air and the air curtain produced around the rotating rolling element collide strongly with each other, which caused a lot of noise.

In order to reduce the speed of the cooling air flowing

into this bearing part, we provided a space between the inner ring spacer and outer ring spacer which extends to the circumference. Fig. 7 shows the fluid analysis result of this design. The cooling air injected to this space flows to the circumferential direction without diffusing immediately after being injected, then flows into the bearing space slowing down the speed. In this case, the collision between the cooling air flow in and the air curtain is reduced compared with the case of Fig. 6; therefore, the noise becomes low.

In order to verify the above space effect, we conducted an operational test. This result is shown in Fig. 8. We verified reduction of noise by provision of a space between the inner and outer ring spacers.

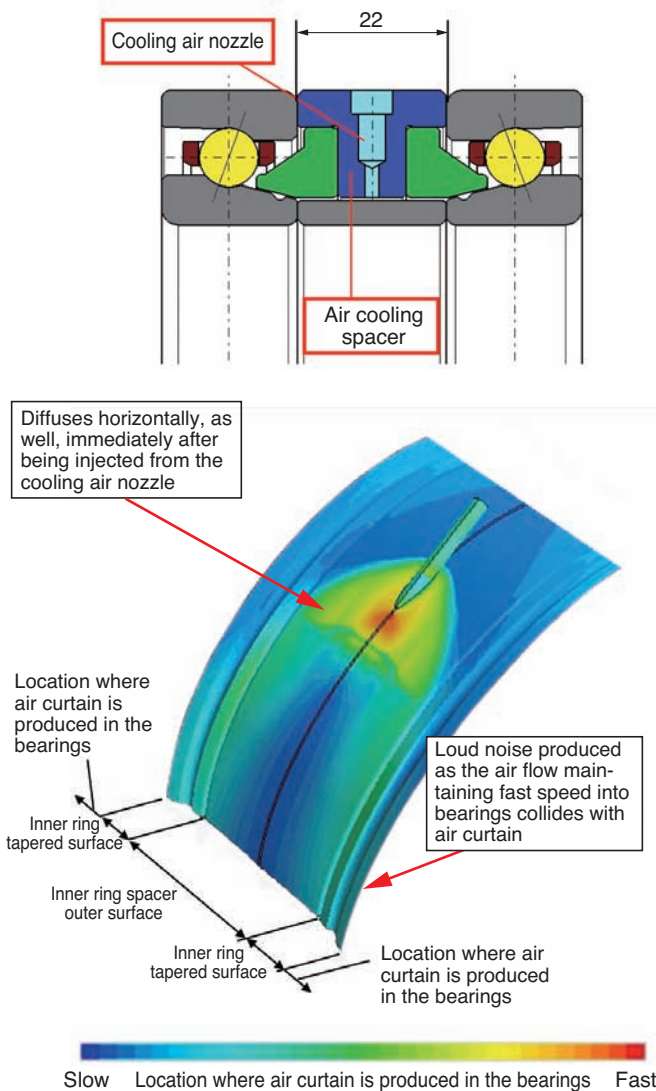


Fig. 6 Cooling air flow near inner ring spacer surface (Fluid analysis results)

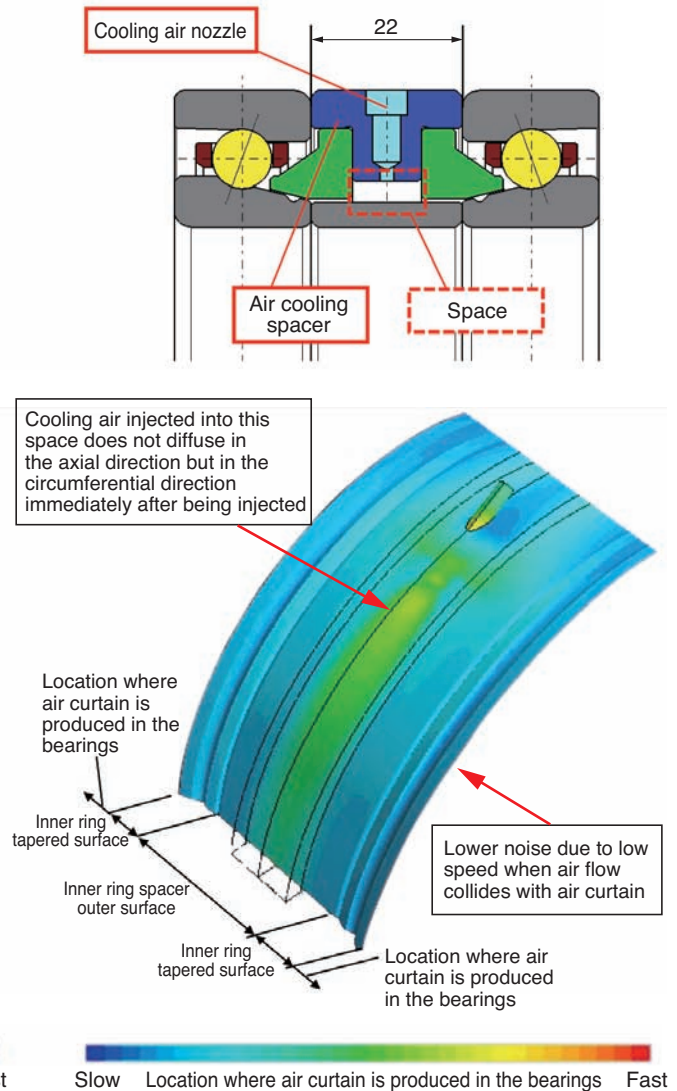


Fig. 7 Cooling air flow near inner ring spacer surface for the case of special space (Fluid analysis results)

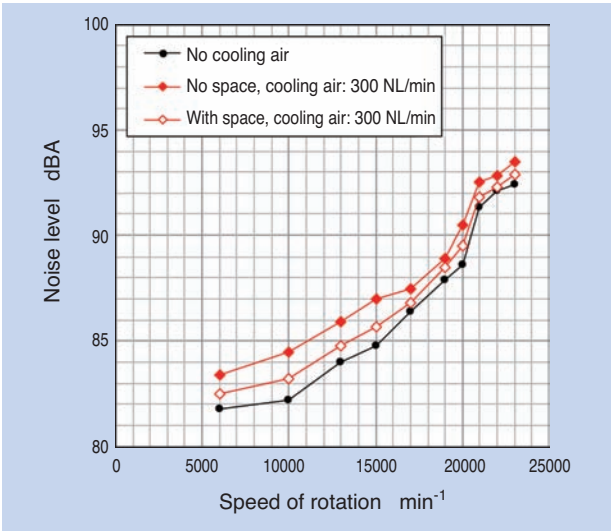


Fig. 8 Special space of air cooling spacer and noise level

6. Relation between the space width and noise

In order to verify the relation between the spacer width and noise, we conducted a test with the cooling air spacer width of 66 mm, as shown in Fig. 9, which is triple the size of the 22 mm spacer width described in the previous section. Fig. 10 shows the rise of temperature of the bearings and Fig. 11 shows the resulting noise level.

With Fig. 10, we verified that the temperature difference between the inner and outer rings is reduced by approx. 7.5°C and the maximum contact pressure of the inner raceway surface is reduced by approx. 20% at the cooling air flow of 300 NL/min and with 23,000 min⁻¹ (d_{mN} value of 2,070,000). As a result, the maximum rotation speed of the bearings can be increased by approx. 15% and the bearing preload during assembly of the main spindle of 0 N can be increased up to approx. 500 N.

Also, we verified that the temperature difference between the inner and outer rings is reduced by approx. 2.5°C and the maximum contact pressure of the inner raceway surface is reduced by approx. 5% at the cooling air flow of 100 NL/min and with 23,000 min⁻¹ (d_{mN} value of 2,070,000). As a result, the maximum rotation speed of the bearings can be increased by approx. 5% and the bearing preload during assembly of the main spindle of 0 N can be increased up to approx. 90 N. From the above, we verified the bearing cooling effect also with the cooling air spacer width of 66 mm.

On the other hand, no increase of noise level was observed with the cooling air spacer width of 66 mm, with the cooling air flow of 300 NL/min and no space between the inner and outer ring spacers, from Fig. 11.

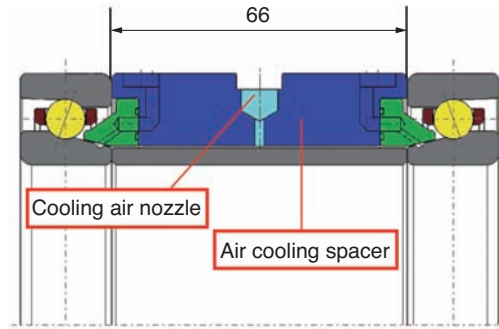


Fig. 9 Bearing with air cooling spacer of 66mm width

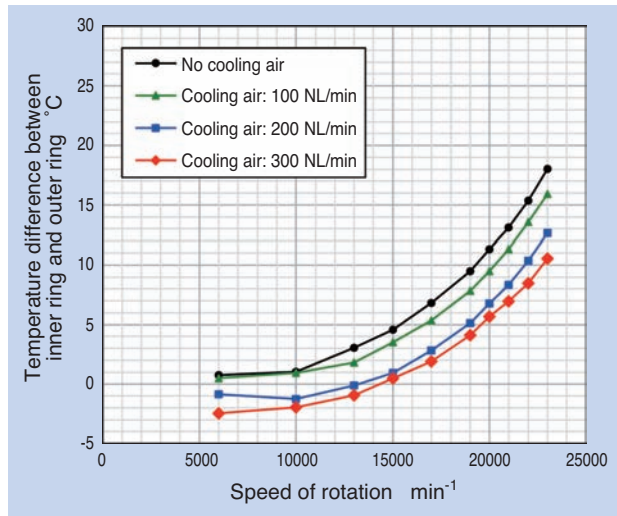


Fig. 10 Temperature difference between inner ring and outer ring of bearings with air cooling spacer 66mm width

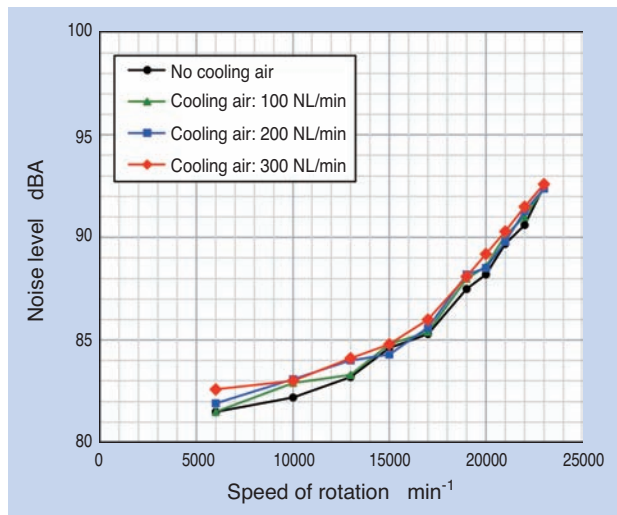


Fig. 11 Noise level of bearings with air cooling spacer 66mm width

In order to understand the reason, we analyzed the cooling air flow with the cooling air spacer width of 66 mm. The result is shown in Fig. 12. With the cooling air spacer width of 66 mm and no space between the inner and outer ring spacers, a part of the cooling air diffuses to the axial direction immediately after being injected from the cooling air nozzles. However, since the distance to the bearing part is longer and the air flow speed was reduced by the air viscosity while it passed the space between the inner and outer ring spacers, it is considered that the resulting noise due to the collision with the air curtain was reduced.

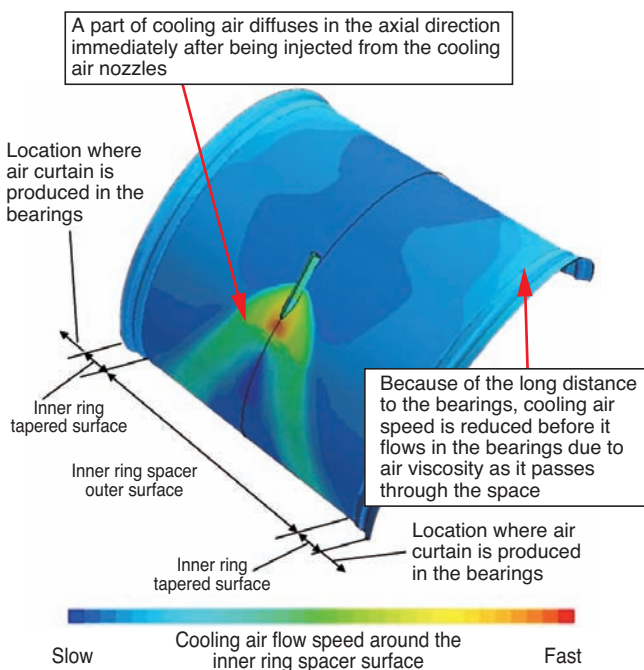


Fig. 12 Cooling air flow in bearing 66mm spacer (Fluid analysis results)

7. Conclusion

NTN achieved a high level of speed and rigidity by using the air cooling technology for the bearings of machining tool main spindles. We strive to continue contributing to "Monozukuri" as we believe that the "Machine Tool Main Spindle Bearings with Air Cooling Spacer" will contribute to higher speed, higher rigidity and higher reliability of the machine tools.

References

- 1) Kenji Fujii, Masatsugu Mori, Yoshimi Ota: Noise Reduction for Machine Tool Main Spindle Air Oil Lubrication Bearings, The Japan Society for Precision Engineering, Autumn Meeting 2000 Proceedings (2000) 449.
- 2) Yoshinobu Akamatsu and Masatsugu Mori: Minimizing Lubricant Supply in an Air-Oil Lubrication System, NTN TECHNICAL REVIEW, No 72 (2004).
- 3) Yushi Onda, Mamoru Mizutani and Masatsugu Mori: Machine Tool Main Spindle Bearings with "Air Cooling Spacer", NTN TECHNICAL REVIEW, No 80 (2012).
- 4) NTN Catalog: Precision Rolling Bearings, CAT. No. 2260-V/J 12.09.01.

Photo of authors



Yushi ONDA
Machining Tool/Aerospace
Engineering Dept.,
Industrial Machinery Division



Kikuo FUKADA
Machining Tool/Aerospace
Engineering Dept.,
Industrial Machinery Division



Yohei YAMAMOTO
Industrial Machinery
Engineering Dept.,
Industrial Machinery Division



Masato YOSHINO
Advanced Technology
R&D Center

New Engineering Plastic Cage of High Speed Angular Contact Ball Bearings for Machine Tools

ULTAGE



Wakana INOUE*
Mineo KOYAMA*
Soichiro ONITSUKA**

To support the high-speed, high-rigidity and high-reliability requirements of machine tools, NTN developed new resin cage of high speed angular contact ball bearings for machine tools. The new cage has good characteristics in high-temperature range and optimized pocket design. With the modifications, the cage can be applied higher speed range than conventional one. In this document, we introduce the design points and test data.

1. Introduction

The speed of spindle rotation for machine tools has been increasing for improving quality of the machined surface and machining efficiency as represented by the machining centers for mold manufacturing. In order to respond to these requirements, NTN has introduced high speed angular ball bearings, ULTAGE Series *1 HSE type, applying special materials and special surface treatment onto the inner and outer rings of the bearings, as well as optimum design for the internal components.

The HSE bearings adopt machined cages made of phenol resin as standard; however, for mid/low speed main spindles of dmn value (an index of the speed of rotation) of 1,000,000 or lower, cages made of polyamide resin are widely used considering the cost. We have designed cages made of newly developed polyamide resin applicable for a higher speed range where machined cages made of phenol resin have been traditionally used.

In this paper, we present features and evaluation results of the developed cages.

2. High speed angular contact ball bearings - HSE type

The high speed angular contact ball bearings - HSE type (shown in Fig.1) employs a special material featuring improved wear resistance and anti-seizure

properties, as well as a special surface modification technique for internal design of inner and outer rings to achieve higher speed, rigidity and reliability. By this adoption, higher speed operation was made possible while maintaining preload after assembly of the main spindles allowing broad use in the main spindles of high-speed lathes and machining centers.

It is possible to allow use of steel balls or ceramic balls as rolling elements and to select contact angles of inner and outer rings (15°, 20° and 25°) depending on the operational conditions of the main spindles.

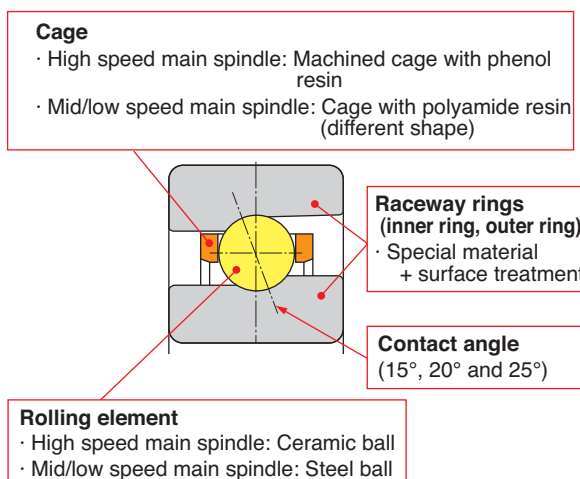


Fig. 1 High speed angular contact ball bearings HSE type

*Machining Tool/Aerospace Engineering Dept., Industrial Machinery Division

**Industrial Machinery Engineering Dept., Industrial Machinery Division

※1 ULTAGE is a name created from the combination of "ultimate" and "stage" signifying NTN's intention to pursue the ultimate performance of precision bearings.

3. Features of cages with new resin

3.1 Issues with cages made of the conventional polyamide resin

Fig. 2 shows the conditions of the cage pocket after high speed operation of bearings with the cage made of conventional polyamide resin at over 1,000,000 of dmn value. The contact area of the cage pocket and the rolling element locally melts and wears depending on operating conditions. This damages progresses as tough operation continues, and may cause abnormal rise of temperature or seizure of the bearings.

The damage process of the cage pocket is shown in Fig. 3. High speed sliding contact is observed between the cage pocket and rolling element in high speed operation of main spindles of machine tools. Fig. 4 shows the relation between the speed of the main spindle rotation and the peripheral speed of the rolling element. In case of main spindles of machining center with the main spindle diameter of 70 mm and speed of rotation 15,000 min⁻¹, the peripheral speed of the rotating element can reach approximately 35 m/s, and over 40 m/s with higher speed spindles.

In addition, the preload of the bearings increases with speed, due to the temperature difference between the inner and outer rings, which expands because of the heat generated between the rolling element and raceway and the centrifugal force applied to the inner ring and the rolling element. This leads to the increase of the load on the rolling element, which causes tighter contact between the cage pocket and the rolling element.

As a result, the heat generated in the cage pocket can locally increase, causing potentially poor lubrication, melting, and wear.

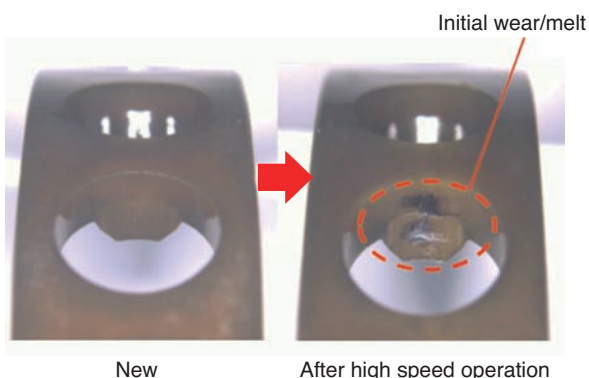


Fig. 2 Conventional cage pocket after high speed operation

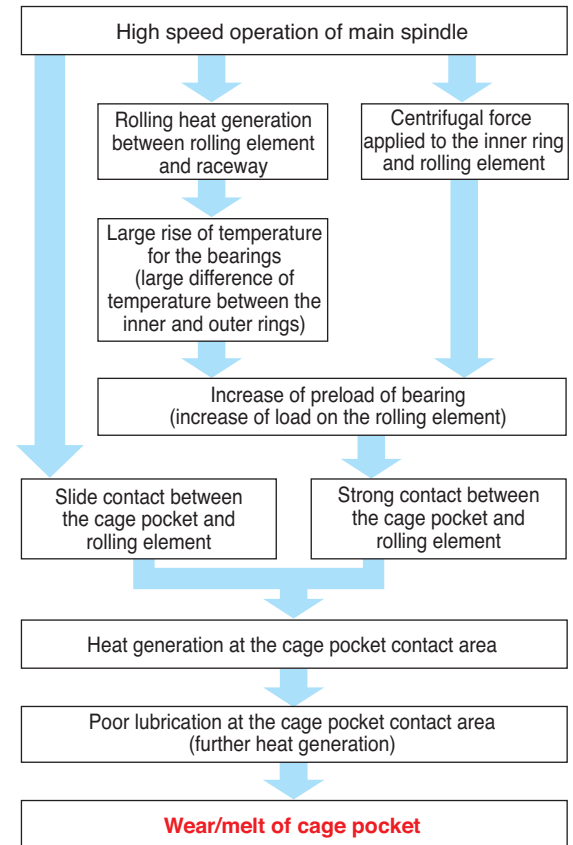


Fig. 3 Cage damage process in high speed operation

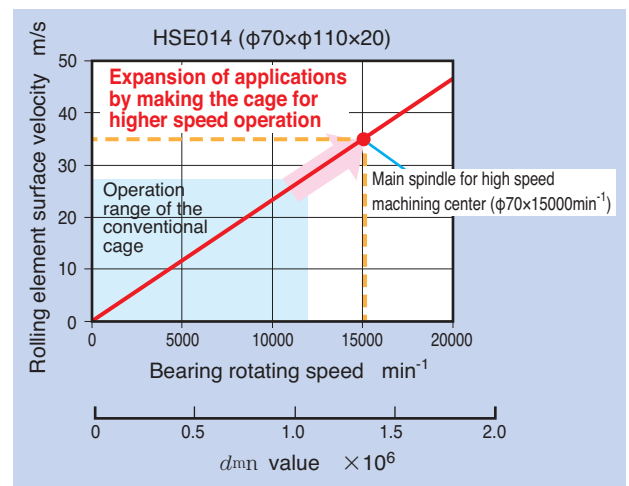


Fig. 4 Relationship between bearing rotating speed and rolling element surface velocity

3.2 Adoption of polyamide resin material with a high melting point

As mentioned in the previous section, it is necessary to apply the materials with a high glass transition point and high melting point, in particular, to prevent local wear and melt of the cage pocket, as shown in **Table 1**, for resin cages to allow higher speed of rotation.

Table 2 shows the characteristics of the developed cage material. We adopted a high melting point semi-aromatic polyamide as the material for the developed cage. It has a higher melting point and glass transition point compared with the conventional polyamide used for cages, with smaller strength deterioration and dimensional change due to high temperature.

Fig. 5 shows the relationship between the dynamic modulus of elasticity*2 to temperature.

The dynamic modulus of elasticity of polyamide for the conventional cages starts decreasing from approx. 50°C, around the glass transition temperature; however, polyamide with a high melting point for the developed cages has a higher glass transition temperature, maintaining a gradual decrease of dynamic modulus of elasticity up to around 120°C. Therefore, when the cage pocket is heated by the high speed slide contact with the rolling element, increase of the contact area with the

rolling element due to the decrease of dynamic modulus of elasticity and the resulting heating can be reduced.

To evaluate the developed cage material, we made a cage with the same shape as the conventional cages for comparison.

Fig. 6 shows the test spindle, **Fig. 7** shows the test result with air oil lubrication, and **Fig. 8** shows the test result with grease lubrication.

Even if no difference in rise of temperature was observed between two cages, the resin of the developed cages with both air oil and grease lubrication demonstrated durability for applications of higher speed than the conventional polyamide resin.

Table 1 The necessary characteristic of cage material for high speed operation

	Required properties	Purpose
1	· Low water absorption and dimensional change · Low linear expansion coefficient	Small dimensional dispersion, allows stable operation
2	· High tensile strength and flexural strength	Little deformation in high speed operation
3	· High glass transition temperature · High melting point	Little wear/melt in high speed slide contact
4	· Superior sliding property	
5	· Good injection moldability	Stable quality
6	· Low cost	Broader applicability without cost restriction

Table 2 Characteristic of cage material

Item		Conventional cage material	Developed cage material
Resin type		Polyamide	High melting point polyamide
Melting temperature Tm	°C	260	300
Glass transition temperature Tg	°C	58	125
Tensile strength	MPa	160	175
Water absorption ratio	%	2~3	0.2

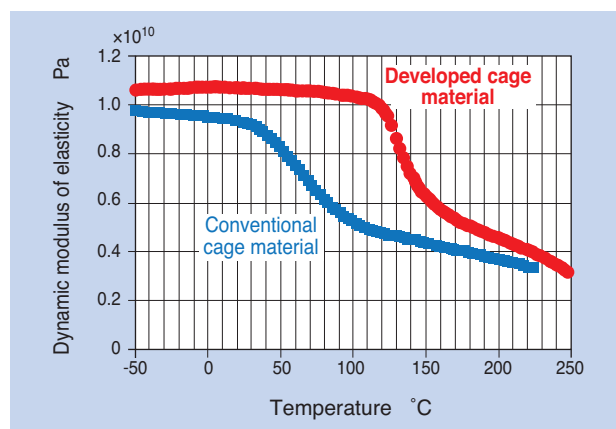


Fig. 5 Relationship between the dynamic modulus of elasticity to temperature

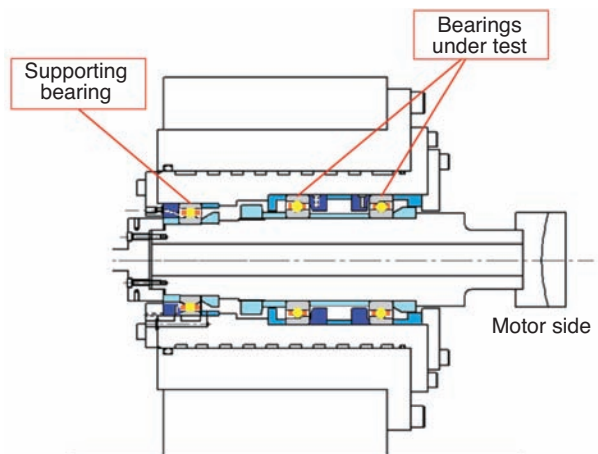


Fig. 6 Test spindle

*2 Dynamic modulus of elasticity is obtained from the response of the sinusoidal amplitude given to the test piece.

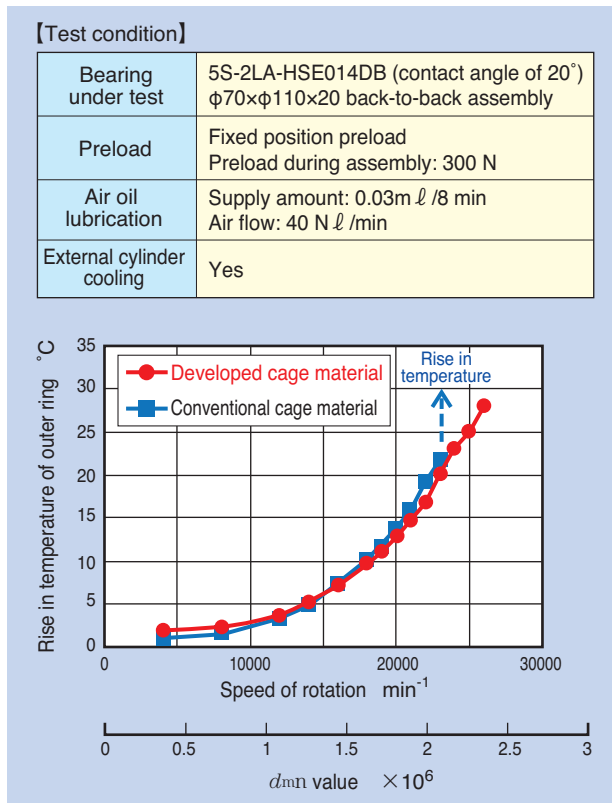


Fig. 7 Test result under air-oil lubrication with ceramic ball

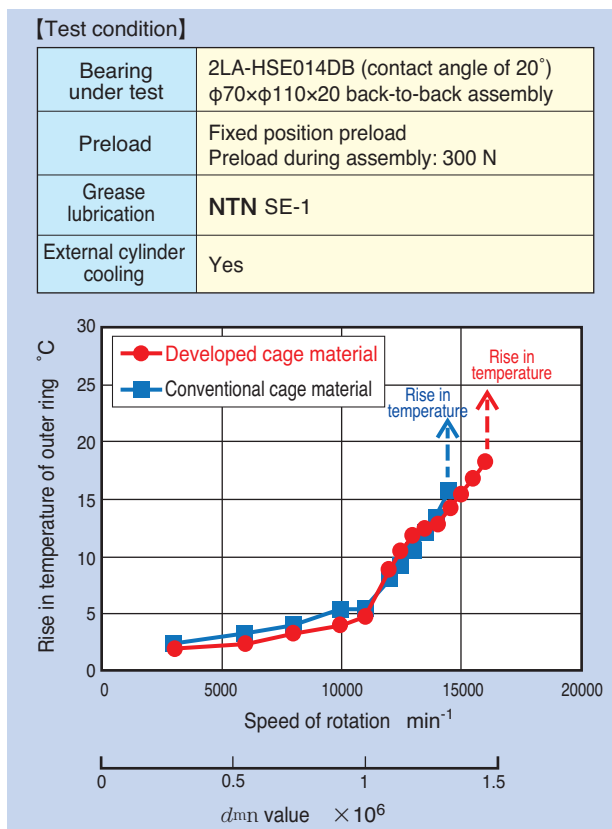


Fig. 8 Test result under grease lubrication with steel ball

3.3 Shape optimization of cages

The shape of the pocket of the developed cage is shown in Fig. 9. We have provided space for lubrication close to the contact area between the rolling element and cage pocket for the developed cage. As a result, in case of air oil lubrication, smooth supply/drain of lubricating oil was made possible at the contact point of the rolling element and the cage pocket. In case of grease lubrication, it also contributed to the retention of grease in the proximity of the contact point increasing lubrication reliability in high speed operation.

In addition, the guiding surfaces, which are the contact area of the developed cage with the rolling element in rotational and axial directions, are made flat (ref. (1) and (2) of Fig. 9) to reduce generation of heat by minimizing the contact area with the rolling element compared with the circular hole contact area of the conventional cages with polyamide resin.

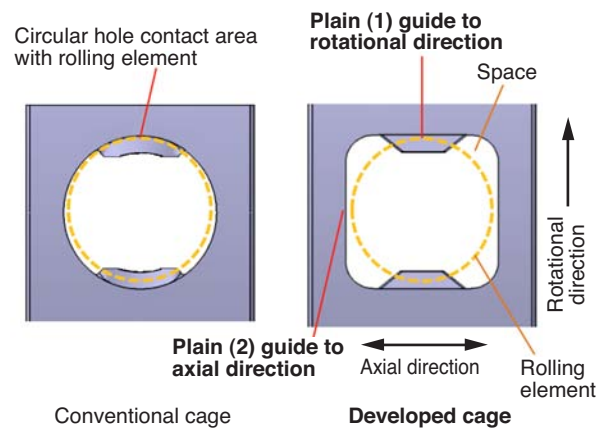


Fig. 9 Cage pocket shape

4. Performance of the developed cage

We evaluated the HSE bearings using ceramic balls with air oil lubrication and grease lubrication, and using steel balls with grease lubrication in high speed operation with the test spindle shown in Fig. 6.

The results are shown in Fig. 10, Fig. 11 and Fig. 12. We verified that the developed cage experienced reduced the rise of temperature enabling higher speed operation.

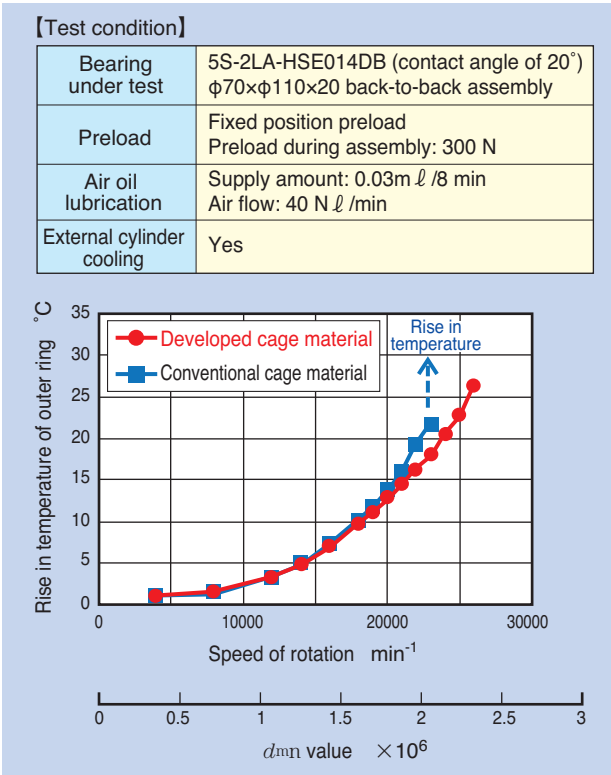


Fig. 10 Test result under air-oil lubrication with ceramic ball

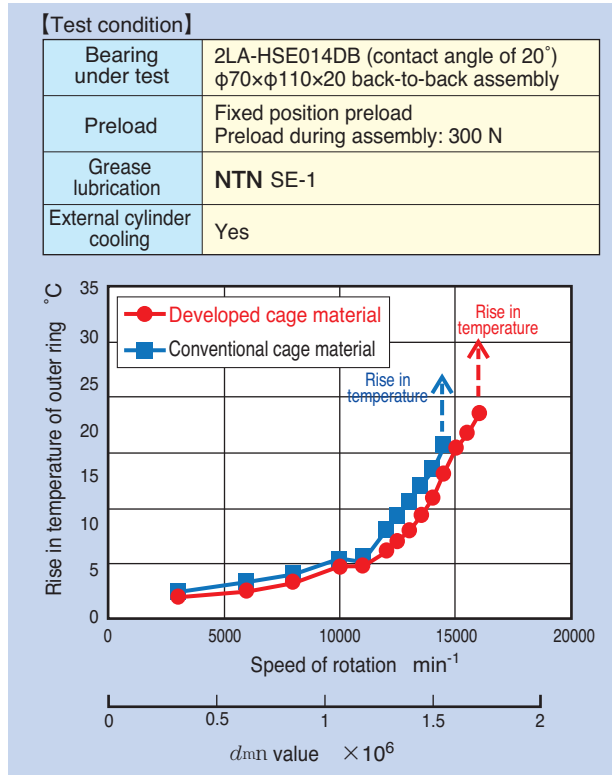


Fig. 12 Test result under grease lubrication with steel ball

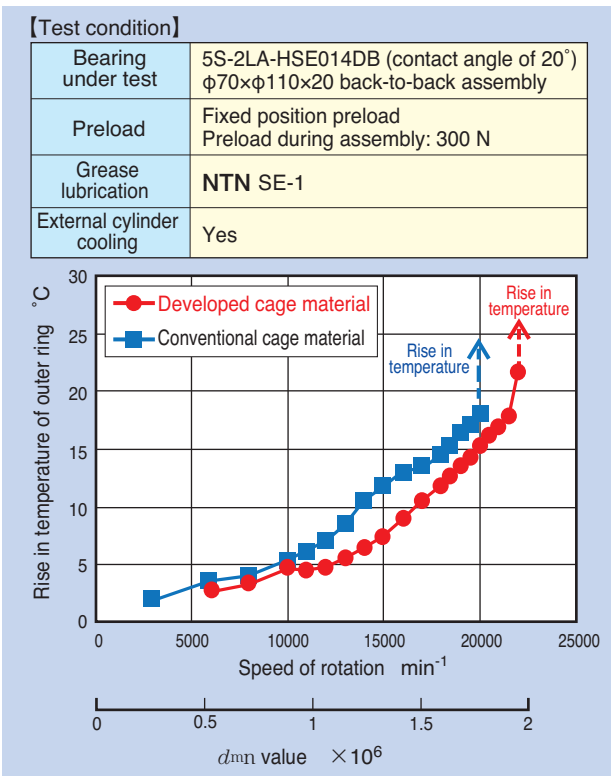


Fig. 11 Test result under grease lubrication with ceramic ball

5. Conclusion

We have improved the high speed performance of cages for high speed angular contact ball bearings for machine tools over the conventional cages made of polyamide resin by adopting high melting point polyamide resin and a new cage shape.

We have enabled cages made of newly developed polyamide resin applicable for a higher speed range where machined cages made of phenol resin have been traditionally used. We will introduce this cage using ceramic balls with air oil lubrication for HSE bearings to be used with d_{mn} value of 1,600,000.

We strive to work on further improvement of performance of the bearings for main spindles contributing to higher speed, rigidity and reliability of machine tools.

Photo of authors

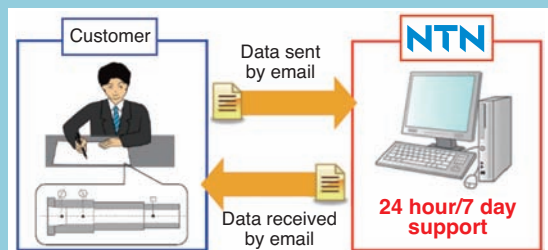


Wakana INOUE
Machining Tool/Aerospace Engineering Dept., Industrial Machinery Division

Mineo KOYAMA
Machining Tool/Aerospace Engineering Dept., Industrial Machinery Division

Soichiro ONITSUKA
Industrial Machinery Engineering Dept., Industrial Machinery Division

Bearing Technical Calculation System for Machine Tool Spindles



Keiichi UEDA*
Yushi ONDA*
Shouhei HASHIZUME*

In recent years, machine tool and spindle manufactures have been developing various products which can meet the new customer demands. To support the activities, NTN developed the bearing technical calculation system for machine tool spindles. Machine tool and spindle manufactures can calculate various characteristics like spindle rigidities and fatigue life of spindle bearings through the system in short time.

Features, mechanism and functions of the system are introduced below.

1. Introduction

The main spindles of machine tools are an essential element in determining the machining accuracy and productivity of machine tools. Their critical properties, such as rigidity, are determined by the type, arrangement, placement, preload, etc., of the bearings.

Therefore, when the manufacturers of machine tools and manufacturers specialized in spindles (hereafter, "customers") design main spindles, they need to obtain specifications of the bearings and properties of the main spindles by calculation and verify if they satisfy the target objectives.

Since these calculations are generally performed by the bearing manufacturers, they are required to calculate the properties of multiple main spindle design candidates quickly and in detail based on the information from the customers' operating conditions, etc. In addition, materials, machining processes, and machine tools users have become increasingly diversified in the recent years with additional requirements such as complex functionalities, downsizing, and environment friendliness in addition to the conventional requirements of high speed, high rigidity and high precision. In order to design main spindles that meet these requirements, more reviews and propositions are required with increasingly frequent design opportunities.

Therefore, NTN developed the Bearing Technical Calculation System for Machine Tool Main Spindles that customers can use to automatically calculate characteristics of the bearings and main spindles in a short time. This new tool will help our customers with their designs and contribute to reductions in lead time for development of machine tools.

In this paper, we present the features, configuration, and functions of this system.

2. Overview

The technical calculation system we developed can calculate characteristics of 10 main spindle bearing layouts of different types, arrangements and preload methods. The overview is shown in Fig. 1.

The customer enters data required for calculation such as the bearing type and operating conditions into the dedicated Excel®*1 file and sends it to NTN's dedicated server by email. The server automatically performs the calculation based on the input information and immediately responds back to the customer with the calculation results such as the rigidity of the main spindle and bearing life. Traditionally, NTN required at least 1 day *2 from receipt of the calculation request from the customer until the report with the calculation results was sent back to the customer. However, with this system, the response is sent back to the customer

*Machining Tool/Aerospace Engineering Dept., Industrial Machinery Division

※1 Excel® is a trademark or registered mark of Microsoft Corporation in the United States of America or other countries.

※2 Required time for technical calculation of bearings for machine tool main spindles, in general, and may vary depending on the content of bearing calculation.

within approx. 10 minutes of the customer's email request.

In this system, the server handles all processes from receipt of the email requests to automatically sending the email responses. Therefore, the time required for transferring information between the customers and NTN can be significantly reduced. Additionally, customers are free to submit as many calculations as they desire, making it possible to narrow down main spindle design plans very quickly. Furthermore, as the server is able to work on a 24 hour, 7 days a week basis, customers can use the system without no time restrictions.

Though the design process leading to the finalization can be shortened by this system, contributing to significant development lead time reductions for main spindles and machine tools, the final specifications of bearings must still be determined by discussions between the customer and NTN.

3. System features, configuration, and flow

3.1 Features

Industry-first technical calculation system with automatic processing

(1) Fast technical calculation of bearings for main spindles

10 minutes after sending a request email (traditionally, at least 1 day)

(2) Technical calculation of many types of main spindle layouts

10 types of main spindle layouts can be processed

(3) Automatic calculation within the dedicated server

24x7 operations

(4) Simple communication of input/output data

Adoption of a practical Excel® file

3.2 Configuration

This system is shown in Fig. 1 and consists of the following elements ① – ③. Any customer with Excel® (Excel 97-2003 or later) and an email system can use this system. No special settings, such as installation of dedicated programs, is required for customers: one of the benefits of this system.

- ① Dedicated server (installed at NTN)
- ② Dedicated program installed in ①
- ③ Dedicated Excel® file for exchanging input/output information between the customer and ①

3.3 Flow

The system flow is as follows: The sequence ① – ⑤ corresponds to ① – ⑤ in Fig. 1. After step ⑤, the specification of the bearing is finalized in a discussion with the customer and NTN.

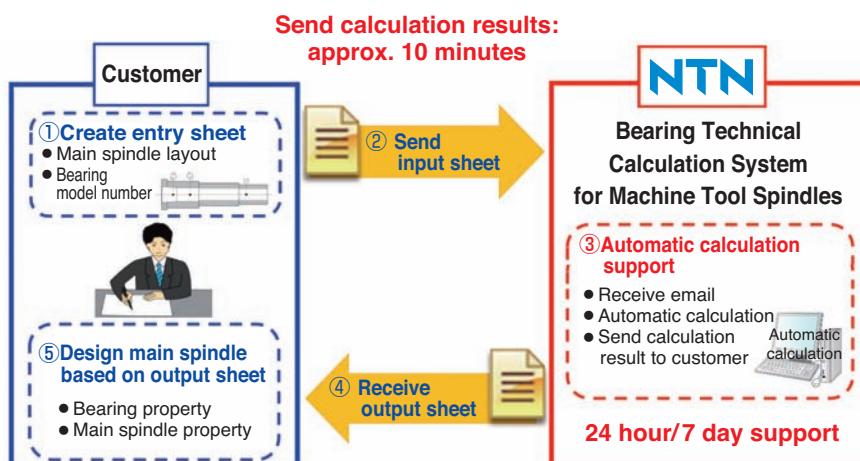
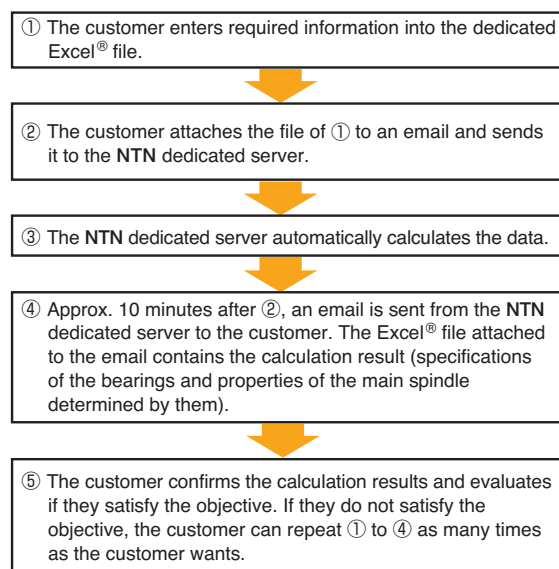


Fig. 1 System flow

4. System input/output

4.1 Input/Output items

Table 1 shows input/output items for this system.

As described in the previous section, the customer enters information in the predefined Excel® file and the system calculates and responds with the calculation results (output) to the customer.

In the input, the items and operating conditions regarding the main spindles are entered. 10 types of layouts can be selected for main spindles, as shown in Fig. 2, so various design candidates for main spindles can be created.

Preload, spring constant, and rolling contact fatigue life of bearings, as well as rigidity during assembly (radial and axial direction) to the main spindles are obtained as output. The customer verifies the result and evaluates if it meets their objectives.

Regarding the main spindle layouts, NTN is expanding the number of types moving forward.

Table 1 Input and output items

Input item	[Items regarding main spindle] · Main spindle layout Select from 10 layouts · Operating conditions Speed of rotation, external load, etc.
	[Items regarding bearings] · Bearing model number, bearing position · Preload, space · Engagement · Amount of adjustment of inner/outer ring spacer, etc.
Output item	[Bearing properties] · Preload, spring constant, rolling fatigue life
	[Main spindle rigidity] · Rigidity during assembly (radial, axial)

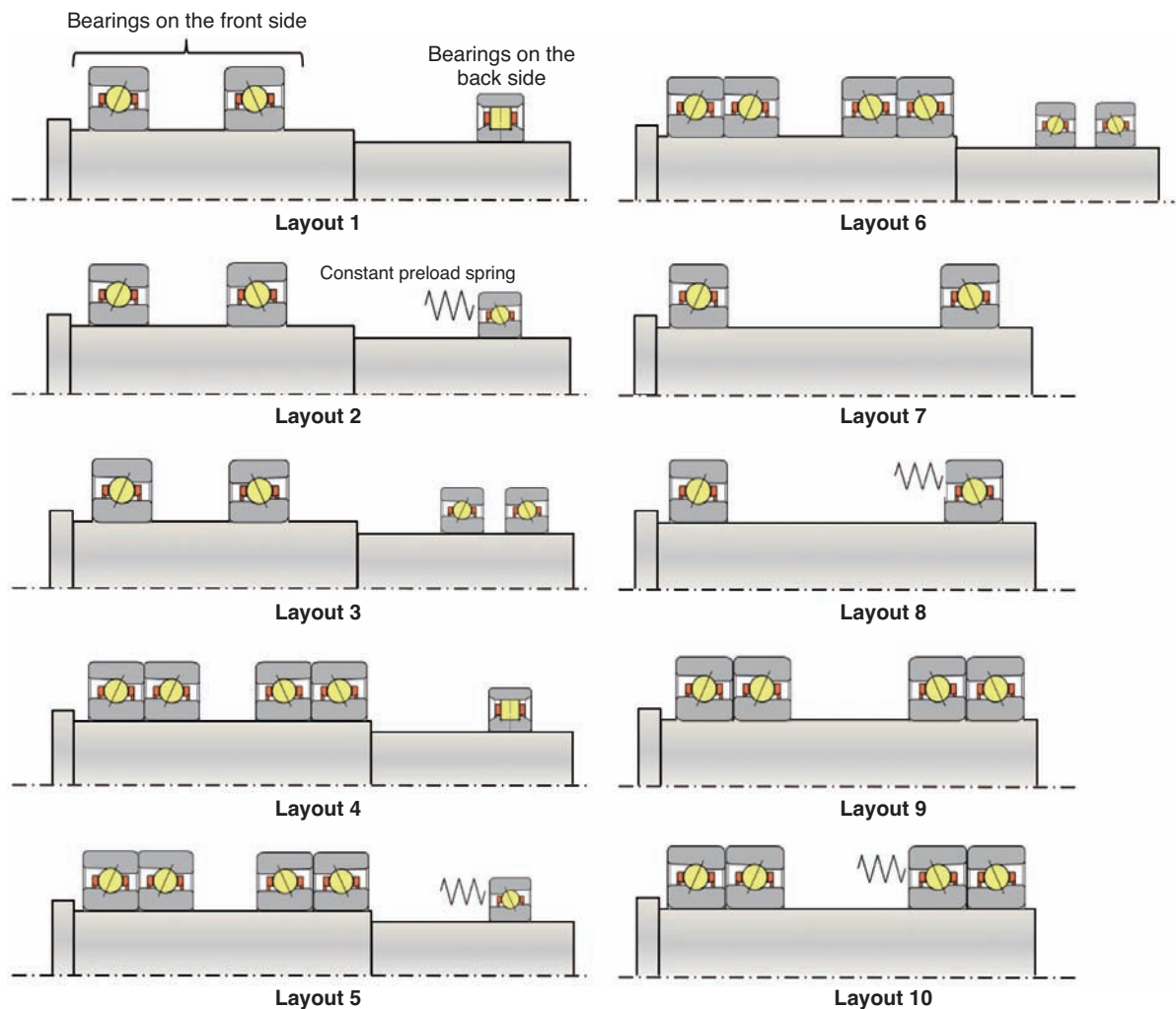


Fig. 2 Spindle layout

4.2 Input/Output screen examples

The customer selects layouts that need to be examined from the main spindle layout group shown in Fig. 2 and enters the required information into the shaded cells of the dedicated Excel® file shown in Fig. 3. The file has a function to check the entered items; therefore, the customer can easily check if any entered information is missing or wrong.

After entry of the required information, the customer sends the file to NTN's dedicated server by email.

The server which receives this email automatically calculates based on the input information and enters the calculation results, such as the main spindle rigidity,

to the output screen of the file in Fig. 4, and automatically sends the file to the customer.

The customer can receive the calculation results approx. 10 minutes after sending email to the server.

5. Calculation examples

As a part of the output examples shown in Fig. 4, the calculation results of main spindle axial rigidity when bearings, arrangements and preload methods in Fig. 5 are examined against the main spindle layout 1 of Fig. 2 are shown in Fig. 6.

The time needed to narrow down design candidates

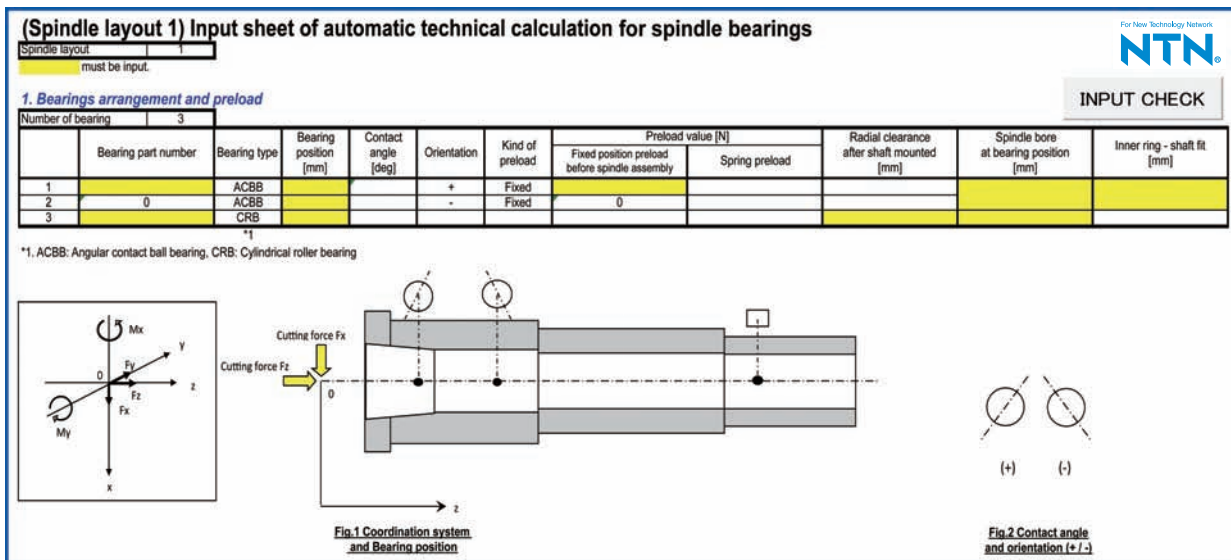


Fig. 3 Example of input sheet (Spindle layout 1, extract)

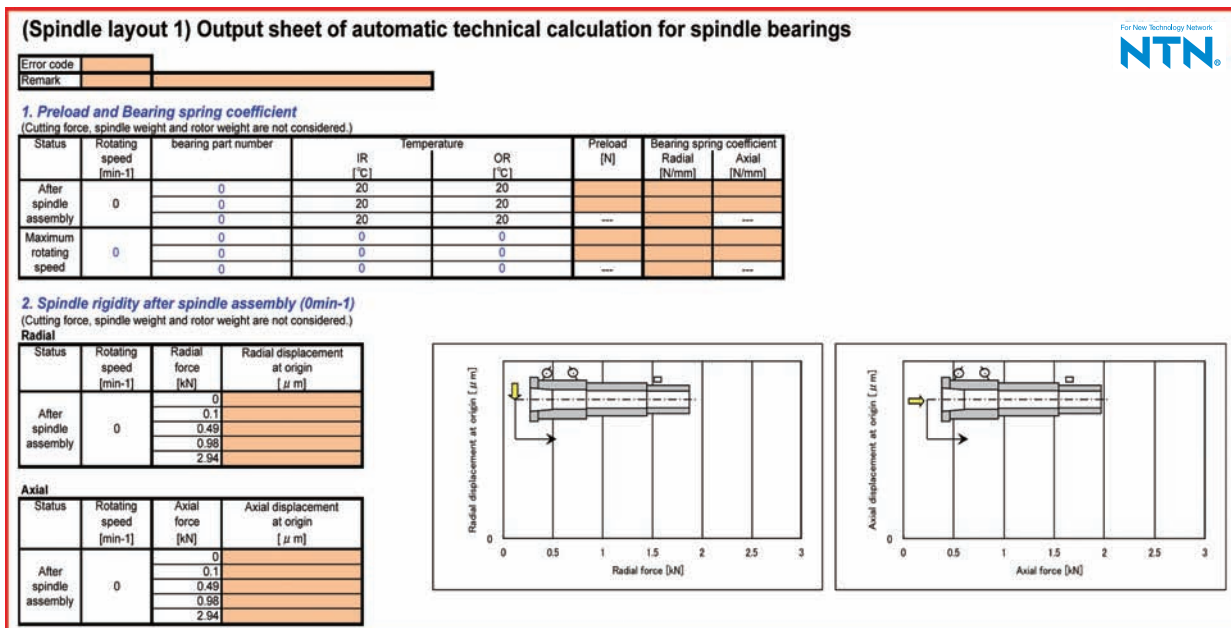


Fig. 4 Example of output sheet (Spindle layout 1, extract)

	Front side	Rear side
Bearing	High speed angular ball contact bearings 5S-2LA-HSE020	Cylinder rolling bearings N1018HSK
Arrangement	Two-row back-to-back (DB)	—
Preload method	Fixed position (GL preload)	—

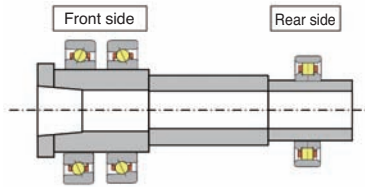


Fig. 5 Technical study example of spindle layout 1

	Front side	Rear side
Bearing	High speed angular ball contact bearings 5S-2LA-HSE020	Cylinder rolling bearings N1018HSK
Arrangement	Four-row back-to-back (DTBT)	—
Preload method	Fixed position (GL preload)	—

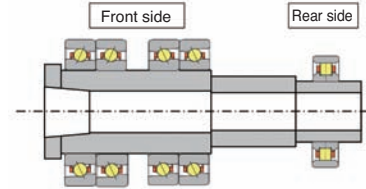


Fig. 7 Technical study example of spindle layout 4

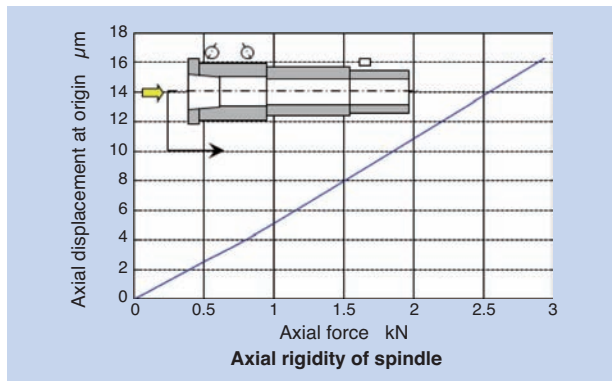


Fig. 6 Example of calculation result (Axial rigidity of spindle layout 1)

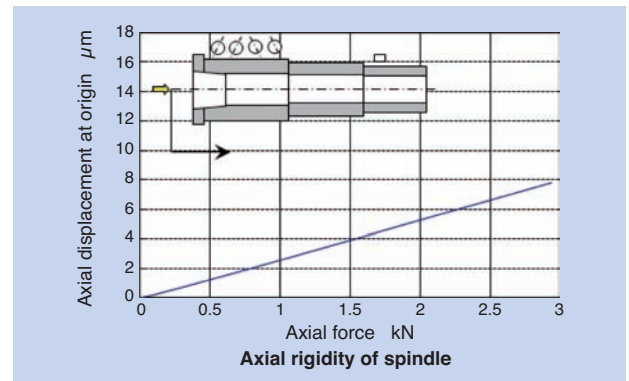


Fig. 8 Example of calculation result (Axial rigidity of spindle layout 4)

can be reduced, given that the calculation of properties of multiple main spindle design candidates can be performed quickly. and compared

For example, the rigidity can be quickly compared when double-row back-to-back (DB) bearings are applied to the main spindle of shaft diameter 100 mm on the front side shown in Fig. 5 and four-row back-to-back (DTBT) bearings in Fig. 7 are applied (main spindle layout 4). In this case, it is observed that the four-row back-to-back bearings shown in Fig. 8 have higher rigidity than the two-row back-to-back bearings shown in Fig. 6.

6. Conclusion

NTN developed the Bearing Technical Calculation System for Machine Tool Spindles which can automatically calculate properties of bearings and main spindles in a short time, for precision rolling bearings to be used for the main spindles of machine tools. This system will support diverse product development of machine tool manufacturers and spindle manufacturers.

With this system, NTN is poised to provide faster technical service and obtain higher customer satisfaction, as well as to contribute to reduced lead time for machine tool development.

NTN will explore easy-to-use, useful, and user friendly systems by the further improvement of this system.

Photo of authors



Keiichi UEDA
Machining Tool/Aerospace Engineering Dept., Industrial Machinery Division



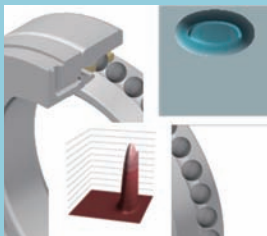
Yushi ONDA
Machining Tool/Aerospace Engineering Dept., Industrial Machinery Division



Shouhei HASHIZUME
Machining Tool/Aerospace Engineering Dept., Industrial Machinery Division

Estimation Method for Friction Torque of Air-oil Lubricated Angular Contact Ball Bearings

Hiroki FUJIWARA*



Angular contact ball bearings for high-speed spindles are lubricated by air-oil lubrication. A main factor of bearing friction torque is rolling viscous resistance. On the air-oil lubricated bearings, oil starvation leads to decrease in the rolling viscous resistance. In this article, the expression of deduction factor of rolling viscous resistance under the driving condition is proposed. It is derived by comparing between rolling viscous resistances estimated from measured friction torques of angular contact ball bearings under the air-oil lubrication and calculated

rolling viscous resistances under the full lubrication. The friction torque of the bearing is computed with consideration for differential slip, spin, elastic hysteresis loss, cage guiding friction, and the starved rolling viscous resistance. The starved rolling viscous resistance is obtained for product of the deduction factor and the rolling viscous resistance by the NTN original regression formula under the full lubrication.

1. Introduction

High speed spindles are required to contain heat in order to reduce thermal expansion of the main spindle. Air-oil lubrication has been adopted to reduce torque of the bearings, therefore reducing heat generation. Air-oil lubrication enables accurate control of lubricating oil quantity by adjusting the plunger pump to supply the minimum required lubricating oil directly to the raceway surface by suspending the oil in air. Through this operation, stirring resistance of the lubricating oil can be almost eliminated and the lubricating oil quantity between the rolling element and raceway is reduced to the bare minimum.

Lubricating oil above a specific amount at the inlet of the elastohydro dynamic lubrication (hereafter, EHL) contact between the rolling element and raceway presents sufficient lubrication where the thickness of the lubricating oil film does not increase anymore. However, from the viewpoint of damage control, sufficient lubrication is not necessarily required. Only oil film large enough to separate the two surfaces from contact is required. Since the rolling viscous resistance, which is the main element of friction torque, is affected by the lubricating oil quantity at the EHL contact inlet, the rolling viscous resistance can be reduced by actively creating insufficient oil quantity, called "starvation", to the level of having no oil film between the rolling element and raceway breaks.

The friction torque of rolling bearings using oil-bath lubrication can be calculated by considering differential slip, spin, rolling viscous resistance, shear resistance of the oil film between the rolling element and cage pocket, etc. ¹⁾.

However, this calculation method is applicable only to the case where lubricating oil is abundant and cannot be applied to air-oil lubrication as its friction torque is 1/10 to 1/5 that of bearings with sufficient lubrication. There are no reports that examine the estimation of friction torque for air-oil lubrication. Although there are attempts to theoretically estimate the starvation status of the ball pushing through the lubricating oil on the raceway, given certain assumptions of lubricating oil quantity ^{2), 3)}, it is difficult to accurately find the lubricating oil quantity on the raceway in air-oil lubrication. Therefore their application to practical use is challenging.

In this paper, we propose an estimation method for friction torque of air-oil lubricated angular contact ball bearings in their unique starvation status. The friction torque of these bearings consists of differential slip, spin, rolling viscous resistance, elastic hysteresis loss and friction between the cage guiding surface and the rolling element.

We considered that the lubricating oil film of these bearings produced a level of no mixed boundary lubrication, assumed that the friction torques due to differential slip and spin are not affected by the

*Advanced Technology R&D Center

starvation, and applied an experimentally obtained reduction factor to the rolling viscous resistance. This reduction factor is proposed as an equation experimentally identified comparing the experimental value of the friction torque with the calculated value of sufficient lubrication.

2. Symbols

a	: Long axial radius of contact ellipse
a_0	: Standard value on the long axial radius of contact ellipse
C	: Reduction factor constant of rolling viscous resistance (includes standard values of the parameters)
C'	: Reduction factor constant of rolling viscous resistance
d_p	: Pitch circle diameter of a ball
F_I	: Traction generated inside differential slip
F_{II}	: Traction generated outside differential slip
F_{HD}	: Dimensionless rolling viscous resistance
F_r	: Rolling viscous resistance
F_s	: Traction
G	: Dowson's dimensionless material parameter
k	: Ellipticity of contact ellipse
l_I	: Length of the contact point and pure rolling point in the radius direction inside the differential slip
l_{II}	: Length of the contact point and pure rolling point in the radius direction outside the differential slip
M	: Moment around rotational axis on the ball
M_r	: Friction torque of the bearing due to friction between the ball and raceway in the rolling direction
m	: Moment due to F_I and F_{II}
P_b	: Component force of the oil film reaction force on the ball in the rolling direction
P_e	: Component force of the oil film reaction force in the rolling direction in the equivalent system
P_1	: Component force of the oil film reaction force applied on object 1 (ball) in the rolling direction
P_2	: Component force of the oil film reaction force applied on object 2 (raceway) in the rolling direction
r_1	: Radius of object 1 (ball)
r_2	: Radius of object 2 (raceway)
r_b	: Radius of the ball
r_b'	: Distance from the center of the ball to the pure rolling point
r_e	: Equivalent radius
S_I	: Inside area of differential slip of inner ring contact
S_{II}	: Outside area of differential slip of inner ring contact
s	: Slip ratio
s_m	: Slip ratio to give the maximum coefficient of traction
s_T	: Index on the ball pass cycle
s_ν	: Index on the kinematic viscosity of lubricating oil
s_α	: Index on the long axial radius of contact ellipse
s_ω	: Index on angular velocity
T	: Pass cycle of the ball

T_0	: Standard value on the ball pass cycle
U	: Dowson's dimensionless parameter on velocity
W	: Dowson's dimensionless parameter on the point contact load
α_0	: Viscosity-pressure factor of lubricating oil
α	: Contact angle
β	: Inclination of the ball's axis of rotation
δ	: Distance from the pure rolling point to the contact point
μ_t	: Coefficient of traction
μ_{tmax}	: Maximum coefficient of traction
ν	: Kinematic viscosity of lubricating oil
ν_0	: Standard value on the kinematic viscosity of lubricating oil
τ	: Shear stress due to Couette flow of contact area between the ball and raceway ring
ϕ_r	: Reduction factor of rolling viscous resistance
ϕ_{re}	: Reduction factor of rolling viscous resistance (experimental value)
ω	: Angular velocity
ω_0	: Standard value on angular velocity
ω_b	: Rotational angle of the ball

Subscripts

i	: Inner ring
o	: Outer ring

3. Static analysis of angular contact ball bearings with only preload

High speed spindle angular contact ball bearings are typically arranged with 2-rows or 4-rows on the front side and used with fixed position or constant pressure preload. Although minor radial load may be applied during operation depending on the use of spindles, we ignored the effect of the radial load and assumed pure axial load with only preload applied to discuss the motion of a ball. Regarding the static analysis of angular contact ball bearings, Fujii has provided a detailed review⁴⁾ and Fujii has determined rotational axis of the ball based on Jones' control ring theory⁵⁾. With Jones' theory, the ball only rolls on the raceway of the ring which has larger friction and only spin occurs on the other raceway. However, in actuality, the rotational axis of the ball should be determined by the way that the force and moment are balanced and the consumed energy is minimized. In the following sections, we will discuss hydrostatic movement of the ball considering additional force due to slippage.

3.1 The force and moment produced due to slippage between the ball and raceway

Fig. 1 shows the schematic diagram of an axial cross section of one ball and the inner/outer ring indicating the force due to slippage within the contact ellipse.

When a tangential force is applied to the ball as shown in Fig. 1, the force can be obtained with the following equation:

$$F_{s,i} = \int \tau_i dS_{II} - \int \tau_i dS_I \dots\dots\dots (3.1)$$

$$F_{s,o} = \int \tau_o dS_{II} - \int \tau_o dS_I$$

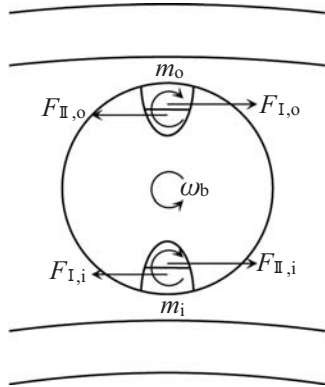


Fig. 1 Direction of forces and moments from slip

The moment of the ball around the pure rolling point due to slippage can be calculated with the following equation:

$$m_i = \int \tau_i l_I dS_I + \int \tau_i l_{II} dS_{II} \dots\dots\dots (3.2)$$

$$m_o = \int \tau_o l_I dS_I + \int \tau_o l_{II} dS_{II}$$

The moment of the ball around its rotational axis due to slippage can be expressed as follows:

$$M_i = \int (r'_b + \delta) \tau_i dS = r_b F_{s,i} - m_i \dots\dots\dots (3.3)$$

$$M_o = \int (r'_b + \delta) \tau_o dS = r_b F_{s,o} - m_o$$

The moment of the ball around the pure rolling point due to slippage can be calculated with the following equation:

$$m_i = \int \tau_i l_I dS_I + \int \tau_i l_{II} dS_{II} \dots\dots\dots (3.2)$$

$$m_o = \int \tau_o l_I dS_I + \int \tau_o l_{II} dS_{II}$$

The moment of the ball around its rotational axis due to slippage can be expressed as follows:

$$M_i = \int (r'_b + \delta) \tau_i dS = r_b F_{s,i} - m_i \dots\dots\dots (3.3)$$

$$M_o = \int (r'_b + \delta) \tau_o dS = r_b F_{s,o} - m_o$$

From Fig. 2, the peripheral force equilibrium on the ball is:

$$F_{s,i} - F_{r,i} + P_{b,i} - F_{s,o} + F_{r,o} - P_{b,o} = 0 \dots\dots\dots (3.4)$$

and as Zhou-Hoeprich⁶⁾ states, the rolling viscous resistance has the following relation:

$$P_e r_e = P_1 r_1 = P_2 r_2 = 2F_r r_e \dots\dots\dots (3.5)$$

Therefore, it can be rewritten as follows:

$$F_{s,i} - F_{r,i} + 2 \frac{r_{e,i}}{r_b} F_{r,i} - F_{s,o} + F_{r,o} - 2 \frac{r_{e,o}}{r_b} F_{r,o} = 0 \dots\dots (3.6)$$

The equilibrium of the moment around the rotational axis of the ball can be expressed,

$$r_b \cos(a_i - \beta) (-F_{r,i} + F_{s,i}) + r_b \cos(a_o - \beta) (-F_{r,o} + F_{s,o}) - m_i \cos(a_i - \beta) - m_o \cos(a_o - \beta) = 0 \dots\dots\dots (3.7)$$

and from equation (3.3), it can be rewritten as follows:

$$r_b \cos(a_i - \beta) (-F_{r,i}) + r_b \cos(a_o - \beta) (-F_{r,o}) + M_i \cos(a_i - \beta) + M_o \cos(a_o - \beta) = 0 \dots\dots\dots (3.8)$$

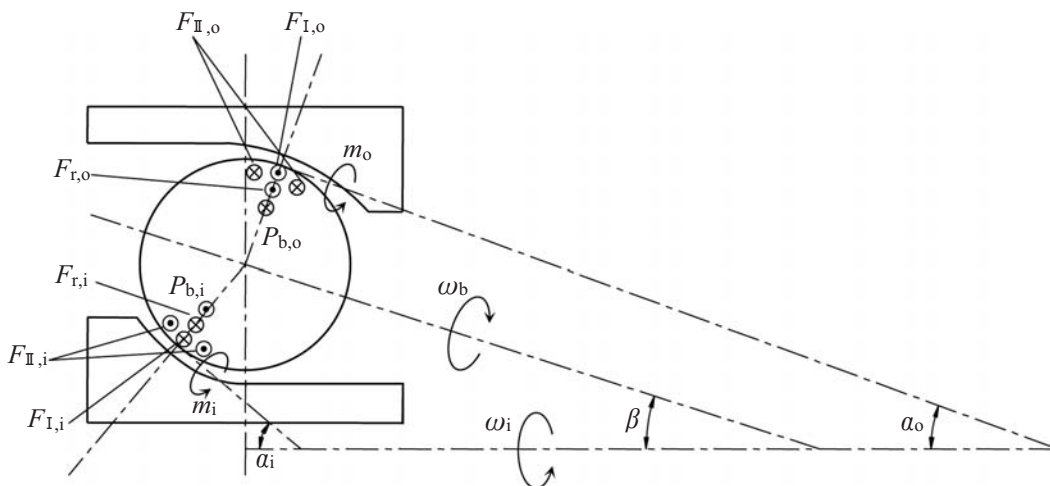


Fig. 2 Forces and moments on a ball

The moment applied to the outer ring of Fig. 3 can be expressed by Equation (3.9):

$$\begin{aligned}
 M_r &= \left(\frac{d_p}{2} + r_b \cos \alpha_o \right) (F_{r,o} + F_{s,o}) - m_o \cos \alpha_o \\
 &= \left(\frac{d_p}{2} + r_b \cos \alpha_o \right) F_{r,o} + \frac{d_p}{2} F_{s,o} + M_o \cos \alpha_o \dots\dots\dots (3.9)
 \end{aligned}$$

This is the friction torque of the bearings generated by the contact between the ball and raceway.

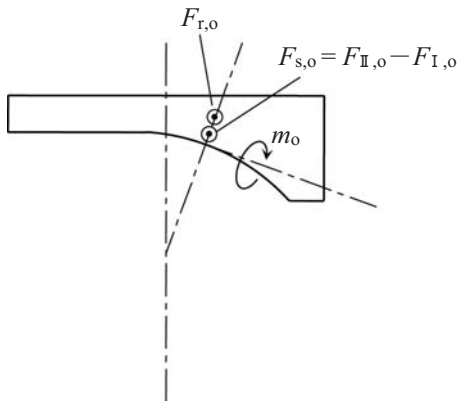


Fig. 3 Forces and moment on the outer race used to calculate outer ring friction torque

The rotational speed, orbital speed and the inclination of the rotational axis of the ball are determined so that the force and moment of the ball are balanced and the friction torque is minimized.

By determining the behavior of the ball in a certain state, the slip distribution and rolling viscous resistance can be calculated. The tangent force is the contact pressure at the observation point multiplied by the coefficient of traction. The coefficient of traction can be given as the function of slip ratio.

We adopted Lee-Hamrock's circular model⁷⁾ shown in Equation (3.10).

$$\mu_t = \frac{s/s_m}{\sqrt{1 + (s/s_m)^2}} = \mu_{t \max} \dots\dots\dots (3.10)$$

In this model, the maximum coefficient of traction $\mu_{t \max}$ and the slip ratio s_m must be assumed so we have set $\mu_{t \max}=0.05$ and $s_m=0.003$.

The rolling viscous resistance is calculated considering the starvation effect which is discussed in detail in the next section. The numerical calculation considers the forces due to this slip and rolling viscous resistance for a convergent calculation.

4. Starvation effect to rolling viscous resistance

4.1 Theoretical regression of rolling viscous resistance

The main undertaking of EHL is to study oil film thickness. Hamrock-Dowson⁸⁾, Chittenden et al.⁹⁾ and others are proposing many theoretical regression equations. On the other hand, only a few reports exist on rolling viscous resistance, and with regard to line contact, no equations based on EHL theory are found except for Zhou-Hoeprich's equation⁶⁾. Also, with regard to point contact, few reports exist on equations to easily obtain rolling viscous resistance. The equation proposed by Houpert¹⁰⁾ lacks material parameter and no consideration was given to a viscosity-pressure factor. It is natural to think that the rolling viscous resistance is affected by the viscosity-pressure and therefore we do not adopt Houpert's equation in this paper.

Fujiwara is proposing the theoretical regression equation regarding point-contact rolling viscous resistance by defining dimensionless rolling viscous resistance with Equation (4.1), and summarizing it as Equation (4.2) using a point-contact dimensionless number of Dowson, etc.¹¹⁾.

$$F_{HD} = \frac{F_r \alpha_o}{r_c^2} \dots\dots\dots (4.1)$$

$$F_{HD} = 44.6 U^{0.694} G^{0.961} W^{0.401} \{1 - 0.962 \exp(-0.818k)\} \dots\dots\dots (4.2)$$

We used the equation for rolling viscous resistance under sufficient lubrication to obtain the rolling viscous resistance under air oil lubrication by multiplying a reduction factor to account for the lubricant starvation.

4.2 Reduction factor of rolling viscous resistance

When a ball passes on the raceway, lubricating oil on the raceway is pushed away by the ball but moves back to the center of the raceway before the next ball passes, thus the lubricating oil quantity at the EHL oil film inlet is recovered. It is considered that the recovery quantity of lubricating oil is affected mainly by the ball passage cycle T , kinematic viscosity ν , and long axial radius of contact ellipse a . The longer the passage cycle of ball T , the larger the recovery amount. The smaller the kinematic viscosity ν , the greater the recovery amount because lubricating oil can move more easily. The smaller the contact ellipse long axial radius of the ball, the greater the recovery amount because the distance the lubricating oil has to move is shorter. It is also possible that centrifugal force on the lubricating oil may also affect the recovery amount. With a large centrifugal force, lubricating oil moves outward on the raceway and therefore the recovery amount is reduced on the contact area on the inner ring side.

However, the recovery amount is increased on the outer ring side because the lubricating oil is forced to move toward the center of the raceway. Since it is not possible to separate the torque produced at the inner ring and outer ring by the experiment, the impact of the reduction of torque at the inner ring side offset by the increase of torque at the outer ring side is considered using angular velocity ω . Although lubricating oil quantity affects starvation, in the case air oil lubrication, the impact was determined to be relatively small as a result of the experiment shown in Fig. 4, so we ignore will it in this discussion.

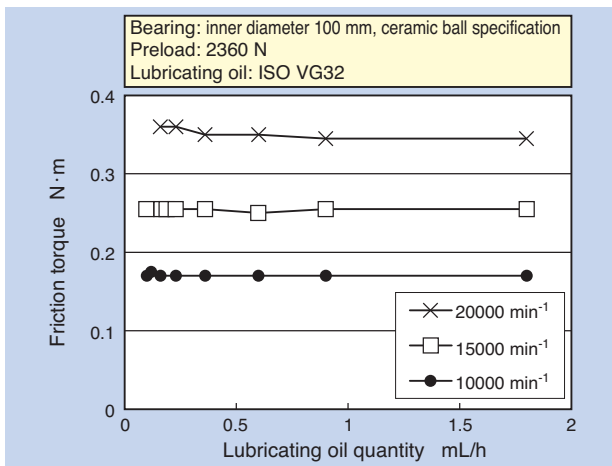


Fig. 4 Effect of oil quantity on friction torque

The reduction factor of the rolling viscous resistance is a function of the amount of lubricating oil recovered and therefore can be considered to be as a function of the ball passage cycle T , kinematic viscosity ν and long axial radius of contact ellipse a . The reduction factor for the rolling viscous resistance can have a value between 0 and 1 and it is adequate to consider that each parameter has a standard value when determining the starvation factor 1. Therefore, we define the reduction factor of the rolling viscous resistance in the following equation:

$$\phi_r = C \cdot \frac{T^{S_T}}{T_0} \frac{\nu^{S_\nu}}{\nu_0} \frac{a^{S_a}}{a_0} \frac{\omega^{S_\omega}}{\omega_0} \dots \dots \dots (4.3)$$

Where, when $T > T_0$, $T = T_0$
 when $\nu > \nu_0$, $\nu = \nu_0$
 when $a > a_0$, $a = a_0$
 when $\omega > \omega_0$, $\omega = \omega_0$

However, since it is difficult to obtain the standard values of T_0 , ν_0 , a_0 and ω_0 , by experiments, Equation (4.3) is converted to Equation (4.4) to identify C , S_T , S_ν , S_a , S_ω .

$$\phi_r = \frac{C'}{T_0^{S_T} \nu_0^{S_\nu} a_0^{S_a} \omega_0^{S_\omega}} T^{S_T} \nu^{S_\nu} a^{S_a} \omega^{S_\omega} \dots \dots \dots (4.4)$$

$$= C T^{S_T} \nu^{S_\nu} a^{S_a} \omega^{S_\omega} \dots \dots \dots (4.4)$$

In addition to rolling viscous resistance, other factors to impact the friction of rolling bearings are differential slip, spin and elastic hysteresis loss. The behavior of the ball is determined by the balance between traction due to slip produced by various frictions and the resistance against those frictions. Therefore, resistance cannot be separated into these various factors. However, we consider that the sum of the friction torques given by each factor is the friction torque of the bearings. In this study, in order to identify the reduction factor of rolling viscous resistance, we compared the friction torque obtained from the experiment removing the calculated friction torques of differential slip, spin, elastic hysteresis loss and friction within the cage guiding surface, and the friction torque due to rolling viscous resistance obtained by calculation assuming sufficient lubrication. We defined the value of the rolling viscous resistance obtained from the experimental data divided by the calculated value of sufficient lubrication as the experimental reduction factor of rolling viscous resistance ϕ_{re} . We determine C , S_T , S_ν , S_a , S_ω of Equation (4.4) so that the square of the difference between ϕ_r and ϕ_{re} becomes the smallest. We can then obtain mathematically precise values if we conduct multiple linear regression. However, for the purpose of this report, due to the accuracy of the experiment and assumptions given, we do not have to define accurate values. Instead integers or similar values such as 0, $\pm 1/2$, ± 1 , ± 2 , ... can be selected for S_T , S_ν , S_a and S_ω . For C , it is sufficient to round to two significant figures on the average of ratios between ϕ_r and ϕ_{re} when $C=1$ is assumed.

Skipping the details of the data, we identified ϕ_r under the above considerations using experimental data of friction torque by varying the bearing size, ball material, speed of rotation, preload and lubricating oil viscosity, we could obtain the following equation:

$$\phi_r = 3.5 \times 10^{-11} \frac{T^{0.5}}{\nu a^2} \dots \dots \dots (4.5)$$

This matches with the physical perception that the longer ball passage cycle T makes larger ϕ_r because it allows longer time for recovery of lubricating oil, smaller kinematic viscosity ν makes larger ϕ_r because it allows lubricating oil to move quickly for recovery, and smaller contact ellipse long axial radius a makes larger ϕ_r because the distance lubricating oil needs to move for recovery is shorter. In addition, ω which we introduced to consider the impact of centrifugal force was negligible. Since the coefficient 3.5×10^{-11} includes T_0 , ν_0 and a_0 , it has a dimension of $[m^4/s^{1.5}]$.

5. Comparison of the calculated value and experimental value of friction torque considering starvation

We calculated the rolling viscous resistance using the reduction factor obtained in section 4.2 and obtained the friction torque of the rolling bearings considering impact of slip, etc. We compared this calculated value with the value from the experiment. Although the friction force of elastic hysteresis loss and friction within the cage guiding surface should also be included in the simultaneous equation, their impact is relatively small. So we obtained them individually, converted to the

friction torques, and added them to the final friction torque. We referred to Kakuta's analysis¹²⁾ for the calculation of elastic hysteresis loss and calculated the friction within the cage guiding surface as the boundary friction caused by the centrifugal force. The effect of the elastic hysteresis loss and the friction within the cage guiding surface is small. The friction torque produced between the ball and raceway ring accounts for 60 - 90% of the overall friction torque.

Fig. 5 shows the experimental and calculated values of friction torque for comparison. Fig. 5 (a) shows the results of angular contact ball bearings with an inner diameter of 70 mm, using ceramic balls, a standard

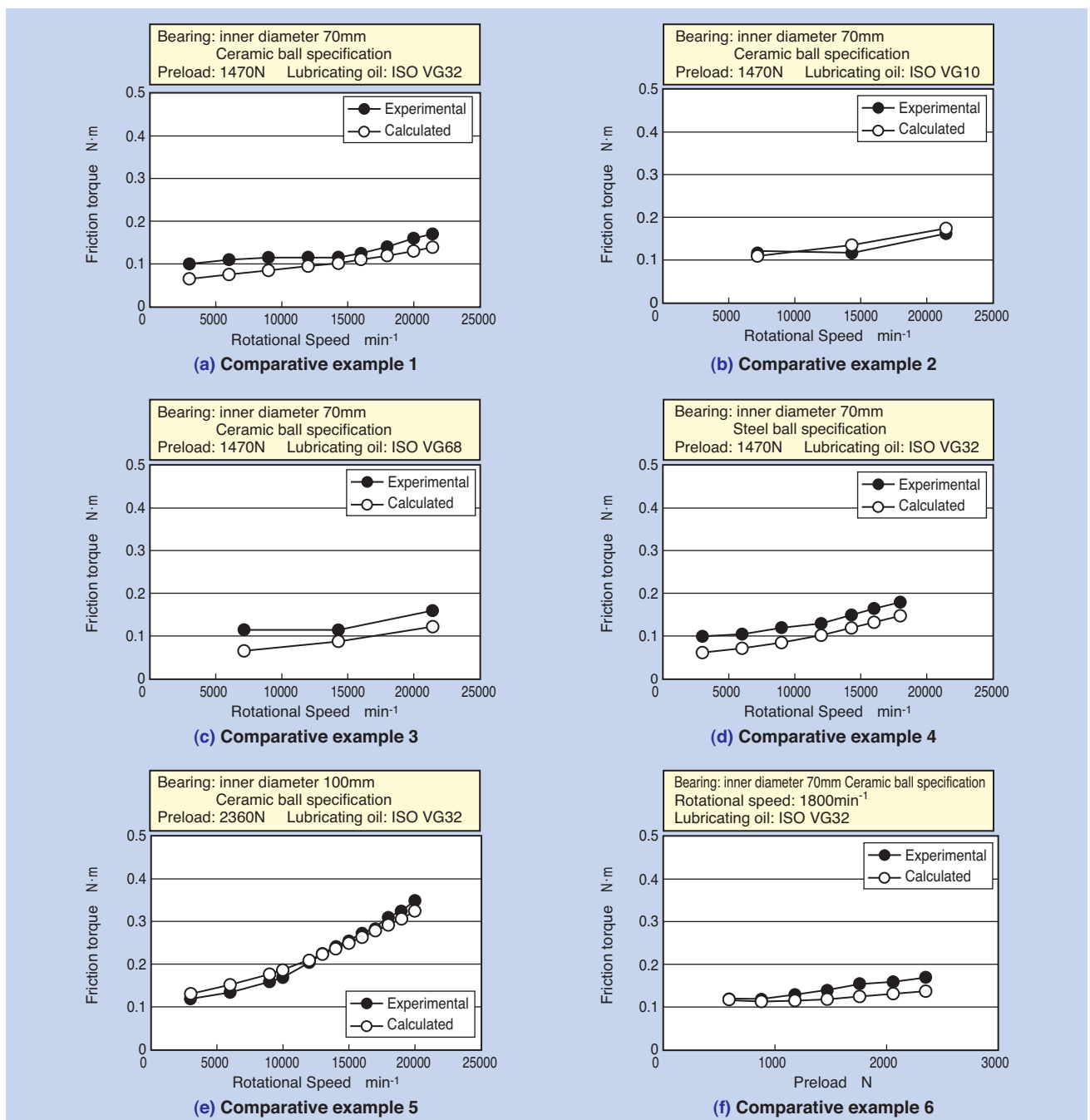


Fig. 5 Comparative example of experimental results to calculated values of friction torque

preload applied, and lubricated with ISOVG32 lubricating oil. The calculated values are a little smaller than the experimental values however they are roughly consistent. **Fig. 5 (b)** and **(c)** are the results with different kinematic viscosity of lubricating oil. **Fig. 5 (d)** shows the results with steel balls and **Fig. 5 (e)** is the result with a different bearing size. **Fig. 5 (f)** shows the comparison with a modified preload. In all cases, the calculated values duplicated the experimental values with accuracy sufficient for practical application.

6. Conclusion

We proposed an estimation method for friction torque of air-oil lubricated angular contact ball bearings. Since air-oil lubrication does not achieve a sufficient lubrication condition, we used experimental values for friction torque to identify the reduction factor of the rolling viscous resistance. This was done by comparing the rolling viscous resistance estimated from the experimental values of friction torque and the calculated values of rolling viscous resistance of sufficient lubrication. The friction torque of air-oil lubrication can be calculated by solving the equilibrium of forces and moments considering the rolling viscous resistance multiplied by the reduction factors, differential slip, traction produced by the spin, and adding the elastic hysteresis loss and friction within the cage.

This technology can be used not only for improving accuracy of the selection of high-speed bearings and preloads, but also for contributing to further development and improvement of high-speed bearing and spindle design.

References

- 1) Hiroki Fujiwara, Kenji Fujii: Rolling Bearing Torque in Oil Bath Lubrication, Japan Society for Precision Engineering Spring Conference Academic Lecture Proceedings (2002), 219.
- 2) Takashi Nogi: An Analysis of Starved EHL Point Contacts with Reflow, *Tribologist*, 59 (2014) 239-250.
- 3) Kenichi Shibasaki, Masato Taniguchi, Marie Oshima: Development of Numerical Method for Coupled Simulation of Starved EHL and Macro Flow, Proceedings of Japan Tribology Conference Tokyo (2010-5), 245-246
- 4) Kenji Fujii: Research on High-Speed Rolling Bearings, Meiji University, Doctoral Dissertation (2001).
- 5) A. B. Jones: A General Theory for Elastically Constrained Ball and Radial Roller Bearings under Arbitrary Load and Speed Conditions, *Trans. ASME J. Basic Eng.*, 82 (1960) 309-320.
- 6) R. S. Zhou and M. R. Hoeprich: Torque of Tapered Roller Bearings, *Trans. ASME, J. Tribol.*, 113 (1991) 590-597.
- 7) R. T. Lee and B. J. Hamrock: A Circular Non-Newtonian Fluid Model: Part I – Used in Elastohydrodynamic Lubrication, *Trans. ASME, J. Tribol.*, 112 (1990) 486-496.
- 8) B. J. Hamrock and D. Dowson: Isothermal Elastohydrodynamic Lubrication of Point Contacts, Part 2 - Ellipticity Parameter Results, *Trans. ASME, J. Lub. Tech.*, 98 (1976) 375-383.
- 9) R. J. Chittenden, D. Dowson, J. F. Dunn and C. M. Taylor: A Theoretical Analysis of the Isothermal Elastohydrodynamic Lubrication of Concentrated Contacts II. General Case, with Lubricant Entrainment along Either Principal Axis of the Hertzian Contact Ellipse or at Some Intermediate Angle, *Proc. R. Soc. Lond., A* 397 (1985) 271-294.
- 10) L. Houpert: Piezoviscous-Rigid Rolling and Sliding Traction Forces, Application: The Rolling Element-Cage Pocket Contact, *Trans. ASME, J. Tribol.*, 109 (1987) 363-371.
- 11) Hiroki Fujiwara: Rolling Viscous Resistance of Point Contact EHL, Proceedings of Japan Tribology Conference Tokyo (2009-5), 119-120.
- 12) Kazuo Kakuta: Friction Moment of Radial Ball Bearings under Thrust Load, *Transactions of the Japan Society of Mechanical Engineers* 27-178, 3 (1961) 945-956.

Photo of author



Hiroki FUJIWARA
Advanced Technology
R&D Center

Real-time Monitoring of the Superfinishing Process

Kohei HIGASHI*

Hajime ISA*

Takakazu KITAGAWA*

Takashi ONISHI**

Kazuhito OHASHI**



The advantage of superfinishing is that, the fine surface of workpiece can be obtained by the transition of machining states from cutting action to finishing one, while the condition of superfinishing stone surface changes self-sharpening to wear during one processing cycle. In conventional superfinishing process, to obtain the fine surface, the superfinishing stone, machining condition and timer control have been determined by empirical laws. In this study, we have monitored the machining force during machining process, and have judged the roughness of workpiece by calculating the machining force ratio.

1. Introduction

Rolling bearings (hereafter, bearings) are said to be the “central core” of the machine industry and to have supported the growth of Japan's manufacturing industry (such as automobile and machine tools) with high performance and consistent quality. Bearings are always required to provide high quality, low cost and short lead time as machine components for high-volume production. This is the reason for the designation “central core” and production technologies to achieve these requirements are also required.

A high level of performance is required for these bearings from three basic elements: low torque, low noise and long life. Superfinishing machining technology (hereafter, “superfinishing”), which is presented in this paper, is a very important machining process in bearing manufacturing, has a significant impact on these three elements of bearing performance.

Conventional superfinishing has typically involved selecting grinding stones and machine conditions based on experience and determining machining time based on desired accuracy. In addition, the machining requirements are affected by the accuracy of the prior process and the condition of the grinding stones.

In view of these issues, the authors developed a technology to monitor the superfinishing process in real-time^{1), 2)}. In this study the in-process monitoring technology was controlled to determine the finish accuracy over a preset threshold, focusing on the machining force ratio, which is the ratio of the thrust and principal forces applied to the grinding stone. In addition, the improvement over a conventional machining cycle based on fixed time was examined and is included in this report.

2. Characteristics of superfinishing and machining models

2.1 Characteristics of superfinishing

Superfinishing is a machining process in which a stick-shaped, fine-grained stone with a relatively low hardness is applied to a work piece under a certain pressure with oscillating motion, rotational motion and feed motion between the stone and the work piece and a large amount of processing solution is supplied³⁾.

Fig. 1 shows the transition cycles of the stone during superfinishing. An important characteristic of superfinishing involves the initial contact between the work piece and the stone and subsequent relative motion which creates new cutting edges. This action is

*Production Engineering R&D Center

**Graduate School of Natural Science and Technology, Okayama University, Division of Industrial Innovation Sciences

called self-dressing of the grinding stone.

Fig. 1 (a): The initial stage of the cycle is called the grinding state, where the stone removes the top rough surface of the work piece while the stone also self-dresses, smoothing the work piece.

Fig. 1 (b): The final stage of the cycle is called the polishing state, where self-dressing of the stone concludes and the stone becomes loaded and there is a rapid improvement in the roughness of the work piece.

Fig. 1 (c): A new work piece is introduced which causes rapid self-dressing of the grinding stone due to the roughness of the new work piece. This overall cycle repeats. Although required in normal grinding, the grinding stone is not dressing in the superfinishing process.

For machining accuracy, superfinishing produces a good non-directional surface roughness due to the smaller amplitude motion and lower machining force than ordinary cutting or grinding. In addition, since superfinishing generates less heat during machining, it minimizes the affected work layer. As a result this process ensures the machined raceway surface is acceptable for bearings with high wear resistance.

2.2 Superfinishing model

Fig. 2 shows a general model of the superfinishing process. Pressure is applied vertically to the grinding stone which oscillates perpendicularly to the rotation of the cylindrical work piece. When focusing on the machining action of the grinding stone, it moves in a sinusoidal motion on the surface of the work piece. The maximum velocity vector on the below sinusoidal curve is called "grinding directional angle θ " and is expressed by Equation (1). θ is an important indicator of superfinishing processing conditions which is commonly used.

- a : Grind stone oscillation amplitude (mm)
- f : Grind stone oscillation frequency (c/min)
- D : Work piece diameter (mm)
- N : Work piece rotational speed (min^{-1})

$$\theta = \tan^{-1}(af/DN) \dots\dots\dots (1)$$

In theory, a stronger grinding action results from a larger θ and a stronger polishing action results from a smaller θ .

However, in reality, since there are countless grains on the grinding stone, a smooth and quality finish can be obtained.

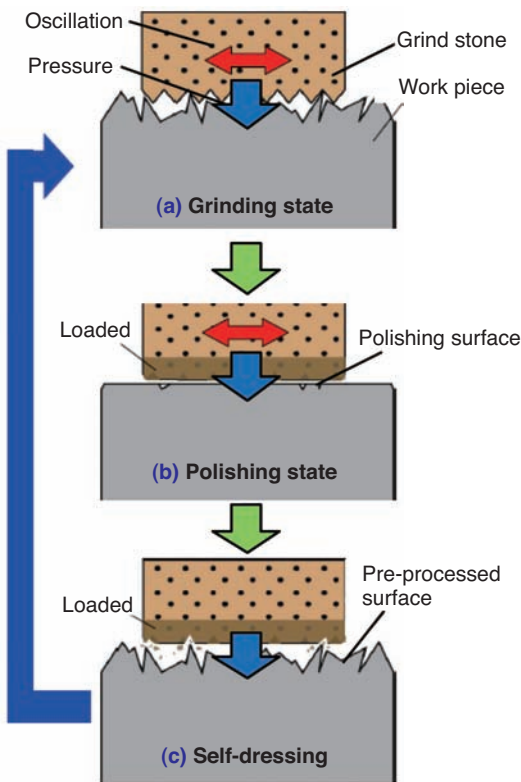


Fig. 1 Mechanism of superfinishing cycle

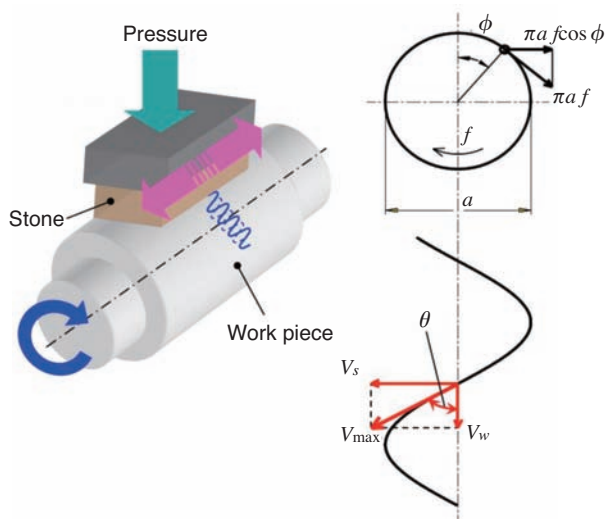


Fig. 2 Superfinishing model

2.3 A superfinishing example

The raceway, in contact with the bearing rolling elements (balls, rollers, etc.), is required to have good surface roughness and quality surface properties, particularly with no surface protrusions, to minimize noise.

As an example, Fig. 3 shows a comparison of the inner ring raceway surfaces of a deep-groove ball bearing after grinding and after superfinishing (part number 6203 with envelope dimensions of: ID = 17 mm, OD = 40 mm & width = 12 mm). An after grinding surface roughness of R_a 0.3 was improved to R_a 0.03 after superfinishing with good surface properties close and no significant protrusions.

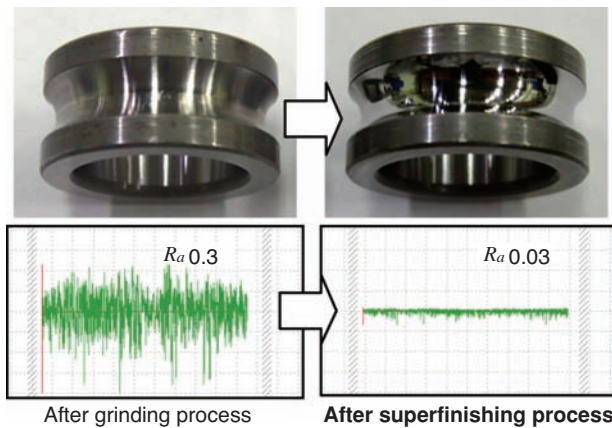


Fig. 3 Improvement of surface roughness

3. Experimental setup

Fig. 4 shows the experimental apparatus used for this study. In order to model the setup shown in Fig. 2, a cylindrical stepped round bar was selected as the work piece. The work piece is supported on both sides and rotated by the lathe shaft. The grinding stone is held by a fixture and pushed horizontally against the work piece by an air cylinder in a direction perpendicular to the work piece. The grinding stone, holding fixture and air cylinder are attached to a table which oscillates axially with respect to the work piece.

Table 1 lists the sensing devices used in this study to monitor the machining process and the items that were evaluated. They include a sizing sensor to measure the work piece diameter, a laser displacement sensor to measure the movement of the grinding stone table as an indication of the stone wear, and a three-component force sensor, installed between the stone and the air cylinder, to measure the machining force applied to the stone. In this study, these sensors were used to determine the finish accuracy by monitoring the machining force applied to the grinding stone.

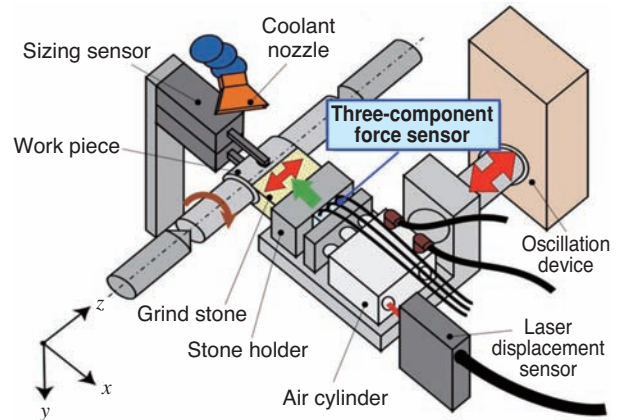


Fig. 4 Experimental setup

Table 1 Sensing device and evaluation points

Sensing device	Displacement	Evaluation item
(1) Sizing sensor	Dimension change	Stock removal
(2) Laser displacement sensor	Advancement of grind stone table	Wear of stone
(3) Three-component force sensor	Grinding resistance against grind wheel	Thrust force Principal force Force on the oscillating direction

4. Investigation of superfinishing machining characteristics

4.1 Test conditions

To understand the machining characteristics of superfinishing and to estimate the formation process of the finished surface, an experiment was conducted under the test conditions shown in Table 2.

The test used a grinding stone wheel (WA1200) with a thickness of 5 mm and the work piece was made from bearing steel pre-processed to a cylindrical shape with a surface roughness of R_a 0.3 – 0.4. In addition, water-insoluble grinding fluid was used as the coolant. The grinding directional angle θ selected was 3.2° and based on experience is positioned between grinding and polishing processing, allowing for continuous transitions from the grinding state to the polishing state. The machining time was set at 20 seconds max. and allowed an arbitrary 2 – 20 seconds to find the machining state during the process.

Table 2 Experiment condition in one step

Grinding stone	Spec : WA1200 20A Size : t5xW30 mm
Work piece	SUJ2 ϕ 20 (HV770)
Grinding stone oscillating amplitude	0.75mm
Cooling flow	2.0L/min (Water-insoluble)
Grinding stone oscillating frequency	1870 c/min
Shaft rotational speed	1230 min ⁻¹
Grinding direction angle	3.2°
Pressure on grinding stone	0. 54 MPa
Machining time	2~20s

4.2 Test results

Fig. 5 shows a diagram of the sensing devices in the machining area including forces and distances. Fig. 6 shows the monitoring data over 20 seconds of machining under the test conditions defined in Table 2 with the elapsed time on the horizontal axis. The top figure shows a plot of the advancement of the grind stone stand d and stock removal R . The bottom figure shows the plot of the thrust force P and principal force Q applied to the grinding stone.

The movement of dimension d barely changes after 3 seconds from the beginning of machining. Therefore, it is theorized that the grinding stone became loaded and the machining state transitioned to polishing. Looking at the change in the machining force, the thrust force P is constant at 80 N as the pressure to the stone is constant; however, we could verify that the principal force Q gradually decreases after 3 seconds.

Focusing on this change, the machining force ratio P/Q (hereafter “force ratio”) was added to the plot. It was observed that after a brief decrease, the force ratio gradually increased over time. This trend is theorized to be related to the roughness of the finishing surface.

4.3 Formation process of a finished surface

In order to understand the roughness formation process on a finished surface, the relationship between force ratio and roughness was examined. Experiments were conducted under 7 different conditions with machining times of 2 – 20 seconds under the test conditions shown in Table 2. As a result, the relationship between the machining force ratio (after machining is completed) and the roughness of the finished surface was determined. The results from each experiment are shown in Fig. 7. As the machining time increased, the machining force ratio increased while the roughness of the finished surface reduced. By calculating the correlation coefficient between the force ratio and the surface roughness at 7 points, a very high correlation of -0.97 was obtained. Therefore, it is highly probable that roughness of the finished surface can be determined by monitoring the machining force ratio.

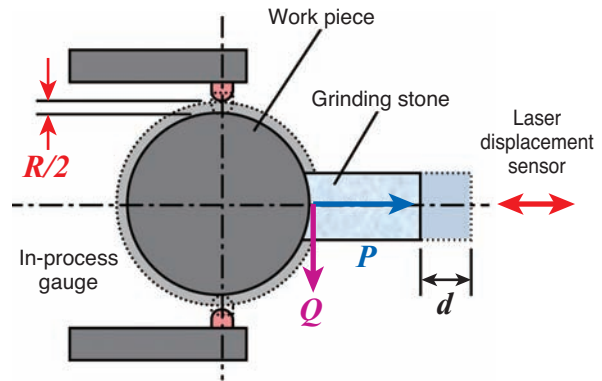


Fig. 5 Diagram of sensing devices in machining area

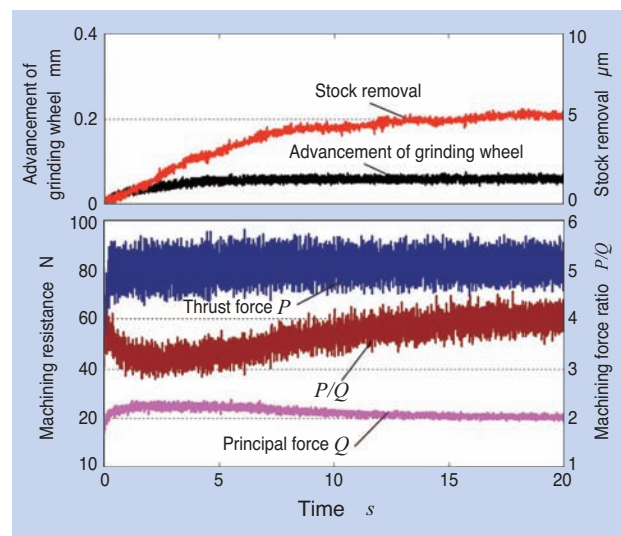


Fig. 6 Machining characteristics during one stage processing

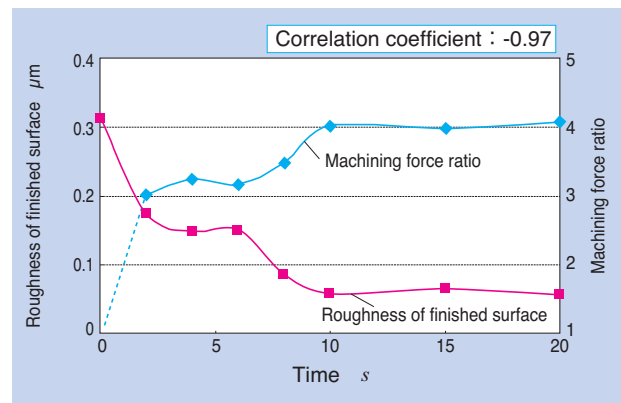


Fig. 7 Relationship between machining force ratio and surface roughness

5. Machining characteristics under forced state transition

5.1 Test conditions

When using the superfinishing process during normal production, it is necessary to remove the work piece's preprocess surface (stock removal) and achieve final finish accuracy. To meet these requirements, it is common to program machining conditions for both grinding and polishing and have the cycle changed sequentially by the timer. That way stock removal is ensured and the stone is forced to be loaded for polishing.

Therefore, the conditions were set for the test machine grinding and polishing processes in two stages and the machining characteristics were investigated.

Table 3 shows the experimental conditions. The grinding stone, coolant and work piece were equivalent to those shown in **Table 2** and the wheel swing speed was set to 670 min^{-1} for both grinding and polishing. The grinding directional angle was changed by reducing the stone oscillation frequency from 1,870 c/min (cycles per minute) for grinding to 500 c/min for polishing to constitute the forced transition condition from grinding to polishing. The machining time for both grinding and polishing each lasted 10 seconds.

Table 3 Test conditions in two steps

Stone	Spec : WA1200 20A	
	Size : t5xW30 mm	
Work piece	SUJ2 ϕ 20mm (HV770)	
Stone oscillating amplitude	0.75mm	
Coolant flow	2. 0L/min (Water-insoluble)	
Machining condition	Grinding (1st step)	Polishing (2nd step)
Stone oscillating frequency	1870 c/min	500 c/min
Main shaft rotational speed	670 min^{-1}	670 min^{-1}
Grinding direction angle	6.0°	1.6°
Stone pressure	0.54 MPa	0.54 MPa
Machining time	10s	10s

5.2 Test results

Fig. 8 shows the monitoring data from the machining test conditions listed in **Table 3**. For the first 10 seconds, the large machining directional angle is set to the grinding state. During this time, the grinding wheel and stock removal are both progressing at a constant speed and the machining force of the grinding stone and the machining force ratio (P/Q or force ratio) are constant. After 10 seconds, when the grinding directional angle is reduced to transition into the polishing state, both stone advancement and stock removal cease and the force ratio starts to increase. At

the end of the machining cycle (20 seconds total), the force ratio was slightly below 4 and the roughness of the finishing surface (R_a) was 0.052.

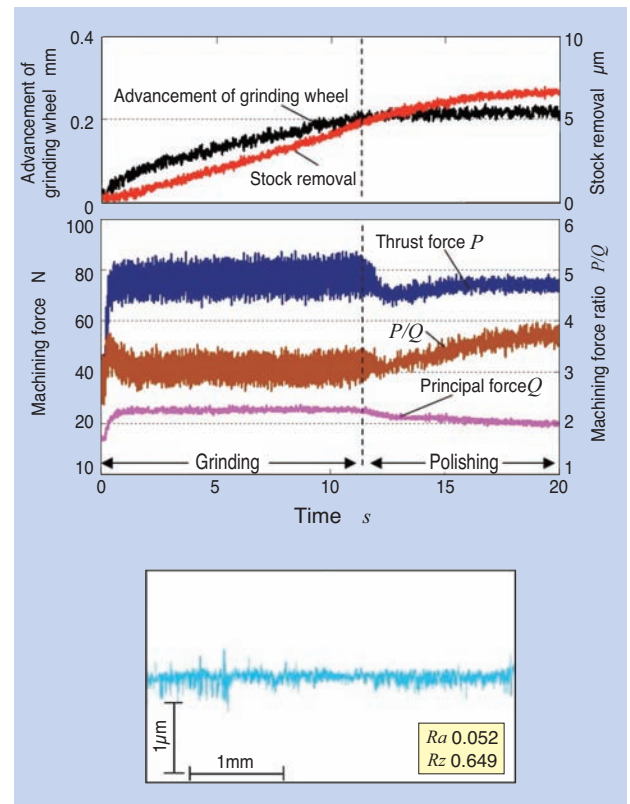


Fig. 8 Machining characteristics during two stage processing

6. Determination of finishing accuracy via threshold

6.1 Method for determining threshold

A high correlation between the machining force ratio P/Q (force ratio) and the finish accuracy (roughness) was verified by the results shown in **Fig. 6** and **7**. Therefore, to estimate the finish accuracy (roughness) in real-time during the machining process, the force ratio was monitored during the machining process and it was compared to a threshold. **Fig. 9** shows a diagram of the signal processing system. The output signals from the three component force sensor are transferred to the processing unit after the A/D conversion. The processing unit has an output terminal which sends the signal to the air cylinder which in turn applies pressure to the stone.

Fig. 10 shows the flowchart used for roughness determination. The two-step machining conditions that were used are listed in **Table 3**. At the beginning of the machining process, the part is ground for 10 seconds for pre-process stock removal. Next, after switching to polishing conditions, the force ratio is continuously

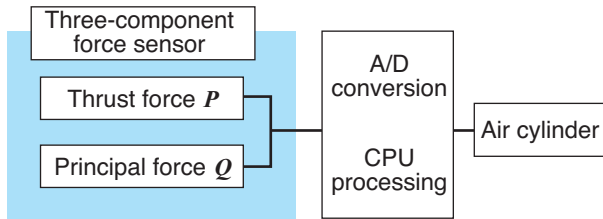


Fig. 9 Signal processing system

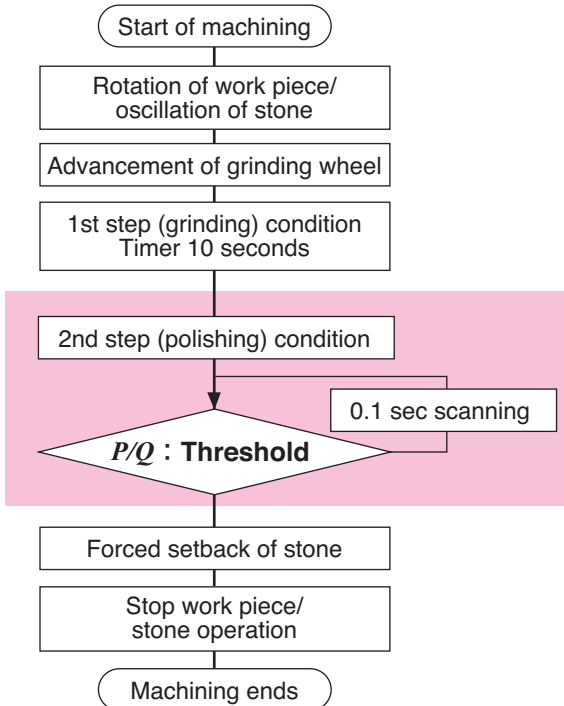


Fig. 10 Judgement signal flow chart

calculated and the result is compared to a predetermined threshold at regular intervals. The scan period was set to a 0.1 second interval. When the force ratio becomes larger than the predetermined threshold, the finishing process is deemed complete and a signal is sent to the air cylinder to retract the grinding wheel away from the work piece.

6.2 Threshold determination results

The plots in Fig. 11 show the measurement results of P , Q and P/Q when the thresholds are set to 3.4 and 3.7, respectively, as well as the surface roughness before and after the machining process. When the threshold was set to 3.4, P/Q exceeded 3.4 after 5 seconds of the polishing cycle. Roughness of the finished surface (R_a) was 0.064 but small irregularities such as grinding marks were found along the roughness curve. When the threshold was set to 3.7, P/Q exceeded 3.7 after 17 seconds of the polishing cycle. However, this time the roughness of the finished surface was 0.037 and no grinding marks were observed along the roughness curve. Based on these results, it was verified that setting a higher threshold for P/Q results in a longer polishing time for improved roughness of the finished surface and no grinding marks.

6.3 Relationship between the force ratio (P/Q) and surface roughness

In order to obtain a straightforward relationship between the force ratio (P/Q) threshold and roughness, roughness and polishing time were plotted against P/Q

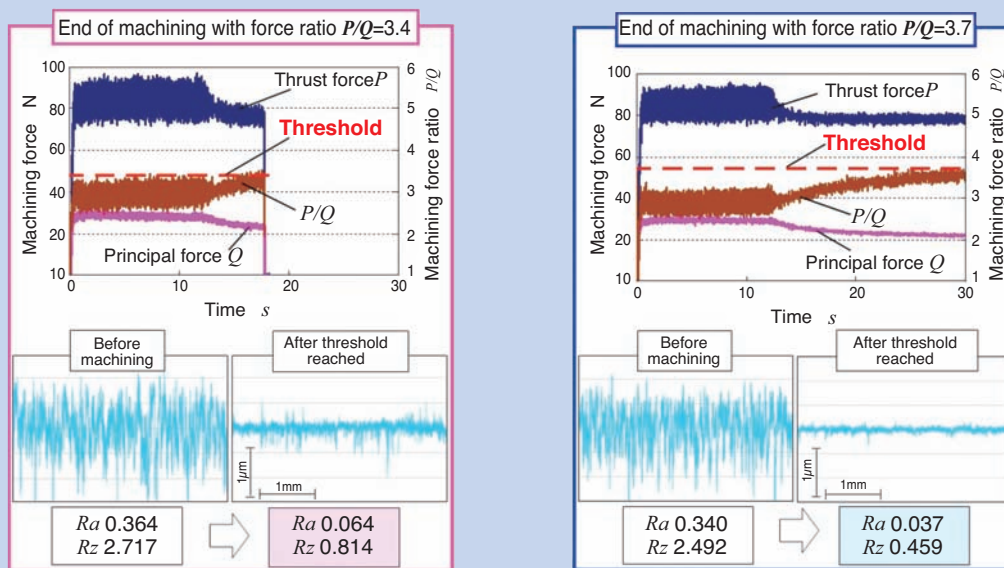


Fig. 11 Comparison of surface roughness after processing using threshold force ratio

thresholds set at 0.1 intervals (shown in Fig. 12). As the threshold is increased, the polishing time lengthens and roughness improves.

However, when the threshold exceeds 3.7, there is no significant improvement in roughness even though the machining time continues to increase.

To compare the superiority of this targeted machining process with a conventional method using fixed machining time, additional testing was performed. In order to obtain a roughness (R_a) of 0.052 (indicated by the red dotted line in Fig. 12), which is equivalent to the finishing surface roughness of the conventional method (as shown in Fig. 2), a threshold of 3.6 was set for this test. The time required for the polishing step was 6 seconds, which is a 40% reduction from the 10 seconds used by the conventional machining method.

From the above results, it is possible to control the roughness of the finishing surface by monitoring the machining force ratio and governing the process using the force threshold. As a result the productivity can be improved by reducing the polishing time compared to a conventional cycle which machines parts for a fixed amount of time.

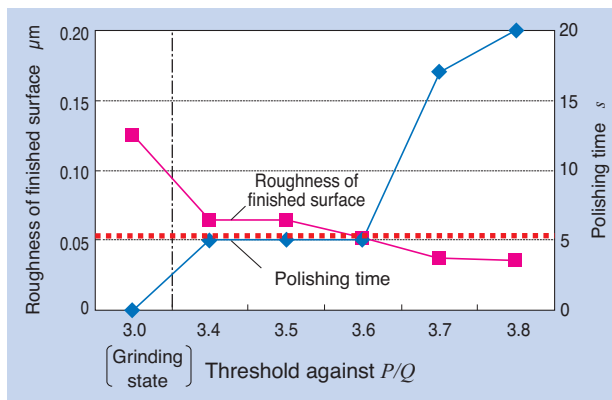


Fig. 12 Relationship between finished surface roughness and polishing time at different threshold force ratios

7. Conclusions

Technology was created to monitor the superfinishing process via an in-process gauge and the following results were obtained:

- (1) A method was proposed to automatically determine the finish accuracy by in-process monitoring of machining force ratio, thus monitoring the machining state in the superfinishing process.
- (2) Under polishing conditions, the machining force ratio P/Q , which is calculated from the thrust force P and the principal force Q applied to the stone, was found to increase as the machined surface roughness became lower.
- (3) The machining cycle time can be reduced by ending the machining process as soon as the machining force ratio P/Q exceeds a preset threshold. This is compared to the conventional machining method of setting machining conditions of all parts for the same amount of time.

References

- 1) Takahiro Iguchi, Taskashi Onishi, Kazuhito Ohashi, Kohei Higashi, Shinya Tsukamoto: Development of Monitoring Technology for Superfinishing Process, The Japan Society for Abrasive Technology, Proceedings of Abrasive Technology Conference (2011) 297.
- 2) Shingo Yamashita, Takashi Onishi, Kazuhito Ohashi, Kohei Higashi, Takahiro Iguchi, Ryosuke Yamamoto, Shinya Tsukamoto: In-Process Monitoring of Machining State in Superfinishing – Determination of Machining State by Machining force ratio -, The Japan Society for Abrasive Technology, Proceedings of Abrasive Technology Conference (2012) 45.
- 3) Toshikatsu Nakajima, Norihiko Narutaki: Kikai Kakogaku (1984) 195.
- 4) T. Onishi, K. Ohashi, K. Higashi, S. Yamashita, T. Iguchi and S. Tsukamoto, In-Process Monitoring of Machining State in Superfinishing, Proceeding of the 7th International Conference on Leading Edge Manufacturing in 21st Century (LEM21), (2013) 89-92.

Photo of authors (titles are at the time of release)



Kohei HIGASHI
Production Engineering
R&D Center



Hajime ISA
Production Engineering
R&D Center



Takakazu KITAGAWA
Production Engineering
R&D Center



Takashi ONISHI
Graduate School of Natural
Science and Technology,
Okayama University, Division of
Industrial Innovation Sciences



Kazuhito OHASHI
Graduate School of Natural
Science and Technology,
Okayama University, Division of
Industrial Innovation Sciences

Lightweight Bearing for Robot

Sebastien BRISSON*



Robotic arms do have many qualities, but intelligence is not their best point. It is necessary and important to be programmed move by move. They work in a XYZ coordinates world associated to θ_x θ_y θ_z for rotations. Moreover, programming and maintenance are matter for specialists. Their size and potential tremendous force imply large secured areas and heavy procedures when an incident occurs.

Some trends can be found such as Cobotics that have new technologies of motion control and can coexist with surrounding humans.

Based on its know-how, experience and Market understanding, NTN-SNR prototyped a bearing concept that aims to accompany the Robotics Megatrends. Making the bearing lighter, less expensive by tuning its stiffness according to real needs of coming technologies.

1. Introduction

Many characteristics are required for industrial robotic arms; however, the following two points are particularly important:

- Robot arm design must conform to the demand for several sizes and use in a broad range of applications while also considering the cost of the robot arm.
- Higher functionality of robot arms and improved operability

To satisfy these requirements, particularly from a functionality standpoint, robot arms use technology to determine various conditions in addition to high rigidity, broad operational range and easy operation. Therefore, bearings supporting the robot arms are required to be designed to conform to these technology trends.

In this paper, we briefly discuss industrial robots and present the lightweight bearings for robots developed by NTN-SNR.

2. Structure and capability of robots

The basic functionalities of today's industrial robots have evolved first from positioning, then to grabbing objects with "hands" to more detailed tasks such as assembling, welding, painting, etc. which previously was the work of humans. For example, in the assembly

process, when parts are conveyed by robots, the robots have to grab the parts in the same way and transport them to the predefined locations following the same trajectory every time. Therefore, the positioning of the robot and objects must always be accurate. This is true with welding and painting processes as well, so accurate positioning and stable operation is again required.

Fig. 1 shows a typical perpendicular articulated 6-axis robot for industrial use. The programming for operation is achieved by expressing and modeling the accurate motion of the robots in X, Y, Z and θ_x , θ_y , θ_z axes, as shown in **Fig. 2**, for each process to be accomplished.

Therefore, good performance of today's industrial robot arms is determined by the following items:

- Accuracy of positioning
- Accuracy of positioning reproducibility
- Rigidity

With the performance of these items, motions are combined to establish automatic operation of an industrial robot. In addition, sufficient rigidity to support the payload capacity of the robot is required.

Fig. 3 shows the performance required for the current industrial robots. Today bearings for industrial robots are heavy due to the necessary control of axis, high precision, high rotational speed (acceleration) and high rigidity required.

*NTN-SNR ROULEMENT Industry Innovative Developments

Fig. 4 shows an image of the industrial robot line-up. In general, the maximum payload capacity is approx. 1,500 kg, however, the majority of applications are 20 kg or less. High rigidity is required not only for maintaining accuracy of positioning, as mentioned earlier, but also for supporting the weight of the manipulator.

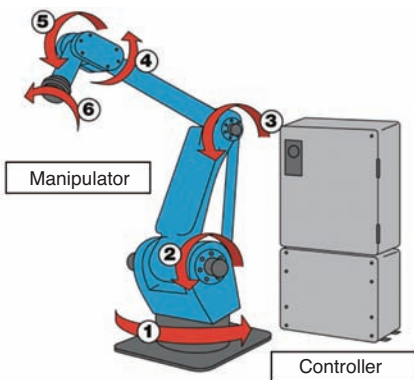


Fig. 1 6 axis robot (manipulator and controller)

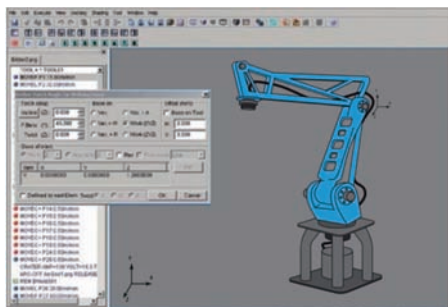


Fig. 2 Modelling and programing for motion

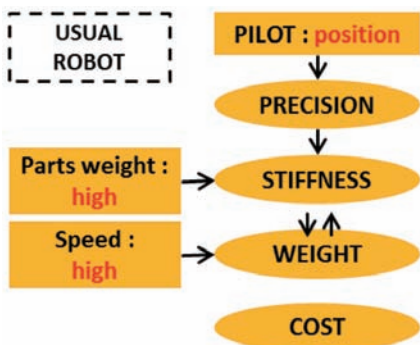


Fig. 3 Specification of usual robots

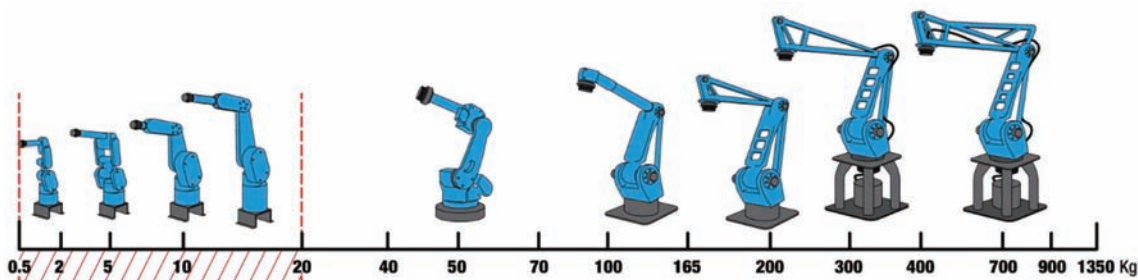


Fig. 4 Payload of industrial robots

3. Cobotics and new technology

3.1 Cobotics

Cobotics derived from "cobot", an abbreviation of collaborative robot, means a collaborative robot that operates in an environment surrounded by humans. Fig. 5 shows examples of operation. Cobots detect the co-working humans and other robots when they approach the cobots and work on their own without making contact with others. Cobots also work for automated or assisted driving of vehicles. For example, they can sense how humans work and assist them with their work or change their behavior accordingly.

The payload of cobots is usually 20 kg or less and these robots are becoming lighter and smaller. However, these approaches are being adopted by large units, as well.



Example of autonomous cobot



Example of cobot to follow man's movements while multiplying its strength

Fig. 5 Payload of industrial robots

The cobots are mainly deployed for tasks with less added value, time consuming tasks and repetitive tasks of critical process. Cobots are also aimed at reducing the load of workers and preventing injuries such as arthritis.

3.2 New technologies

Among the technologies on robots, the following are directly related to control:

- Image processing technology
- Force sensing technology
- Laser measurement technology

Fig. 6 shows some examples of movement using the above technologies. These technologies enable robots to understand the shape of the work, support it, and accurately transport it after computational processing for various movements.

They also assist operation with other robots and adjust distance with the workers in the proximity.

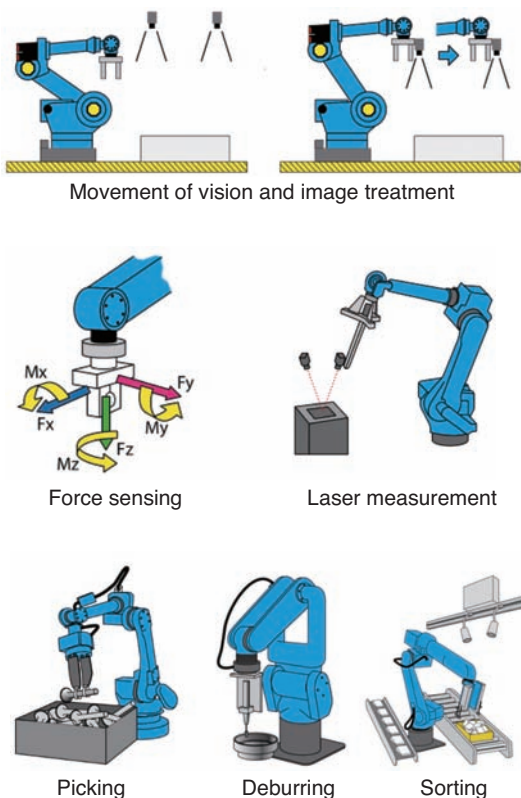


Fig. 6 Example of movement by new technologies

4. Bearings for robots developed by NTN-SNR

In Europe, NTN-SNR is a leading bearing manufacturer of reducers for robots and maintains a high share not only for industrial robots but also for work/motion-assist robots.

Fig. 7 shows an example of the specifications for the manipulator and bearings of common industrial robots. The rigidity required for the bottom most turning bearings and the wrist rotating bearings at the tip of the arm are significantly different even for the same robot. Therefore, the bearings to be used in the robot must be individually selected depending on the task, payload, position and operation of the robot.

Due to the above reason, crossed roller bearings shown in Fig. 8 or four-point contact ball bearings are used for turning, rotating and oscillating robot joints and the bottom most bearings need to support the weight of the manipulator.

NTN-SNR focused on developing a more lightweight bearing while maintaining the previously mentioned functional requirements.

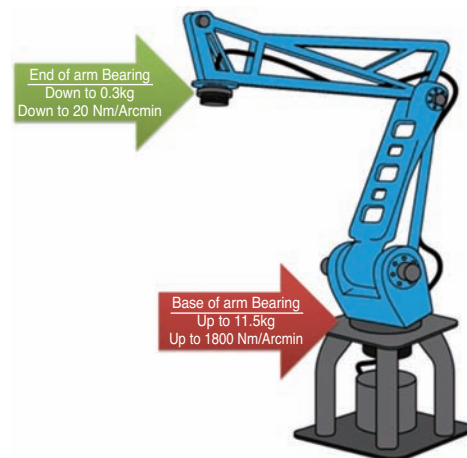


Fig. 7 Manipulator and specification example of bearing



Fig. 8 NTN-SNR crossed roller bearing

5. Lightweight bearings for robots

The design concept of NTN-SNR lightweight bearings for robots is a composite material of resin and steel. Conventionally, inner and outer rings are specially shaped and made of steel because they are attached to the peripheral components with bolts, etc., however, the developed product uses steel only for bearing raceway assembly and rolling elements and adopts resin for the specially shaped part to be attached to the peripheral components.

The application of resin must function without affecting the bearing peripheral components. Therefore, we also considered the operating environment of industrial robots in the selection of resin material and adopted nylon resin of high-melting point with excellent strength.

Also, the developed bearings can replace the conventional bearings without redesigning of robot joints and reducers.

In the following, we present the types of lightweight bearings for robots.

5.1 Non-separable type

With the non-separable type, resin is injection molded on the inner and outer rings of the deep groove ball bearings, as shown in Fig. 9. The rigidity is increased by reducing the internal clearance of the bearings.

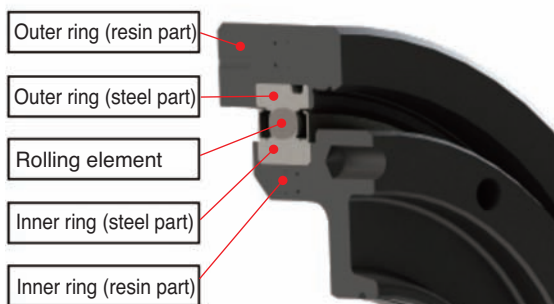


Fig. 9 Lightweight bearing for robot (non-separable type)

5.2 Separable type

The separable type is the crossed roller bearings shown in Fig. 10, to obtain higher rigidity than the non-separable type which adopted deep groove ball bearings. In the assembly of the bearings, only the inner ring is molded in a single piece with resin and the resin parts of the outer rings are assembled from both sides of the steel parts after the rollers are inserted.

Also, as shown in Fig. 11, the widths of the separable resin parts on each side are different. The reason is that the outer rings made of steel are engaged only to one

side of the resin parts, so that no displacement on the outer ring raceway of both sides is created in the radial direction.

There are several ways to connect both sides of the resin parts, such as use of rivets as shown in Fig. 12 ①, or to insert steel-made sleeves and fixed by bolts as shown in ②.

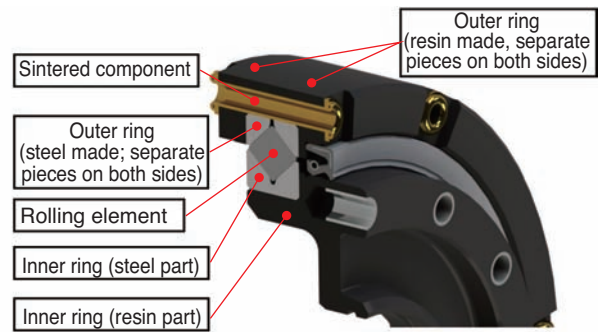


Fig. 10 Lightweight bearing for robot (separate type)

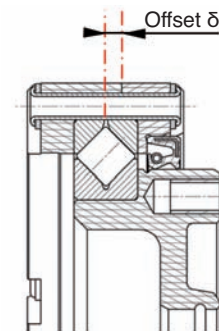


Fig. 11 Assemble example of lightweight bearing (separate type)

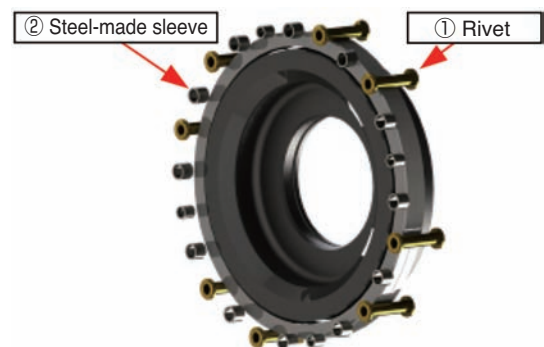


Fig. 12 Fastening example of lightweight bearing

5.3 Rigidity

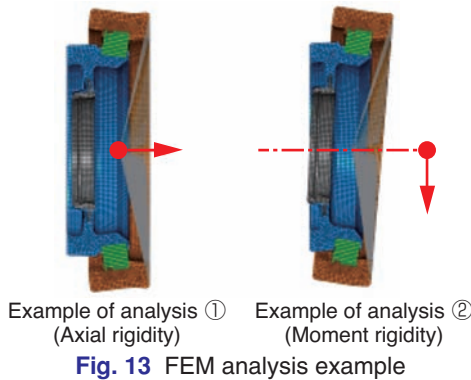
The developed bearings have reduced rigidity compared with the conventional bearings because the specially shaped part of the inner/outer rings is replaced with resin. Table 1 and Fig. 13 show an example of the comparison of rigidity of the separable type (crossed

roller bearings) by FEM analysis.

In case of cobotics discussed in Section 3, which are controlled by image processing and force sensors, the high speed and high rigidity requirements of current robots are not required; therefore, this reduction of rigidity of the developed product should be in the permissible range.

Table 1 FEM Analysis to compare the stiffness between developed bearing and current bearing

		Current bearings	Developed bearings
Bearing main sizes mm		$\phi 40 \times \phi 110 \times 26$	
Analysis conditions	① Axial load kN	40	
	② Moment load Nm	1000	
Analysis results	① Axial rigidity mm (axial movement)	0.020	0.150
	② Moment rigidity deg (bearing inclination angle)	0.04	0.25



5.4 Weight

Table 2 shows the comparison of weight between the conventional bearings made of steel and the developed product of the equivalent size. The developed bearings reduced the weight by 63% for the separable type and 73% for the non-separable type compared to the conventional bearings, resulting in a significant weight reduction.

Table 2 Weight comparison between developed bearing and current bearing

Bearing type	Current bearings (separate crossed roller)	Developed bearings (separate crossed roller)	Developed bearings (non-separate, deep groove ball)
Appearance			
Bearing size mm	$\phi 40 \times \phi 110 \times 29$		
Weight kg	1.00	0.37	0.27
Reduction factor %	—	63	73

6. Conclusion

We have discussed the lightweight bearings for robots developed by NTN-SNR. We have also summarized the recent trend and new technologies of the robot industry and the resulting requirements to the bearings in **Fig. 14**.

As shown in **Fig. 3**, the control of axis for the robot motion has been emphasized until now. However, it is believed that the requirements on being lightweight and lower in cost will be more emphasized more in the future instead of high speed and high rigidity, due to the increasing control with image processing and support of workers by cobotics.

We developed the bearings for robots discussed in this paper to cope with this trend. We will continue our development with a close eye on the trends of the robot industry and are poised to contribute to the development of the European and global industry by providing this product for various industrial robots.

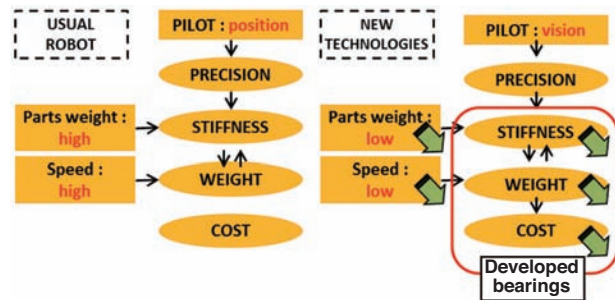


Photo of author



Sebastien BRISSON
NTN-SNR ROULEMENTS
Industry Innovative Developments

Essential Elements for Ecology

Condition Monitoring System (CMS) for Wind Power Generators Wind Doctor®

Data acquisition
module



Data management/monitor/
analysis software



NTN's Condition Monitoring System (CMS) for Wind Power Generators consists of a data acquisition module, measurement sensors, and data management/monitor/analysis software and enables monitoring of bearing condition, etc. from a remote location. It helps early detection of errors to prevent expansion of damages and ensures availability of power generators.
CMS: abbreviation of Condition Monitoring System

NTN®

www.ntn.co.jp

**NTN's system products supporting stable operation
of offshore wind power generation**

Development of Condition Monitoring System



Keisuke HASHIZUME*
Akitoshi TAKEUCHI*
Yuzuru TANAKA*

NTN has developed Condition Monitoring System using bearing diagnosis technology. This article introduces CMS's products, and explains necessity of CMS in the market and expansion in the future.

1. Introduction

Aiming at the prevention of global warming, energy conservation and the reduction of power generation cost, demonstration and full-scale production of power generation devices using renewable energy are well underway. In Japan, the feed-in tariff program for renewable energy (photovoltaic, wind, hydro, geothermal and biomass power) started in July 2012 and their deployment is expected to accelerate. Among these, the cost of wind power generation is low among renewable energies, and many sites are actually deployed as key power generation facilities in Europe, which is a leading region for wind power generation. It is expected that wind power generation will further expand as larger wind power generation facilities are developed for off-shore deployment, and large-scale introduction in the Asian region is expected as well.

NTN introduced the Condition Monitoring System (CMS) for wind power generation as a product for the renewable energy market that supports the next-generation power industry, taking advantage of vibration analysis technology and sensing technology. Through various improvements since its introduction, we now market this system as Wind Doctor® as shown in Fig. 1. We are increasing the number of installations



Fig. 1 Data acquisition module, Wind Doctor®

at wind turbine sites in Japan, and have started acquiring large amounts of data. In this paper, we discuss the reason why CMS is drawing attention, technical details of analysis through CMS, and its future technology trends.

2. Condition Monitoring System (CMS)

Condition Monitoring System is a system to continuously or intermittently acquire data remotely from several sensors, such as vibration sensors, displacement sensors and temperature sensors which are attached to the target machinery, for early detection of component anomalies based on the acquired data. By early detection of anomalies, damage progression can be limited, which results in reduced maintenance costs, and by determining the damaged area, appropriate preparation and treatment can be performed.

3. Market demands of CMS

Now, we will discuss the market demands of CMS, taking the power generation business as an example.

In order to reduce power generation costs, the reduction of initial facility investment, the introduction of highly efficient generation technologies and the improvement of equipment availability are necessary. That is, after switch-over, maintaining stable operation is critical, and downtime must be reduced to a minimum. In general, stable operation of power generation is considered to be a basic requirement, and unscheduled downtime has a significant impact on consumers.

As a countermeasure to avoid such downtime, periodical inspection of equipment and preventive

*CMS Engineering Dept., Industrial Machinery Division

maintenance are necessary, but it is also important to gather information beforehand in order to identify anomalies and their locations based on early and accurate detection of changes in equipment condition. In fact, with the gas turbine generation and steam power generation, various sensing technologies, such as vibration, temperature, rotation speed, pressure, displacement and acoustic response, are used for continuous monitoring and for associated maintenance operations.

On the other hand, in the field of industrial machines, some businesses, including those with long production lines such as steel, papermaking and chemical plants, are conducting preventive maintenance with immediate effect by introducing their own CMS with the objectives of maintaining supply capabilities and ensuring stable quality.

4. Examples of equipment and applications

NTN is moving forward with the development and market introduction of CMS related technology including special sensors. In this section, we describe some of the typical examples of NTN's commercial products.

4.1 CMS for wind power generation

The following is the data acquisition module, Wind Doctor® targeted for use in wind power generation applications as shown in Fig. 1 in the previous section.

This module works with a 100V-240VAC power supply and is equipped with 17 channels of signal inputs. It also complies with IP65 level of Japanese Industrial Standard for electrical machinery and apparatus protection code JIS C 0929 for its dust/water proof performance.

In order to achieve highly stable operation, it is also equipped with data protection and cooling capabilities during power outages as a hedge against risk. This Wind Doctor® module is operated as part of a system as shown in Fig. 2. The output data in multiple formats from various sensors are encrypted and uploaded to a

dedicated server through the Internet. Based on this acquired data, various analyses and precise diagnoses are done using dedicated software applications installed on the user PC. Fig. 3 shows the base screen of this condition monitoring. When an anomaly is detected, an alarm is displayed on the screen, and emergency emails are sent to the designated email addresses.

This software also displays the trend view of RMS values as shown in Fig. 4 and vibration wave patterns of acquired data as shown in Fig. 5. In addition, it also has capabilities of various calculations and analyses such as the envelope signal processing as shown in Fig. 6 based on vibration wave patterns as shown in Fig. 5 and FFT spectrum analysis and display as shown in Fig. 7. It also allows arbitrary setting of band-pass filters to maximize the signal-to-noise ratio (S/N ratio), which is appropriate for displaying defect frequencies of the bearings and step-up gears diagnosed as damaged.

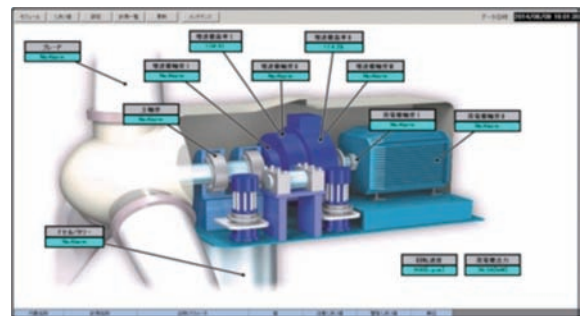


Fig. 3 Home screen of monitoring software

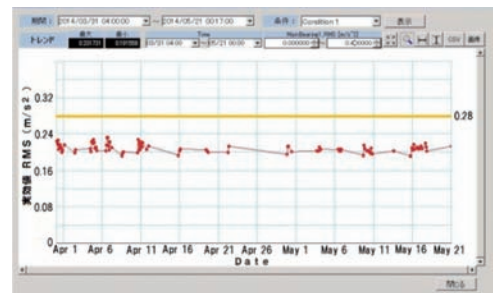


Fig. 4 Trend view of RMS value

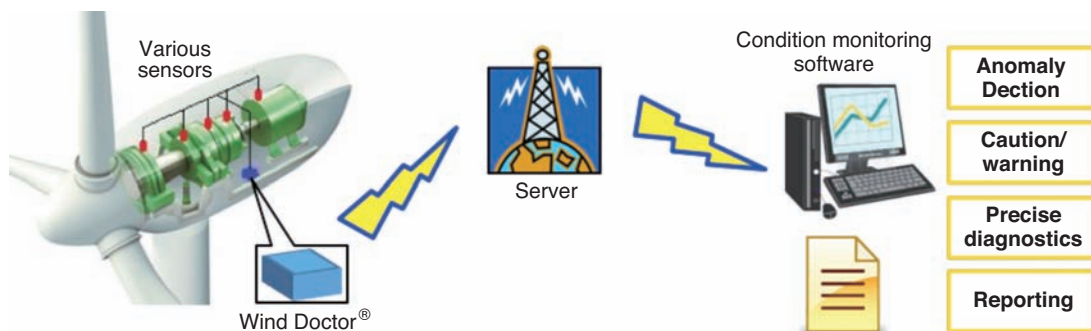


Fig. 2 Layout of CMS for wind turbines

In addition, the raw data can be downloaded in CSV format so that users can freely process the data.

These operations can be run repeatedly without limitation, so they can be used as an effective data analysis tool.

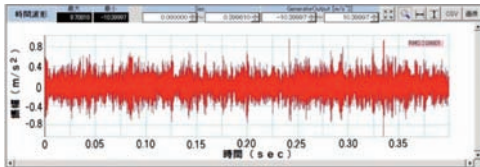


Fig. 5 Wave pattern of acquired data

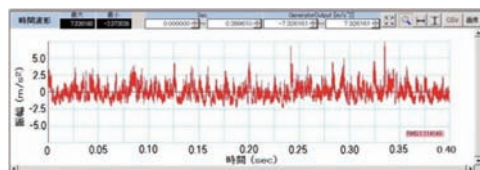


Fig. 6 Envelope signal processing of acquired data

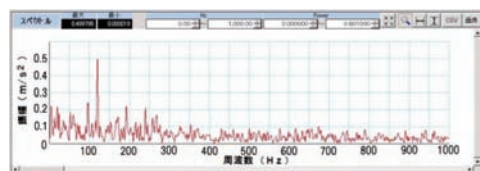


Fig. 7 FFT Analysis Results

4.2 Handy type failure detection device

Fig. 8 shows the handy type failure detection device developed for condition monitoring and maintenance of general industrial machines such as general-purpose motors and fans.

This system consists of a vibration pick-up and pocket-sized A/D converter that are provided by NTN and link to a user-provided smartphone. This product was realized by applying bearing diagnostics technology which has been developed over the years with the goals of performing diagnostics “easily”, “consistently”, “on the spot” and “in a short time”.

Conventional all-in-one type diagnostics systems calculate and analyze the measured vibration data within the system, and require large displays for easy identification of detailed data, limits how far their size and weight can be reduced. In contrast, by using smartphones, displayed data can be easily recognized by zooming in to the most detailed view.

In addition, maintenance personnel of manufacturing equipment and production lines need to carry the system together with tools and paperwork during their maintenance and inspection activities.

Therefore, NTN’s handy type failure detection device is made very compact and portable for the measurement of vibration. In this system, the acquired

vibration data is automatically sent to the server through the Internet using a dedicated application as shown in Fig. 9. The server determines normal/abnormal status of inner rings, outer rings and rolling elements of the bearings through calculation and analysis and sends the results back to the smartphone.

Fig. 10 shows an example of the operation screen and result display screen on the smartphone. Fig. 11 shows FFT analysis results, Fig. 12 shows the overall values and Fig. 13 shows a trend view of the RMS values. These data are stored on the dedicated server not only on a temporary basis, but also past data can



Fig. 8 Handy type failure detection device

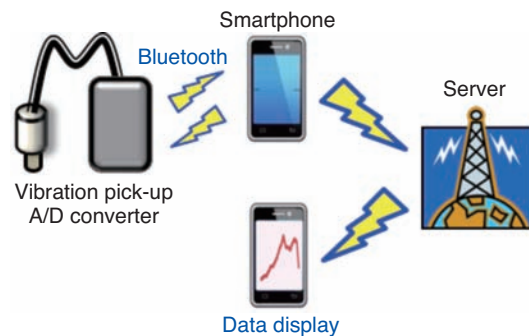


Fig. 9 Layout of handy type failure detection device



Fig. 10 Operation screen and judgment screen

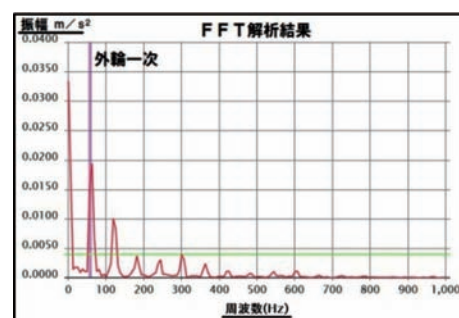


Fig. 11 FFT Analysis Results

be downloaded; therefore, the data can be used for fixed-point monitoring of facilities such as displaying the trend view of past measurement results.

測定結果		
	Peak	RMS
加速度 m/s ²	16.582	3.052
速度 mm/s	3.266	1.331
変位 mm	0.058	0.023

Fig. 12 View of overall values

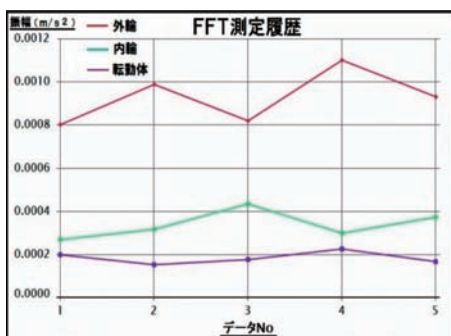


Fig. 13 Trend view of RMS values

5. Participation in the NEDO (New Energy and Industrial Technology Development Organization) project

NTN is participating in the “NEDO Advanced Practical Research and Development of Wind Power Generation” (R&D of Smart Maintenance Technologies) project with other organizations such as the University of Tokyo, to perform experimental evaluations of CMS.

This research and development aims to increase average availability of domestic wind power generation facilities from the current level below 20% to over 23% by developing highly-efficient maintenance techniques and conducting demonstration tests on actual wind turbines. NTN will conduct demonstration tests for this R&D project by installing Wind Doctor® modules to the wind power generation facilities across Japan thereby promoting the further advancement of CMS equipment diagnostic technology.

6. Future development

Power plants in general including wind power are building remote monitoring/controlling systems (SCADA: Supervisory Control and Data Acquisition) to acquire operational data of their facilities and entire sites. We believe that advanced control such as automatic trend analysis and degradation trend

prediction based on much broader information will be enabled by integrating the data obtained from SCADA with data from CMS which is useful for early detection of anomalies.

The ultimate function required for CMS is not only early discovery of damage, but also prediction of remaining life. It is important to know how to minimize the period of downtime due to anomalies; and specification of operating limitations is frequently requested in order to secure preparation time.

However, because the progression from anomaly detection to failure can vary significantly depending on the operating conditions, disturbances and environment, predicting remaining life is fraught with challenges. In the future it may become necessary to employ new analysis methods and to introduce precise diagnostics technologies incorporating not only vibration and displacement data but also acoustic and visual sensing data.

7. Conclusion

We have discussed why CMS is necessary and also NTN's products and activities. We are poised to contribute to further improve availability and reduce maintenance burden of not only wind power generation but also industrial machines in general, by continually advancing high functionality and high performance data acquisition devices and providing highly accurate and useful technology information services.

References

- 1) Akitoshi Takeuchi, Takashi Haseba, Hiroshi Ikeda: Application of Condition Monitoring System for Wind Turbines, NTN TECHNICAL REVIEW, No. 80 (2012) 15-18.

Photo of authors



Keisuke HASHIZUME
CMS Engineering Dept.,
Industrial Machinery Division



Akitoshi TAKEUCHI
CMS Engineering Dept.,
Industrial Machinery Division



Yuzuru TANAKA
CMS Engineering Dept.,
Industrial Machinery Division

Introduction of "ULTAGE" series : High Functionality Roller Bearings

ULTAGE



Shogo TABATA*
Kouhei TODA**
Yasuhiko SHIMIZU***

When it comes to the operational demands put on equipment (such as iron and steel machinery, or wind power generation) and industrial machinery (such as construction and mining machinery, or gearboxes), customers are looking to maximize output and efficiency under more severe usage conditions, like higher vibration and impact loads. In response to these increase demands, NTN developed the ULTAGE® Series of cylindrical, tapered and thrust spherical roller bearings, which deliver the highest load capacity and allowable speed by optimizing the internal design and crowning profile. NTN will release these bearings as the ULTAGE Series which reduce the internal friction resulting in less energy needed to operate.

1. Introduction

Technology development that emphasizes global environmental protection is well underway for every industrial machine.

Bearings used in rotational components of industrial machines are required to have an improved "long life", "high load carrying capacity", "high speed", and "ease of use". To meet this demand NTN has developed the world's-highest level of new-generation bearings known as the "ULTAGE®" series. This series started with precision rolling bearings for main spindles of machine tools and was followed by standardization of new spherical roller bearings, roll neck sealed type 4-row tapered roller bearings for rolling mills, etc. Since then new cylindrical roller bearings, tapered roller bearings and thrust spherical roller bearings have been added to the ULTAGE series. These bearings achieve long life, high load carrying capacity and high speed and are discussed in the following:

2. ULTAGE Cylindrical Roller Bearings

The ULTAGE cylindrical roller bearing is optimized for rolling contact so that the contact pressure distribution between the rolling elements and rolling bearing rings becomes uniform. The features of this bearing are as follows:

2.1 Features

(1) Load carrying capacity (compared with the conventional cylindrical bearings)

- Basic dynamic load rating: 1.2 x
- Basic rating life: 1.8 x

(2) Limiting speed (compared with the conventional cylindrical bearings)

- Max. 1.2 times under oil lubrication condition

(3) Resin cage material is applied as standard

- Applicable for oil and grease lubrication

(4) Allowable inclination (misalignment)

ULTAGE: 1/500 (0.002 rad.)

Conventional cylindrical bearing : 1/2000 (0.0005 rad.)

※ ULTAGE® is a name created from the combination of "ultimate," signifying refinement, and "stage," signifying NTN's intention that this series of products be employed in diverse applications. This is the general name for NTN's new generation of bearings that are noted for their industry-leading performance.

*Industrial Machinery Engineering Dept., Industrial Machinery Division

**New Energy Engineering Department, Industrial Machinery Division

***Construction Machinery and Railway Engineering Department, Industrial Machinery Division

2.2 Structure

Fig. 1 shows an example of the structure of NU type cylindrical roller bearings.

1) Optimized internal design

Adoption of larger diameter rollers and optimized crowning shape enabled use under tough conditions such as larger inclination and heavy load, increasing load carrying performance.

2) Resin cage material is standard

Glass fiber enhanced polyamide resin is used as the material. Resin cages are lightweight and characterized by low torque and low noise.

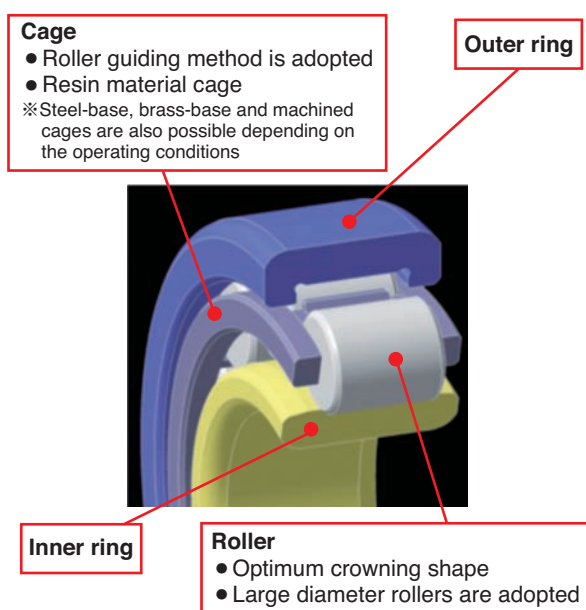


Fig. 1 Design of ULTAGE cylindrical roller bearing

2.3 High Load Carrying Capacity

Fig. 2 shows the stress distribution under the following calculation conditions.

The ULTAGE cylindrical rolling bearing has significantly reduced edge stress compared with the conventional bearings by optimizing the roller crowning shape. In addition, smoothly blending the straight area and crowning area of the outer surface of the roller by applying a new processing method, we have reduced concentration of stress at the starting point of the crowning area seen in the conventional bearing crown designs. This reduces the contact stress even under tough conditions, resulting in improved load carrying performance and bearing life.

<<Calculation Conditions>>

Bearing part number: NU304E ($\phi 20 \times \phi 52 \times 15$)
 Radial load: 7.9 kN
 Inclination: 1/500 (0.002 rad)

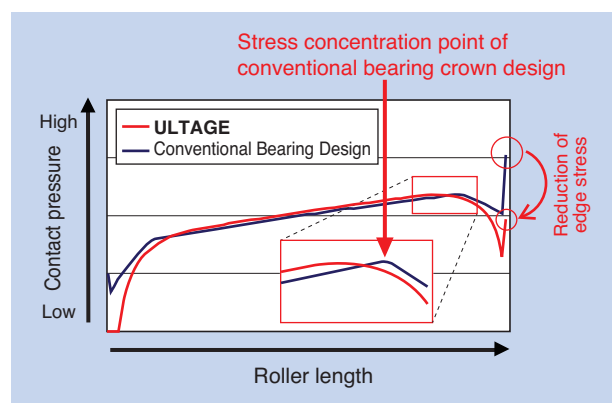


Fig. 2 Contact stress distribution of rollers

2.4 High Speed Operation

(increase of allowable rotational speed)

The ULTAGE cylindrical roller bearings reduces the contact pressure between the rollers and rolling bearing rings and improved the contact conditions between the rollers and rib section. This improves lubrication performance inside the bearings and reduces heat generation allowing a 20% improvement of rotational speed compared with the conventional bearings. Fig. 3 shows the test result of oil lubrication temperature rise.

<<Test Condition>>

Bearing part number: NU307E ($\phi 35 \times \phi 80 \times 21$)
 Radial load: 3.5 kN (5% C_{or})
 Bearing internal clearance: CN clearance (0.025 - 0.050)
 Lubrication: Turbine oil VG32 circulation lubrication

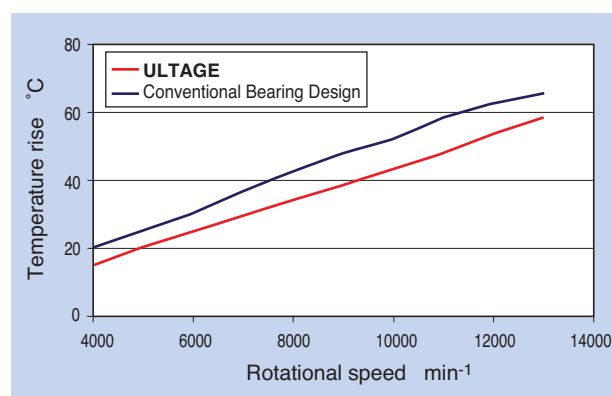


Fig. 3 Temperature rise test results

2.5 Standardized Series

The ULTAGE design will be the standard for cylindrical roller bearings with an outer diameter of 180 mm or less.

3. ULTAGE Large Tapered Roller Bearings

The ULTAGE large tapered roller bearings have the following features by optimizing the internal design of conventional bearings:

3.1 Features

- (1) **Load carrying capacity (compared with conventional tapered roller bearings)**
 - Basic dynamic load rating: 1.3 x
 - Basic rating life: 3 x
- (2) **Limiting speed (compared with conventional tapered roller bearings)**
 - Max. 1.1 times under oil lubrication condition
- (3) **Reduction of running torque**
- (4) **Long-term dimensional variation**
 - 1/10 of bearing steel, 1/4 of case hardening steel
- (5) **Allowable inclination (misalignment)**
 ULTAGE: 1/600 (0.0017 rad)
 Conventional tapered roller bearings: 1/2000 (0.0005 rad)

3.2 Structure

Fig. 4 shows the structure of this bearing.

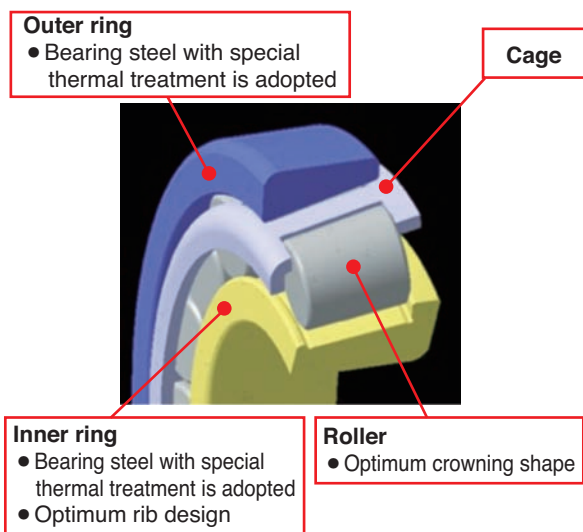


Fig. 4 Design of ULTAGE taper roller bearing

3.3 Higher Load Carrying Capacity

The ULTAGE large tapered roller bearings have improved load carrying capacity compared with the conventional bearings by optimizing the roller crowning. This optimized crowning reduces excessive contact stress and provides uniform contact stress distribution. This reduction of contact stress results in improved bearing life even under tough conditions..

Fig. 5 shows the roller contact stress distribution under the following calculation conditions.

<<Calculation Conditions>>

- Bearing part number: 30316U ($\phi 80 \times \phi 170 \times 42.5$)
- Radial load: 102 kN
- Inclination: 1/600 (0.0017 rad)

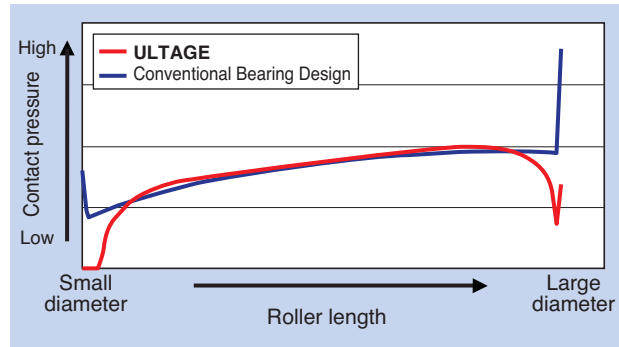


Fig. 5 Contact stress distribution of rollers

3.4 High Speed Operation

(increase of allowable rotational speed)

The ULTAGE large tapered roller bearings have improved the allowable rotational speed by 1.1 times compared with the conventional units by reducing the running torque and temperature rise by optimizing the sliding contact area of the rollers and inner rings as shown in Fig. 6.

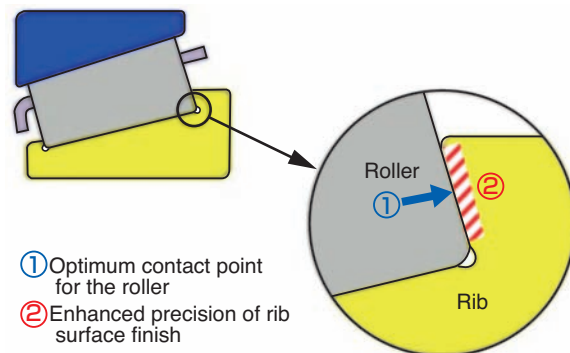


Fig. 6 Contact point between inner ring large end rib face and roller large end face

(1) Temperature Rise Test

Fig. 7 shows the temperature rise test results of the ULTAGE large tapered roller bearing compared with an NTN's conventional bearing and another manufacturer's bearing .

<<Test Condition>>

- Bearing part number : 32940XUE1 ($\phi 200 \times \phi 280 \times 51$)
- Lubrication: Turbine oil VG56 circulation lubrication
- Bearing internal clearance: C2 (0.100 – 0.260)

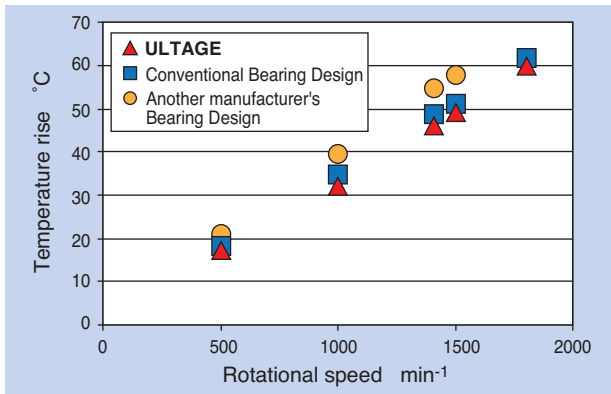


Fig. 7 Temperature rise test results

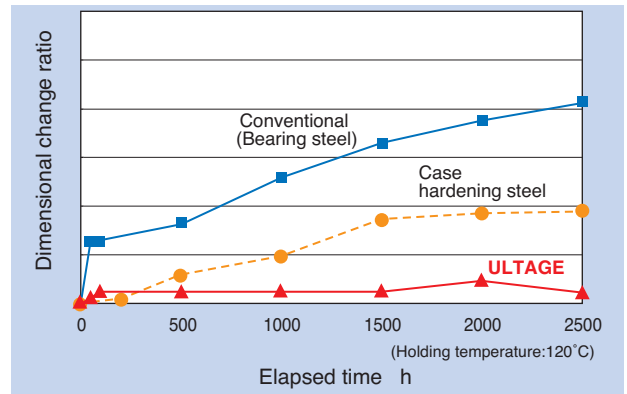


Fig. 9 Dimensional change test results

(2) Running Torque Test

Fig. 8 shows the running torque test results of the ULTAGE large tapered roller bearing compared with an NTN's conventional bearing and another manufacturer's unit.

<<Test Condition>>

Bearing under test: 30316U ($\phi 80 \times \phi 160 \times 42.5$)
 Axial load: 6.9 kN
 Lubrication: Turbine oil VG32
 Temperature: Room temperature

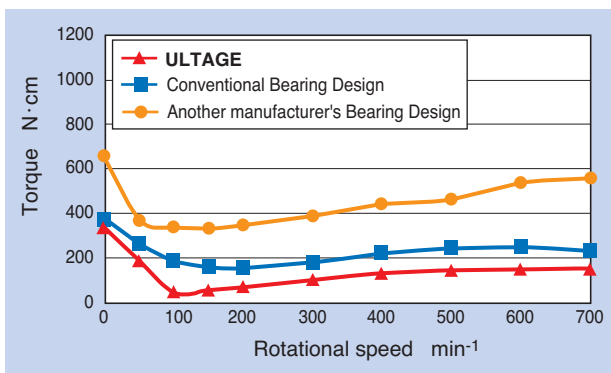


Fig. 8 Running torque test results

3.5 Reduction of Long-Term Dimensional Variation

The operating long-term dimensional variation was reduced to 1/10 or less compared with the conventional bearings using the bearing steel (1/4 or less compared with case hardening steel) by adopting special thermal treated (heat resistant dimensional stability treatment) bearing steel. This result is shown in Fig. 9.

3.6 Standardized Series

The ULTAGE design will be the standard for metric series bearings with an outer diameter of 270 mm or more.

4. ULTAGE Thrust Spherical Roller Bearings

The ULTAGE thrust spherical roller bearings have the following features by optimizing the internal design of conventional bearings:

4.1 Features

- (1) **Load carrying capacity (compared with the conventional units)**
 - Basic dynamic load rating: 1.7 x (max.)
 - Basic rating life: 6 x (max.)
- (2) **Limiting speed (compared with the conventional units)**
 - Allowable rotational speed: 1.2 x (max.)
- (3) **Window type punched steel cage is adopted**
 - Applicable for oil and grease lubrication
- (4) **Heat resistant up to 200°C**
 - Adoption of special heat treatment

4.2 Structure

Fig. 10 shows the structure of this bearing.

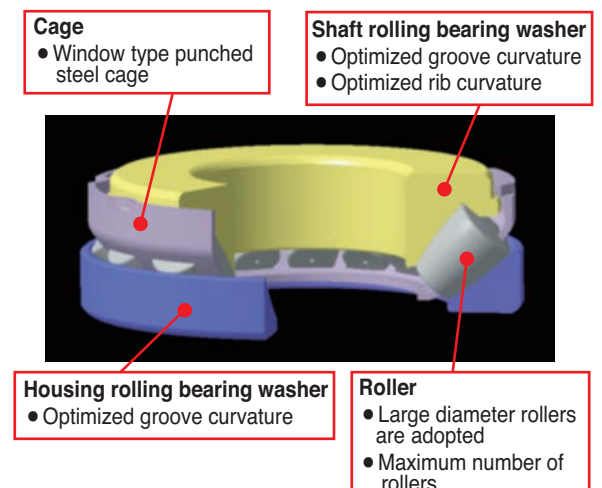


Fig. 10 Design of ULTAGE thrust spherical roller bearing

1) Optimized internal design

The diameter and length of the rollers are maximized and the curvature of the groove and rib is optimized.

2) Adoption of the window type punched steel cage

By adopting a punched steel cage, lubricant can easily flow to the inside of the bearings enabling use of either oil or grease as lubricant.

4.3 High Load Carrying Capacity

The ULTAGE thrust spherical roller bearings achieved the world's-highest level of load carrying capacity by maximizing the diameter and length of the rollers of conventional bearing .

4.4 High speed operation

(increase of allowable rotational speed)

The ULTAGE thrust spherical roller bearings adopts a window type punched steel cage as opposed to the supported-ring-guided machined steel cage of the conventional bearing . In addition, optimization of the rib curvature of the shaft rolling bearing washer reduces the rise of temperature which improved allowable rotational speed by up to 1.2 times compared with the conventional bearing .

Fig. 11 and 12 show the test result of temperature rise of vertical and horizontal shaft tests. In both tests, the rise of temperature was lower than the conventional bearing .

(1) Vertical Shaft Test

<<Test Condition>>

- Bearing part number: 29418E
- Axial load: 98 kN (5% C_{0a})
- Lubrication: Turbine oil VG32 circulation lubrication

(2) Horizontal shaft test

<<Test Condition>>

- Bearings under test: 29418E
- Axial load: 98 kN (5% C_{0a})
- Lubrication: Turbine oil VG32 circulation lubrication

4.5 Standardized Series

The ULTAGE design will be the standard for the 29400Series and bearings with an outer diameter of 130 - 320 mm.

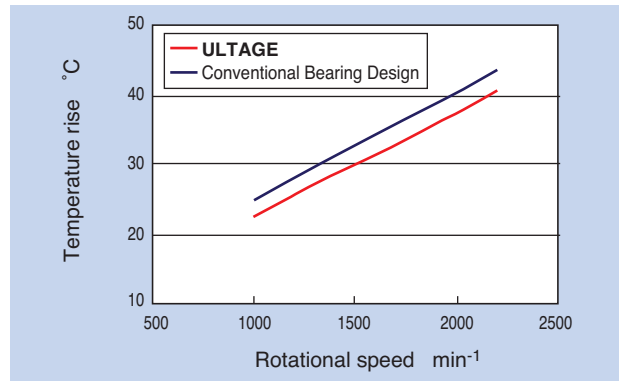


Fig. 11 Temperature rise test results, vertical shaft

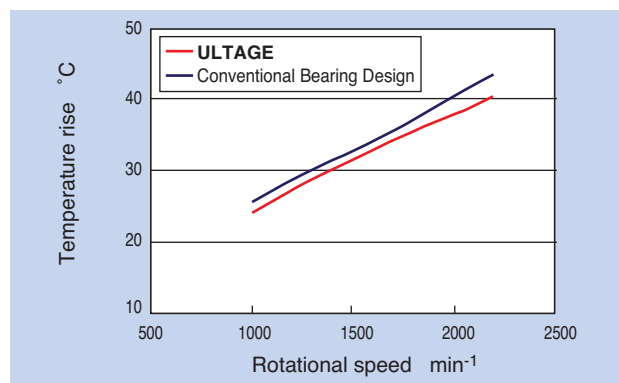


Fig. 12 Temperature rise test results, horizontal shaft

5. Conclusion

Three new types of roller bearings are now added to the NTN next-generation bearings, the ULTAGE Series.

As technology innovation of industrial machines for global environmental protection is currently underway, we believe that bearings featuring high load carrying capacity and high speed will meet the market requirements of industrial machines by being lightweight, compact and having a long-life.

We are poised to continue with the development of next-generation bearings with further improvement and higher functionality that respond to various market demands.

Photo of authors



Shogo TABATA
Industrial Machinery Engineering Dept., Industrial Machinery Division

Kouhei TODA
New Energy Engineering Dept., Industrial Machinery Division

Yasuhiko SHIMIZU
Construction Machinery and Railway Engineering Dept., Industrial Machinery Division

Technical Trend of Aircraft Bearings



Takashi NISHIKAWA*
Nao HAYASHI*
Akiko HAYAKAWA**

There are many different types of bearing for aircraft applications. NTN supplies bearings to jet engine manufacturers all over the world. Recently due to new customer requirements for reducing weight, environmental impact and higher performance, bearing systems are becoming very complicated that require higher reliability and quality controls.

In this paper, NTN's design theory to jet engine main shaft bearings along with the industry trends are documented.

1. Introduction

Demand and sales of commercial aircraft are growing steadily, together with rapid growth of emerging markets, as well as the global expansion of low cost carriers (LCC). Aircraft employ many bearings, and NTN also provides bearings to the key jet engine manufacturers. In this paper, we discuss NTN's activities on the bearings for aircrafts, and bearings for main shafts of jet engines which are used under particularly tough conditions.

2. NTN's activities on bearings for aircraft

Development and manufacturing of aerospace products requires considerably high technology. NTN has established bearing plants dedicated to aerospace applications at NTN Kuwana Works (Mie Prefecture) and NTN-SNR Argonay Works (France) to guarantee high precision and high reliability with utmost quality control. To support this, these plants utilize customer-approved special processes and certified inspectors accredited by the international certification program NADCAP (National Aerospace and Defense Contractors Accreditation Program). Special process operations for the aerospace industry and certification programs of various customers may include heat treatment, surface plating & treatments, non-destructive testing, etc. In addition, final assembly and inspection

processes occur in clean room environments, and customer-authorized quality assurance representatives make final product release decisions.

In addition, NTN's development includes hybrid bearings with rolling elements made of ceramic and raceway rings made of bearing steel, for which demand is expected to grow, nitrided bearings in which raceway rings and rolling elements are nitrided, as well as its own test rig which evaluates dry-run performance to determine if the bearings can be used without seizure, even if the supply of lubricant is interrupted for a certain period.

NTN has technology development sites, in addition to production sites, in Japan and France. Centered on these sites, NTN has been directly dealing with the key jet engine manufacturers, helicopter manufacturers and aerospace businesses not only in Japan and France but around the world, providing a number of high quality products for many years. Recently, NTN's bearings are adopted by General Electric's GENX engine which is used in Boeing 787, Rolls Royce's Trent XWB engine expected to be used by Airbus A350, Pratt & Whitney's GTF engine expected to be used by Mitsubishi MRJ, etc., which are raising NTN's presence in the aerospace industry.

NTN's bearings are used in various parts of aircraft in addition to main shafts of jet engines, such as accessory gear boxes (AGB), flight control systems (FCS), landing gears and auxiliary power units (APU).

*Machining Tool/Aerospace Engineering Dept., Industrial Machinery Division

**Kuwana Works, Industrial Machinery Division

3. Introduction of bearings for main shaft of jet engines

3.1 Types of jet engines

There are four types of aircraft turbine engines: turbojet, turbofan, turboprop and turboshaft, and the former two are usually called jet engines. The most widely used engines are two-shaft turbofan engines featuring high efficiency and low noise; however, three-shaft engines which enable optimization of compressor design are also used. There are also GTF engines equipped with a planetary gear mechanism for driving fans with reduced speed.

Fig. 1 shows the basic structure of a turbofan engine. In this configuration, the air absorbed from the front side of the engine is compressed by the compressor, which is sent to the combustion chamber where fuel is burned and the exhaust drives the turbine. There are two driving systems for the turbine, compressor drive and fan drive, and most of the thrust of a turbofan engine is obtained from the exhaust of the fan.

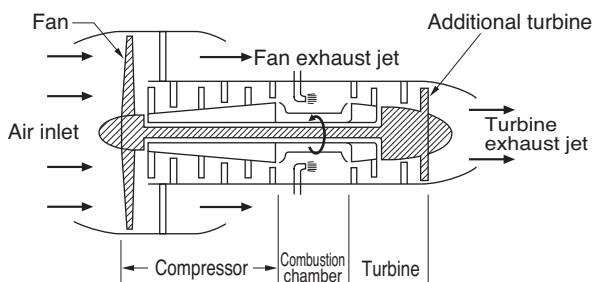


Fig. 1 Outline structure of Turbo fan engine

3.2 Characteristics required for bearings of jet engine main shaft

Key characteristics required for the bearings of jet engine main shaft are:

- Suitable for high-speed rotation
- Operable in high temperature
- Highly reliable and traceable

(1) High speed

An index to evaluate high speed property of bearings includes dn value (bearing inner ring inner diameter (mm) \times inner ring rotational speed (min^{-1})). **Fig. 2** shows dn value of the bearings of the typical use in general industrial machines. The bearings of jet engine main shafts are used under the condition that exceeds dn 2.0×10^6 , therefore, they are required to have superior fatigue life and anti-galling properties. In addition, significant hoop stress is placed on the bearing inner ring due to centrifugal force; therefore, the fracture strength to withstand the force is also required.

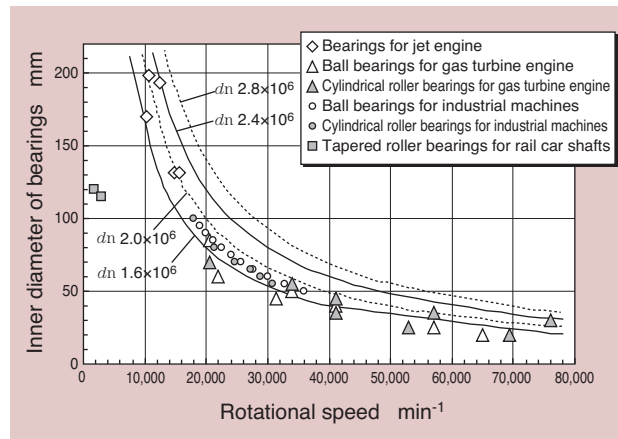


Fig. 2 dn value of bearings

(2) High temperature

The bearings for jet engine main shafts are exposed to temperature of approx. 200°C during operation. In addition, the turbine remains in the so-called heat soak back state where heat is stored with no escape even after the engine stops, which raises the temperature of the bearings to over 300°C . Therefore, low dimensional variation and high fatigue life under high temperature are required.

(3) Reliability and traceability

Since aircraft safety is an absolute requirement, the bearings are also required to have high reliability. We maintain high reliability by conducting full inspections in every step of bearing manufacturing process, such as procurement of material, forging, turning, heat treatment, machining and surface treatment, to verify manufacturing conformity including various certification contents mentioned in the previous section.

In the event of any possible trouble such as damaged bearings, the ability to trace all manufacturing data of every process is also required.

3.3 Main features of bearings of jet engine main shafts

(1) Bearing types

Ordinary jet engines have two shafts, one for the compressor/turbine on the high speed/high pressure side, and the other one for the fan/compressor/turbine on the low speed/low pressure side. The bearings have a role to support them.

The bearing types for jet engine main shafts are mainly three-point contact ball bearings and cylindrical roller bearings as shown in **Fig. 3**. The three-point contact ball bearings support load in the axial and radial directions.

They can support both directions of axial loads. The inner rings of these bearings can be split to incorporate

as many balls as possible to ensure long life under a large load. The cylindrical roller bearings are used as floating-side bearings in order to absorb longitudinal expansion/contraction of the engine's main shaft while supporting radial load.

Fig. 4 shows the bearings for main shafts used on Boeing's passenger aircraft B767.

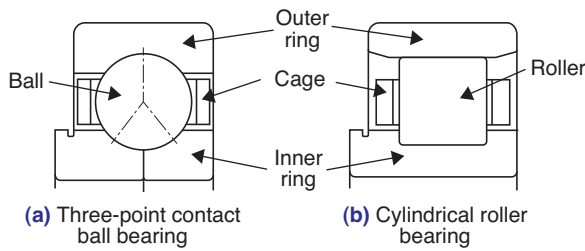


Fig. 3 Bearing types for jet engines



(a) Three-point contact ball bearing (b) Cylindrical roller bearing

Fig. 4 Examples of main shaft bearings of jet engine

(2) Bearing material

The material of bearings for jet engine main shafts requires long life, dimensional stability, high strength and high wear resistance, particularly under high temperature. For raceway rings and rolling elements, high speed steel such as molybdenum-based AISI M50 or tungsten-based T1 is used. As shown in Fig. 5, M50 has hardness of around 58HRC at 300°C and high dimensional stability.

When bearings are used under high speed rotation, centrifugal force is applied to the inner rings and the tensile stress on the circumferential direction of the inner rings (hoop stress) will increase. In case of through-hardening steel such as M50, once exfoliation starts at the inner rings, cracking may progress very fast resulting in fracture of the inner rings; therefore, heat-resistant carburized steel AISI M50NiL may be used. Fig. 7 shows the comparison of fracture toughness.

Cages are frequently used with SAE4340 steel hardened to around 30HRC.

Usually, the bearings of aerospace applications must only use the material certified by the aircraft manufacturers or engine manufacturers.

NTN also procures the material from suppliers certified by the engine manufacturers.

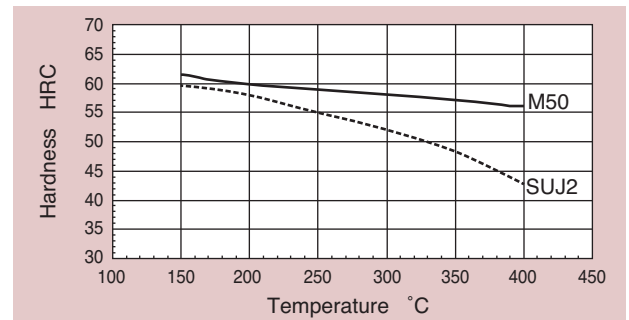


Fig. 5 Hardness of bearing steel for high temperature

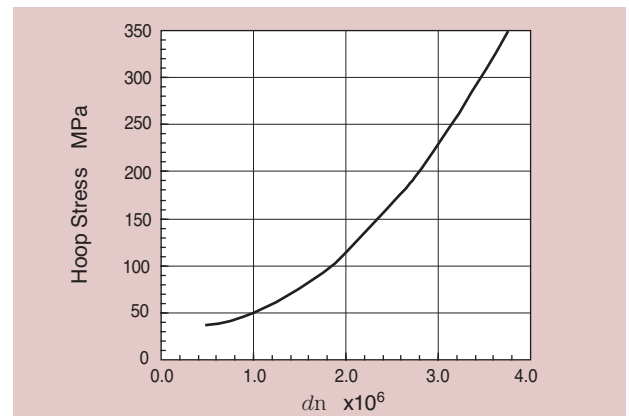


Fig. 6 Hoop stress on bearing inner ring

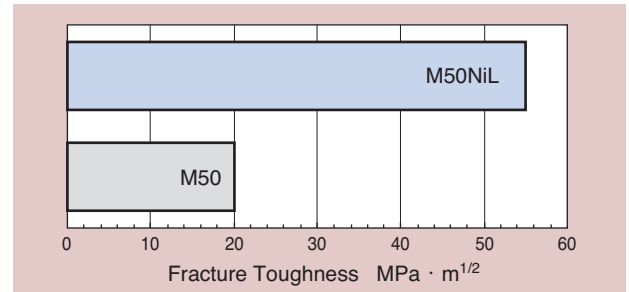


Fig. 7 Comparison of fracture toughness

(3) Bearing design

In order to absorb vibration produced at the main shaft in high speed rotation, the outer ring is unitized with the vibration absorbing components with springs which are supported by the oil damper, as shown in Fig. 8. Currently, the vibration absorbing components are most likely unitized with the outer ring in order to reduce the weight and number of components.

Fig. 9 shows an example of the commercially available unitized bearings.

The cylindrical roller bearings have low load carrying requirements because they only support the main shaft weight as the radial load and the force that the inner ring drives to the rollers is also relatively small. Sliding between the rollers and the raceway may cause early wear. Therefore, in some cases, the outer diameter is

made into an oval shape so that preload is given to the rollers when they are assembled into the housing.

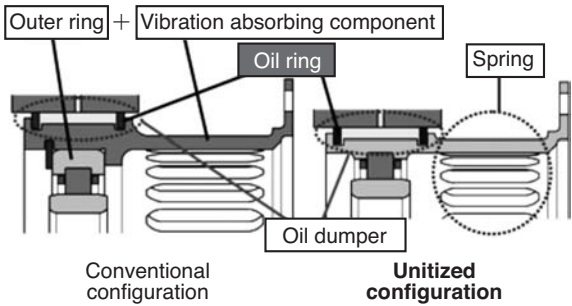


Fig. 8 Unitized bearings



Fig. 9 Unitized model of a bearing

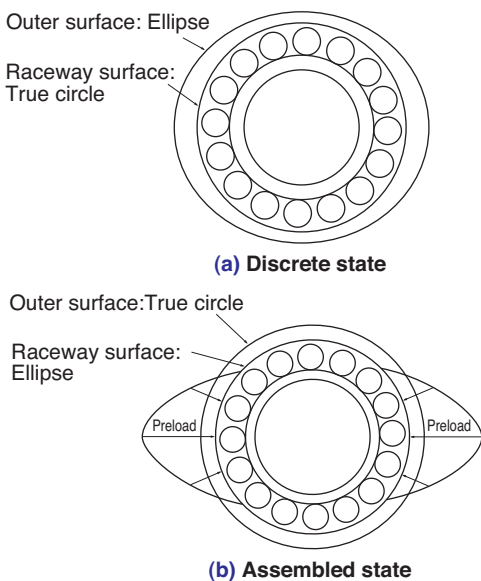


Fig. 10 Non-true circle cylindrical roller bearing

(4) Lubrication

Mineral oil based SAE1010 was used as lubricant of early jet engines, however, its fast oxidative degradation due to the use under high temperature affected the bearing life.

The first solution to this challenge was the development of synthesized ester base MIL-L-7808. Then, MIL-L-23699 was developed with improved load carrying performance and currently, MIL-PRF-23699 is

most widely used as the lubricant for jet engines. In addition, lubricant oil with superior oxidation stability under high temperature and sludge resistance is also developed and standardized as MIL-PRF-23699 HTS. Along with this, the conventional oil MIL-PRF-23699 was standardized as MIL-PRF-23699 STD.

The lubricant must be delivered to the rolling contact surface of the bearings and the contact area between the cage guiding surface and land. Therefore, forced lubrication is required, such as oil jet lubrication where the high speed lubricant is injected from the nozzle (shown in Fig. 11).

Along with the high speed rotation of the main shaft, a “wall” of air, or so-called “air curtain”, is formed due to the rotation of the rolling elements and the cage, which prevents sufficient delivery of lubricant oil injected from the nozzles. In that case, under-raceway lubrication is used to deliver oil to the required area with the centrifugal force. Fig. 12 shows an example of under-raceway lubrication.

The oil jet injected from the nozzle is captured by the oil scoop and guided to inside the main shaft. Then, the oil is supplied into the bearing with the centrifugal force. Since the under-raceway lubrication delivers the oil directly into the inner ring of the bearings, the cooling effect on the bearings is higher than with oil jet lubrication.

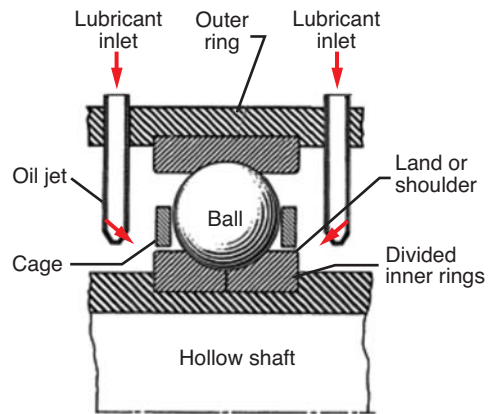


Fig. 11 Oil jet lubrication

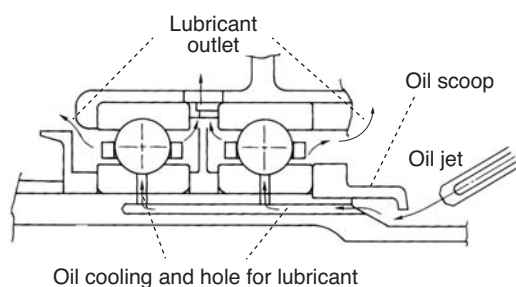


Fig. 12 Under-raceway lubrication

(5) Surface treatment

On the cage guide surface, sliding friction between the cage and the land cannot be prevented; therefore, good friction properties and wear resistance are required. In order to obtain good friction properties, secure delivery of lubricant oil to the cage guide surface is required and the above mentioned under-raceway lubrication is used. In addition, the cage surface is silver plated to prevent contact between the similar metals. The main standard for this silver plating is AMS2414.

The land surface on the rolling bearing rings shown in Fig. 13 may be TiN coated, which is a type of hard ceramic, in order to improve wear resistance.

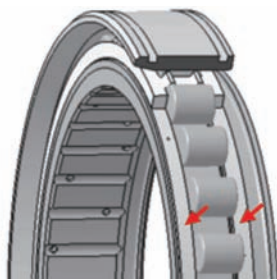


Fig. 13 TiN coating

3.4 Technology development for bearings of jet engine main shafts

Recent jet engines are designed to operate at higher temperature and pressure for lower fuel consumption and lighter weight, and the structure of the bearings for jet engine main shafts is becoming more complicated. Therefore, reliability of bearings must be improved. This important development task is being pursued on several fronts:

1) Surface modification

Common causes of bearing degradation are exfoliation and adhesion, which originate from surface defects such as indentations produced by hard foreign objects.

Raceway hardening processes via surface modification are being developed to reduce such degradation and achieve high reliability.

2) Rolling element material

We are considering use of ceramics (Si_3N_4) which is light with the specific gravity of approx. 40% of M50 and exhibits good friction and wear properties for the rolling elements in order to reduce the contact pressure between the rolling elements and the raceway rings due to high speed rotation. However, since high reliability is required for its application in bearings for jet engine main shafts, we are working on establishment of a high precision non-destructive testing method for detecting defects.

4. Conclusion

Bearings are used in various locations of aircraft, including jet engines. NTN has been providing a number of high quality bearings for many years, and guaranteeing high precision and high reliability through comprehensive quality control.

Bearings for jet engines are expected to face increasingly severe operating conditions considering the ongoing development of high performance jet engines. NTN will continue to advance research and development of new technologies recognizing the importance of bearings in jet engines. At the same time, we are poised to contribute to the aerospace industry by providing our high technology and quality to customers around the world through our participation in new development projects with jet engine and helicopter manufacturers, among others.

References

- 1) Masuji Matsuoka: Koku Kagaku Koza Vol. 11 Jet Engine (Structure)
- 2) NTN TECHNICAL REVIEW, No.67 (1998) 7.
- 3) NTN Bearing Engineer, Vol. 21, Issue 1 (1972) 61.
- 4) NTN Naoki Matsumori, Bearings for Jet Engine Main Shafts to Protect Safety of Aircrafts, Tool Engineer, Vol. 54 No 13, Taiga Publishing Co., Ltd. (2013) 61.

Photo of authors



Takashi NISHIKAWA
Machining Tool/Aerospace
Engineering Dept.,
Industrial Machinery Division



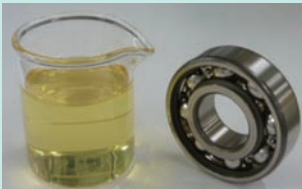
Nao HAYASHI
Machining Tool/Aerospace
Engineering Dept.,
Industrial Machinery Division



Akiko HAYAKAWA
Kuwana Works,
Industrial Machinery Division

The Influence of the Humidity and Quantity of Hydrogen into Steel under the Abrasive Wear

Motohiro ITO*



An early bearing damage is occurred and accompanied by unique white microstructures in the raceway subsurfaces. The main cause is thought to be the result of hydrogen embrittlement caused by generated hydrogen from decomposition of lubricant and containing water. It is considered that hydrogen embrittlement is occurred by penetrated diffusible hydrogen. There is a method to detect diffusible hydrogen in

steel. This method measures the specimen that is worn under abrasive wear by thermal desorption analysis. In this report, we tested abrasive wear in space that is controlled humidity and investigated that relationship between humidity and penetrated diffusible hydrogen into steel via abrasive wear.

1. Introduction

Early flaking together with distinctive white structural change observed in roller bearings is considered to be mainly caused by hydrogen¹⁾. The mechanism of this phenomenon is assumed that the hydrogen produced by hydrolysis of the lubricant or water inside the bearings penetrates the steel causing the steel to become brittle and separate²⁾⁻⁴⁾. In addition, the hydrogen which causes the embrittlement is considered to be diffusible hydrogen.

In order to detect the diffusible hydrogen, two methods can be used. One method is to have hydrogen electrochemically penetrate into steel and capture the permeated hydrogen as the ionized current⁵⁾. The second method is to have hydrogen penetrate into steel under a corrosive environment and apply thermal desorption analysis (TDA)⁶⁾.

Diffusible hydrogen derived from water or lubricant hydrolysis can be detected by thermal desorption analysis after abrasive wear of steel by emery paper while water or oil is dropped on the steel⁷⁾. However, diffusible hydrogen is also detected in the dry abrasion test where no water or oil is applied. Therefore vapor in the atmosphere may also contribute⁷⁾.

In this paper, we have investigated the amount of hydrogen that penetrated into steel and the impact of temperature on the amount through abrasive wear under the environment with controlled temperature and humidity.

2. Wear test

Fig. 1 shows an overview of the test equipment and **Table 1** shows the wear test conditions. In this test, emery paper #220 was set on the rotary surface table and three SUJ2-material disks were set on the specimen holder. The chamber is designed to provide air circulation with which the temperature and humidity are controlled by an air conditioner. The load on the specimen is provided by a weight with a target of 85.4 kPa of contact pressure. The wear test was conducted applying 5 ml of test oil on the emery paper before the test and then dropping 1 ml/min of test oil during the test. Both the rotary surface table and the specimen holder rotate with the rotational speed of the rotary surface table, at the center of the specimen holder, being 0.59 m/s and the rotational speed of the specimen holder, at the center of the specimen, being 0.03 m/s.

Fig. 2 shows the shape of the specimens and **Table 2** shows the processing conditions of the specimens. The specimen is SUJ2 processed with ordinary quenching at 850°C and tempering at 180°C x 2 h.

Table 3 shows various wear test conditions using mineral oil, water-added oil and fluorine-based oil.

For mineral oil, additive-free turbine oil VG100 was used.

The temperature in the test chamber was set to 20°C and 30°C and several levels of relative humidity values were used ranging of 25 to 95%RH. The wear test

*Advanced Technology R&D Center

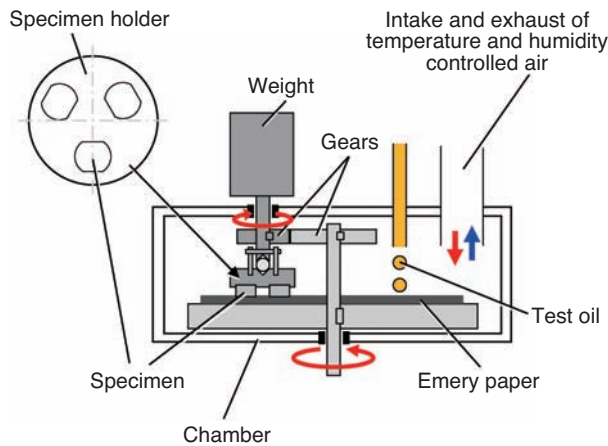


Fig. 1 Schematic of test rig

Table 1 Wear test common condition

Number of specimens	Three
No. of emery paper	#220
Table rotation speed at the center of specimen holder	0.59 m/s
Holder rotation speed at the center of specimen	0.03 m/s
Contact pressure	85.4 kPa
Drop rate	1 ml/min

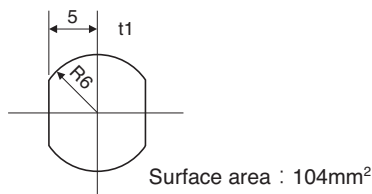


Fig. 2 Specimen shape (unit: mm)

Table 2 Disposal condition of specimen

Material	SUJ2
Thermal processing	Quenching temperature: 850°C, tempering: 180°C×2 h

Table 3 Each wear test conditions

Item	Mineral oil	Water added oil	Fluorine-based oil
Test oil	Additive-free turbine oil VG100		Perfluoro-polyether oil
Amount of added water	0 wt%	2, 5, 10, 15 wt% (Pure water)	0 wt%
Set temperature	20, 30 °C	30 °C	
Set relative humidity	25~95 %RH	25, 95 %RH	25, 60, 95 %RH
Abrasive wear time	40 min		20, 30, 40 min

duration was 40 minutes.

In order to verify the impact of water mixed in oil, a wear test was also conducted using water-added oil. For water-added oil, additive-free turbine oil VG100 with pure water was used. The amount of added water was 2, 5, 10 and 15 wt%, with a set temperature of 30°C and two relative humidity conditions, 25%RH (low humidity) and 95%RH (high humidity).

Diffusible hydrogen in steel after the wear test is considered to be derived not only from water but also from the decomposition of the mineral oil. In order to verify the impact of hydrogen from hydrolysis, a wear test was conducted with fluorine based oil which does not contain hydrogen in the chemical structural formula. For fluorine-based oil, additive-free perfluoro-polyether oil with kinematic viscosity at 40°C adjusted to 100 mm²/s was used. A set temperature of 30°C and relative humidity of 25, 60 and 95%RH were used in the test chamber. The wear test duration was set at 20, 30 and 40 minutes.

3. Thermal desorption analysis

After the wear tests, 3 specimens were cleaned and added to the analyzer tube for thermal desorption analysis. The rate of temperature rise was set to 180°C/h and the final test temperature was set to 540°C. A thermal conductivity detector (TCD) was used as the hydrogen detector. Fig. 3 shows an example of TDA profiles. The diffusible hydrogen was defined as the total amount of hydrogen emitted up to 200°C.

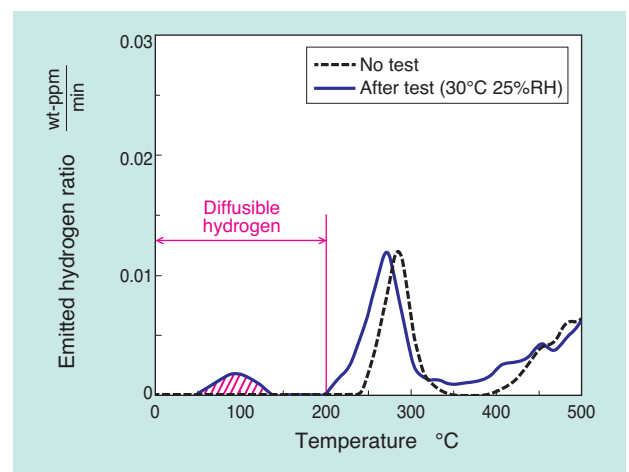


Fig. 3 An example of TDA profiles

4. Mineral oil

Fig. 4 shows the TDA profile of the specimen before and after the abrasive wear tests. No diffusible hydrogen emission was detected in the “no test” case. The emitted diffusible hydrogen increased as the relative humidity increased at both 20°C and 30°C.

Fig. 5 shows the relation between the relative humidity and amount of diffusible hydrogen. At both set temperatures of 20°C and 30°C, a high correlation was observed.

Fig. 6 shows the relation between the absolute humidity and amount of diffusible hydrogen.

The absolute humidity was obtained based on the measured temperature and relative humidity.

There was a strong correlation between the absolute humidity and amount of diffusible hydrogen with little impact of temperature.

The results show that the amount of diffusible hydrogen in steel is dependent on the amount of vapor in the unit volume of air.

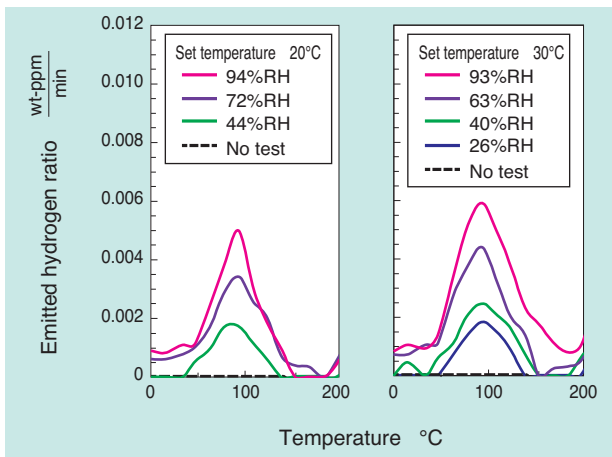


Fig. 4 TDA profiles of specimens before and after abrasive wear testing

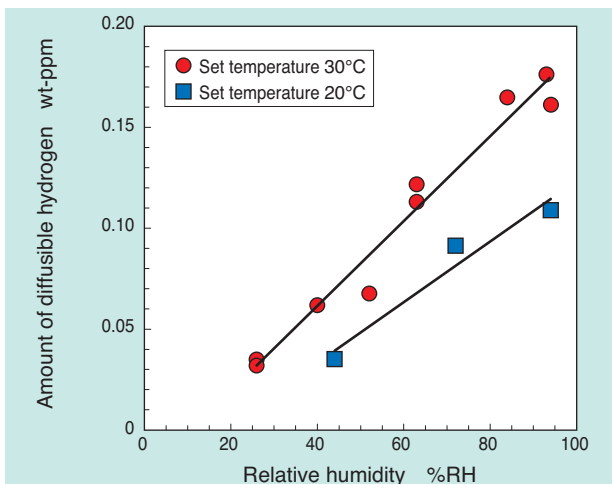


Fig. 5 Relationship between relative humidity and amount of diffusible hydrogen

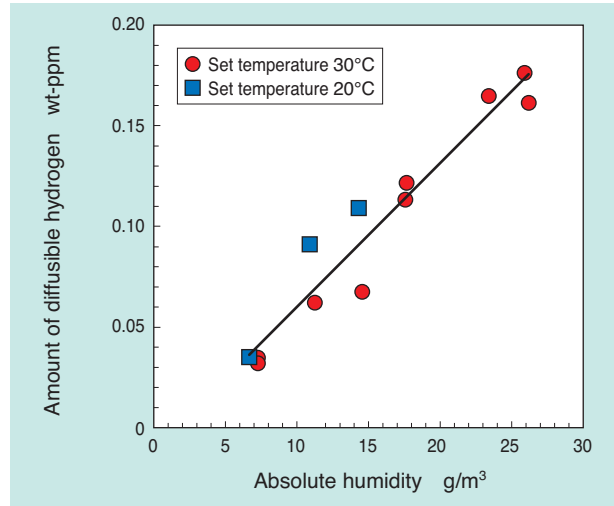


Fig. 6 Relationship between absolute humidity and amount of diffusible hydrogen

5. Water added oil

Fig. 7 shows the relation between the amount of added water and amount of diffusible hydrogen. Both in the low humidity and high humidity cases, as the amount of water increased, the amount of diffusible hydrogen increased. The amount of diffusible hydrogen in the low humidity test, excluding the 15 wt% water added oil, was less than the amount of diffusible hydrogen in the high humidity test, excluding the water-free oil.

When water added oil was used, the amount of diffusible hydrogen increased compared to the water-free oil in both high and low humidity. This indicates that the water added to the grease as well as the small amount of water vapor in the air both contributed to as diffusible hydrogen sources to the new steel surface produced during abrasion.

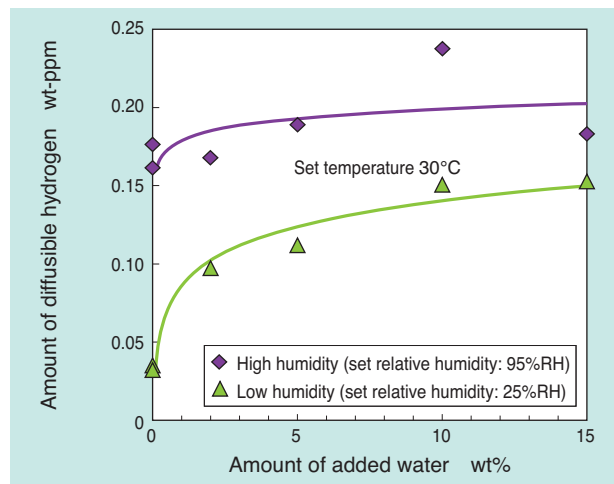


Fig. 7 Relationship between amount of containing water and amount of diffusible hydrogen in cases of water containing oils

However, the amount of diffusible hydrogen in the low humidity test, excluding the 15 wt% water added oil (0.153wt-ppm), was less than the amount of diffusible hydrogen in the high humidity test, excluding water-free oil (0.176wt-ppm). This shows that the impact on diffusible hydrogen into the steel after abrasion was larger for water vapor in the air than that of water added directly to the test oil.

Table 4 shows the amount of water involved in the abrasive wear test and the amount of diffusible hydrogen. Since the volume of the test chamber is 0.0104 m³, the amount of vapor contained in the test chamber air is 0.080g in low humidity and 0.271g in high humidity. When 15 wt% of water was added to the test oil, with a drop rate of 1 g/min and an abrasion test duration of 40 minutes, the amount of water in the dropped oil was 6g. The total amount of water when 15 wt% water added oil was used in low humidity was 6.080g (6 + 0.080g).

On the other hand, when water-free oil was used in high humidity, the amount of water was 0.271 g. This shows that while the amount of water involved in the abrasive wear test was larger in the case of 15 wt% water added oil in low humidity versus that of water-free oil in high humidity, the amount of diffusible hydrogen was smaller. While the reason why the amount of diffusible hydrogen varies depending on the state of water is unclear, the test result showed humidity had a larger impact on the amount of diffusible hydrogen in steel after the abrasion test.

Table 4 Amount of water and amount of diffusible hydrogen in wear test

Item	Low humidity (25%RH) + added water (15 wt%)	High humidity (95%RH) + no added water (0 wt%)
Volume of chamber space	約 0.0104 m ³	
Absolute humidity	7.6 g/m ³	25.9 g/m ³
Amount of water in the chamber	0.080 g	0.271 g
Drop rate	1 g/min	
Test time	40 min	
Amount of added water	15 wt%	0 wt%
Amount of water in oil	6 g	0 g
Total amount of water	6.080 g	0.271 g
Diffusible hydrogen	0.153 wt-ppm	0.176 wt-ppm

5.1 Relationship between humidity and water contained in oil

It was shown that the amount of diffusible hydrogen in steel after the abrasive wear test depends on the amount of vapor in the air. It was also shown that the impact of humidity is larger than the impact of added water to the lubricant. Therefore, we investigated the water content of the oil when exposed to different humidity conditions in order to verify the impact of humidity on water content of the oil.

Table 5 shows the test conditions for measuring the water content. The same additive-free turbine oil VG100 was used. A set temperature of 30°C and relative humidity of 30, 60 and 90%RH were used for the test chamber. The container with test oil was exposed in the test chamber for 30 minutes, then the water content was measured.

Fig. 8 shows the measurement results of the water content in the oil. As the absolute humidity increased, the water content in the oil also increased.

This means that in high humidity the amount of water contained in oil increased.

It is considered that as humidity increases, water contained in the oil increases and becomes the source of hydrogen. Therefore, diffusible hydrogen in steel depends on the amount of water vapor in the air.

Table 5 Water content of oil test condition

Test oil	Additive-free turbine oil VG100
Set temperature	30°C
Set relative humidity	30, 60, 90 %RH
Exposure time	30 min

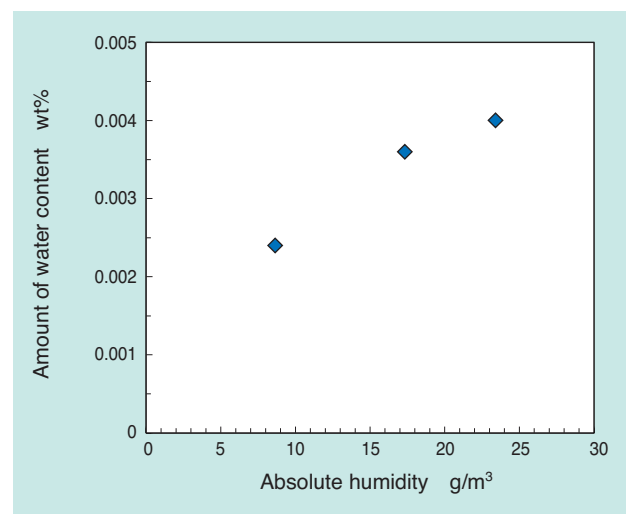


Fig. 8 Water content of oil

6. Fluorine-based oil

Fig. 9 shows the TDA profile of the specimen before and after the wear tests. After the abrasive wear test, diffusible hydrogen was detected from every specimen and the amount of diffusible hydrogen increased as the relative humidity increased (in their respective abrasion duration). As the abrasion time increased, diffusible hydrogen increased.

Fig. 10 shows the relationship between the relative humidity and amount of diffusible hydrogen with fluorine-based oil. There is a high correlation observed for all abrasion times.

Fig. 11 shows the relationship between the abrasion time and amount of diffusible hydrogen.

As the abrasion time increased, diffusible hydrogen increased for a given relative humidity.

In the abrasive wear test using mineral oil, diffusible hydrogen was detected from steel and a high correlation was observed between the absolute humidity and diffusible hydrogen. From this, it was shown that the amount of diffusible hydrogen in steel after an abrasive wear test depends on the amount of vapor contained in the unit volume of air. However, in case of mineral oil, the source of diffusible hydrogen could derive not only from the vapor contained in the air

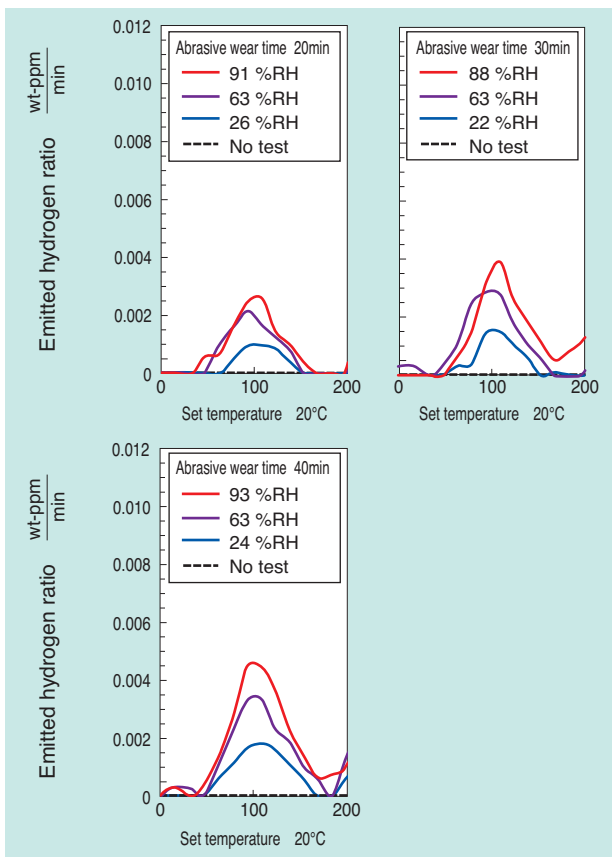


Fig. 9 TDA profiles of specimens before and after abrasive wear testing in cases of fluorine based oil for wear duration of 20, 30, 40 min

but also from decomposition of mineral oil. Therefore, we conducted an abrasive wear test using fluorine-based oil to obtain correlation between the increase of humidity and increase of diffusible hydrogen. Since fluorine-based oil does not contain hydrogen in the chemical structural formula, diffusible hydrogen detected in the abrasive wear test using fluorine-based oil derives only from water.

In addition, since the abrasive wear tests indicate a linear increase of diffusible hydrogen within the test range, it is assumed that diffusible hydrogen is not saturated in the steel but is in a transient state. Therefore, it is possible that the impact of humidity will be more significant when abrasion takes longer time than these tests.

The impact of humidity on the amount of hydrogen penetrated in steel has not been reviewed until now. However, this result indicates that the impact of humidity is a significant factor.

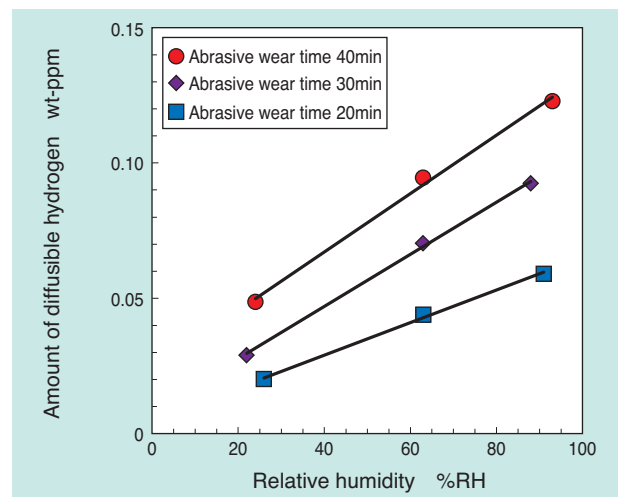


Fig. 10 Relationship between relative humidity and amount of diffusible hydrogen in cases of fluorine based oil

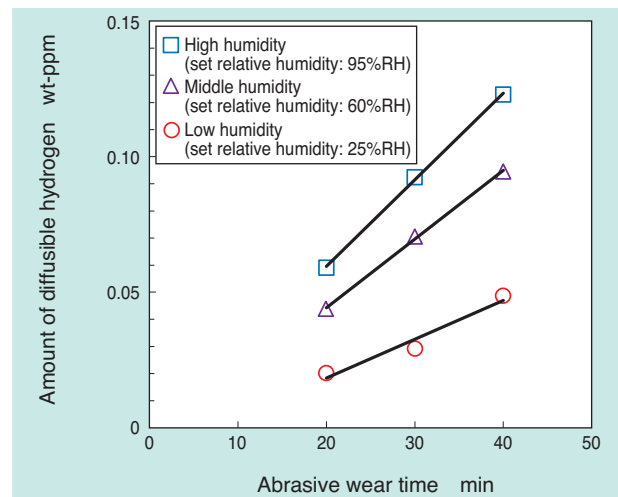


Fig. 11 Relationship between wear duration and amount of diffusible hydrogen in cases of fluorine based oil

7. Conclusion

We have investigated the impact of humidity on the amount of hydrogen penetrated in steel by conducting an abrasive wear test in a chamber under controlled temperature and humidity and applying thermal desorption analysis. As a result, the following were revealed:

- 1) When the abrasive wear test was conducted using mineral oil, the amount of diffusible hydrogen increased as the relative humidity increased for a given temperature. When absolute humidity was used instead of relative humidity in the arrangement of data, a strong correlation was observed with the amount of diffusible hydrogen.
- 2) When the abrasive wear test was conducted with pure water added to mineral oil, the amount of diffusible hydrogen increased both in low and high humidity.
Within the range of ambient temperature in this test, the amount of diffusible hydrogen in the low humidity test, excluding the 15 wt% water added to oil, was less than the amount of diffusible hydrogen in the high humidity test, excluding no water added to oil.
- 3) Even when fluorine-based oil was used, which does not contain hydrogen atoms in the chemical structural formula, diffusible hydrogen was detected from the steel. The amount of diffusible hydrogen increased when the abrasive wear duration was increased.

References

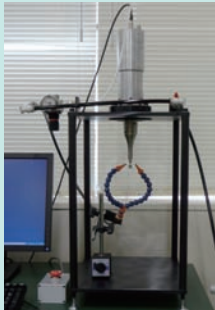
- 1) K. Tamada, and H. Tanaka, "Occurrence of brittle flaking on bearings used for automotive electrical instruments and auxiliary devices" *Wear*, 199 (1996), pp. 245-252.
- 2) M. Kohara, T. Kawamura and M. Egami, "Study on Mechanism of Hydrogen Generation from Lubricants" *Tribology Transactions*, 49 (2006), pp. 53-60.
- 3) L. Grunberg, "The Formation of Hydrogen Peroxide on Fresh Metal Surfaces" *Proc. Phys. Soc (London)*. B66 (1953), pp. 153-161.
- 4) P. Schatzberg and I. M. Felsen, "EFFECTS OF WATER AND OXYGEN ROLLING CONTACT LUBRICATION" *Wear*, 12 (1968), pp. 331-342.
- 5) Shigeru Asano, Yoshio Fujishima, Namio Ohtani, "The Diffusivity of Hydrogen in Iron at Room Temperature", *Journal of The Japan Institute of Metals*, Vol. 37, Issue 3 (1973), pp. 301-306.
- 6) M. Nagumo, M. Nakamura, and K. Takai, "Hydrogen Thermal Desorption Relevant to Delayed-Fracture Susceptibility of High-Strength Steels" *METALLURGICAL AND MATERIALS TRANSACTIONS A*, 32A (2001), pp. 339-347.
- 7) Hiroyoshi Tanaka, Hiraku Tanimoto, Joichi Sugimura, "Observation of Hydrogen Permeation into Fresh Bearing Steel Surface by Thermal Desorption Spectroscopy", *Proceedings of Japan Tribology Conference Tokyo (2010-5)*, pp. 203-204.

Photo of author



Motohiro ITO
Advanced Technology
R&D Center

Evaluation of Shear Fatigue Properties in Medium Carbon Steels and Rolling Bearing Steels up to Giga-cycle Test Regimes



Noriaki MIWA*

We have developed an ultrasonic torsional fatigue tester which enables for the rapid evaluation of shear fatigue properties of high strength steels. This report presents the test results of shear fatigue properties of induction hardened medium carbon steels, and rolling bearing steels, up to giga-cycle regimes as evaluated by the developed tester.

1. Introduction

Repetitive torsional load is applied to the shafts of constant velocity universal joints, which are used in front-wheel drive and four-wheel drive vehicles and industrial machines. Therefore, it is important to investigate shear fatigue properties up to giga-cycle test regimes in order to guarantee long-term reliability of the materials. As one of the stresses governing generation of cracks before internal-originated cracking in rolling bearings, NTN can report completely reversed alternative shear stress acted repeatedly on the surface¹⁾. Therefore, it is important to evaluate shear fatigue properties in order to determine life of rolling bearings.

The shear fatigue life can be obtained by a torsional fatigue test. However, since the load frequency of the conventional torsional fatigue tester is low, evaluation up to 1×10^9 cycles has been practically impossible. Therefore, we developed an ultrasonic torsional fatigue tester (USTF tester) aimed at rapid evaluation of shear fatigue properties of high strength steel. Since the commercially available torsion vibration converters have low power, we optimized the shapes of torsion amplitude magnifying horns and specimens and succeeded to provide shear stress amplitude of around 950 MPa max²⁾. In this paper, we discuss the following shear fatigue property evaluation results using the developed ultrasonic torsional fatigue tester:

- (1) Impact of B on shear fatigue properties of induction hardened medium carbon steels up to 1×10^9 cycles
- (2) Relationship between shear fatigue life and rolling fatigue life of bearing steels obtained by an ultrasonic torsional fatigue test.

2. Impact of boron (B) on shear fatigue properties of induction hardened medium carbon steels up to 1×10^9 cycles

2.1 Background

Induction hardened medium carbon steel S40C is used for the shafts of ordinary constant velocity joints. When the shaft diameter is relatively small, the material with increased manganese (base steel) is used to improve the quenching property and when the shaft diameter is large, boron (B) is added to the base steel or its equivalent (boron-added steel) to further increase the quenching property. NTN has evaluated shear fatigue properties of shaft materials up to 1×10^9 cycles with an ultrasonic torsional fatigue tester and investigated the impact of added boron on the fatigue properties.

2.2 Test method

Boron-added steels, where 19 ppm of boron and 420 ppm of Ti are added to the base steel, were used as test materials. Fig. 1 shows the induction hardening conditions and Fig. 2 shows the diagram of the sample. The gray area of Fig. 2 is heated to adjust the hardness of the hatched area including the smallest diameter area to 700 HV. Then, the specimen is tempered at $170^\circ\text{C} \times 1\text{h}$ and finished by grinding. To eliminate the impact of surface roughness, emery abrasion (#500 and #2000) and diamond wrapping (grain size of $1 \mu\text{m}$) were applied for a mirror finish before the ultrasonic torsional fatigue test. Resonance frequency of 20000 Hz and stress ratio $R = -1$ (completely reversed) were used as the test conditions. When a shear fatigue crack is generated and propagated in the sample, resonance frequency

*Advanced Technology R&D Center

decreases.

It was determined that the sample was damaged when resonance frequency exceeded the preset range, and the test was terminated. Since continuous loads would cause the specimen to heat up in the USTF test, an intermittent load method was used, alternating loads and pauses³⁾. In the case of shear stress amplitudes of more than 700 MPa, 0.11 sec of load and 1.1 sec of pause were used until damage was detected from heat generation.

In the case of less than 700 MPa, 0.11 sec of load and 1.1 sec of pause were used 1×10^7 times, then the conditions were changed to 1 sec of load and 0.2 sec of pause. When no damage was detected up to 1×10^9 cycles, the test was terminated. The real load frequency of 0.11 sec of load and 1.1 sec of pause is 1803 Hz and that of 1 sec of load and 0.2 sec of pause is 16529 Hz²⁾.

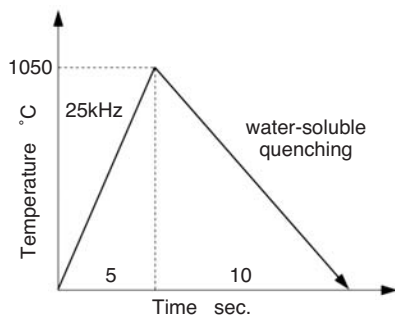


Fig. 1 Induction heat treatment condition



Fig. 2 Specimen shape and hardened region

2.3 Results and observation

Fig. 3 shows the S-N curves of the base steel and the Boron-added steel. S-N curves were obtained by applying the fatigue test results to the continuous drop single logarithm curve model of the Standard Regression Method of S-N Curves from the Society of Materials Science, Japan. Fatigue strength of the base steel and Boron-added steel after 1×10^8 cycles with 10% fracture probability was 636 MPa and 643 MPa, respectively, almost equal.

Shear type initial cracks started at the smallest diameter, and propagated and transitioned to tensile type. Shear type initial cracks are either axial or radial and the latter are plotted with a horizontal line in Fig. 3. Fig. 4 shows the SEM images of the fracture surface at initial shear fatigue cracking. Both materials exhibited transgranular fracture. Although B is reported to be

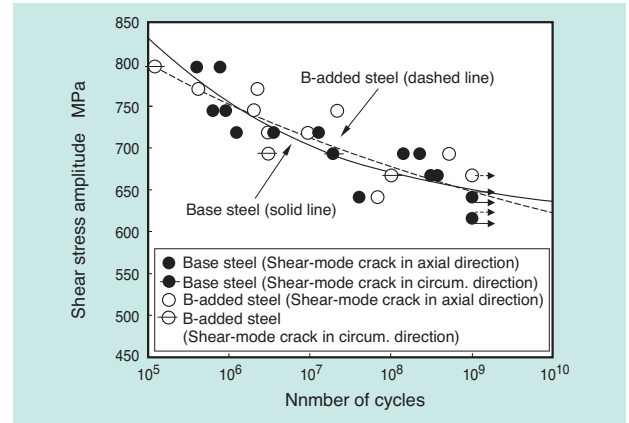


Fig. 3 Shear fatigue properties of Base and B-added steels evaluated by USTF tester

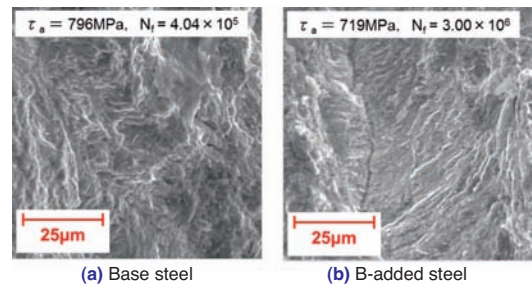


Fig. 4 SEM images of fracture surface at initial shear fatigue cracking

intergranular enhancement elements⁴⁾; its effect could not be confirmed since the fracture in these experimental conditions were transgranular.

3. Relationship between shear fatigue life and rolling fatigue life of bearing steels obtained by ultrasonic torsional fatigue testing.

3.1 Background

Shear fatigue properties of carbon steel for machine parts S53C and heat-resistant carburized steel M50NiL (AMS6278) were evaluated. In addition, we investigated the relationship between the shear fatigue properties and rolling contact fatigue (RCF) test results of these two steels and SUJ2 bearing steel²⁾ for which previous test results exist.

3.2 Test method

Table 1 shows the chemical contents of S53C and M50NiL, used for the USTF test samples Fig. 5 shows the cross section hardness distribution of the USTF samples at minimum diameter. To eliminate the impact of surface roughness, emery abrasion (#500 and #2000) and diamond wrapping (grain size of 1 µm) were applied for a mirror finish before the ultrasonic torsional fatigue test.

The diameter and length of the RCF samples were 12 mm and 22 mm, respectively.

Table 2 shows the number of lots, total number of samples, as well as the average, maximum and minimum hardness measurements of samples evaluated in the tests.

Table 1 Chemical compositions of S53C and M50NiL used for USTF specimens (mass %)

	C	Si	Mn	P	S	Ni	Cr	Mo	V
S53C	0.54	0.17	0.86	0.011	0.008	0.02	0.14	-	-
M50NiL	0.12	0.20	0.25	0.005	0.002	3.40	4.08	4.15	1.18

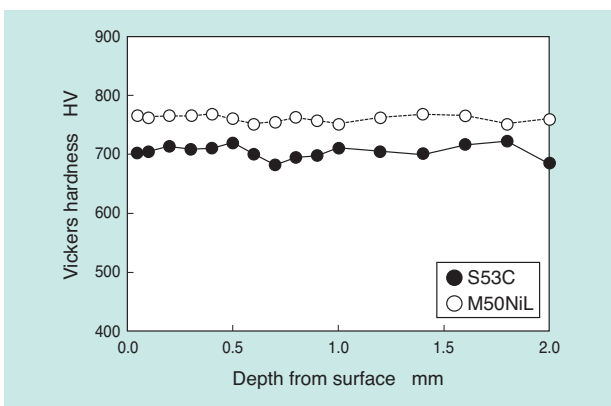


Fig. 5 Hardness distributions of S53C and M50NiL at minimum circumference of USTF specimens

Table 2 Number of lots, total number and hardness of RCF specimens

	Number of lots	Total number of specimens	Hardness (HRC)	
			Ave.	Min.~Max.
SUJ2	9	124	62.4	62.0~62.8
S53C	2	34	61.0	60.5~61.5
M50NiL	3	63	63.8	62.4~64.5

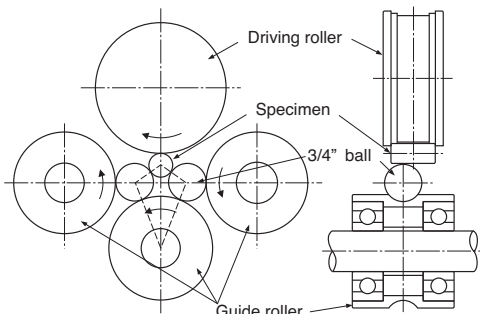


Fig. 6 Schematic of RCF tester

Table 3 RCF test conditions

Ball	3/4" (19.05mm)×2 made of SUJ2
Max. contact pressure	5.88 GPa
Loading rate	46240 c/min
Lubricant	Turbine oil VG68

The USTF test conditions are the same as those in Section 2.2. When there was no damage up to 1×10^{10} cycles, the test was terminated.

Fig. 6 shows the schematic diagram of the RCF test equipment and **Table 3** shows the test conditions. The samples are driven by the driving roller to cause rolling fatigue with the 3/4 inch steel balls in contact under high contact stress conditions. When damage occurs in the sample, vibration of the tester increases, which was used as the termination signal.

3.3 Results

Fig. 7 shows the shear fatigue properties of three types of steels, namely, the two steel types tested in this paper and SUJ2²⁾. S53C was the lowest both in fatigue strength at finite life and fatigue limit (442 MPa) among the three steel types evaluated so far. M50NiL was the highest both in fatigue strength at finite life and fatigue limit (680 MPa) among the three steel types. The slopes of shear fatigue properties of the three steel types were not significantly different within these fatigue strength cycles.

Table 4 shows the average, maximum and minimum values of 50% life of these three steel types in the RCF tests previously conducted. The overall performance of 50% life was S53C<SUJ2<M50NiL.

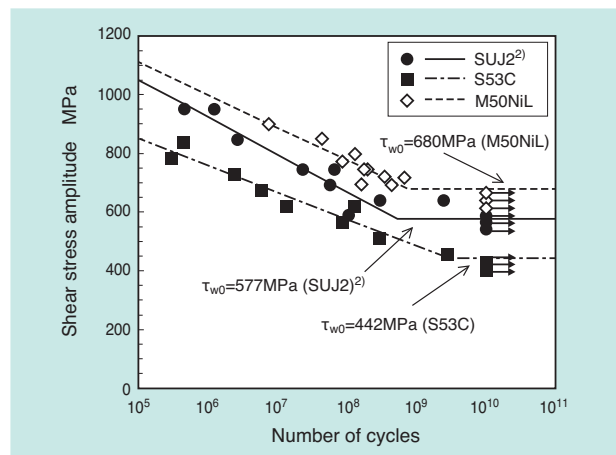


Fig. 7 Shear fatigue properties of three kinds of bearing steels evaluated by USTF tester

Table 4 RCF test results

	Number of lots	RCF life L ₅₀ (cycles)	
		Average	Minimum~Maximum
SUJ2	9	1.5×10^8	$8.5 \times 10^7 \sim 2.1 \times 10^8$
S53C	2	3.5×10^7	$3.3 \times 10^7 \sim 3.7 \times 10^7$
M50NiL	3	1.0×10^9	$7.3 \times 10^8 \sim 1.2 \times 10^9$

3.4 Observation

Fig. 8 shows shear fatigue life within finite life (fracture probability 50%) at a stress amplitude of 700 MPa of three steel types and rolling fatigue life L_{50} . A linear relationship was observed between the data sets.

Therefore, it was implied that the USTF test may become an alternative to the RCF test. That is, it could be an effective tool for determining relative superiority of RCF life.

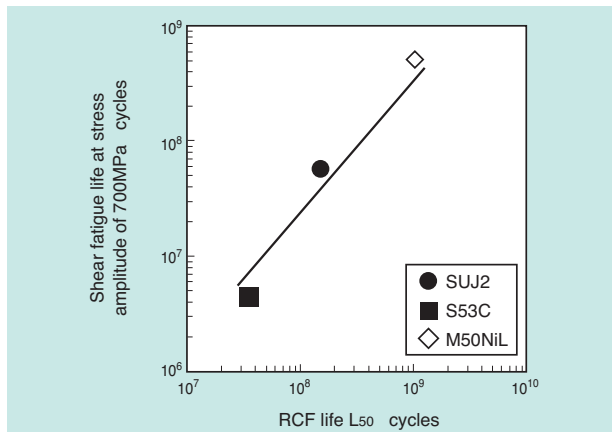


Fig. 8 Relationship between shear fatigue life and RCF life

4. Conclusion

Since torsional loads are applied repeatedly to the shafts of constant velocity joints, it is important to evaluate their shear fatigue properties. We evaluated shear fatigue properties of the materials with increased manganese on S40C (base steel) and boron (B) added on the base steel or its equivalent material up to 1×10^6 - cycle regimes with an ultrasonic torsional fatigue tester.

On the other hand, it is important to evaluate shear fatigue properties in order to determine rolling fatigue life, since alternate shear stress is considered to be one of the stresses governing crack generation and its initial propagation causing internal-originated damage of the rolling bearings. Therefore, we evaluated shear fatigue properties of carbon steel for machine parts S53C and heat-resistant carburized steel M50NiL (AMS6278). In addition, we investigated the relationship between shear fatigue properties and rolling fatigue life test results of three steel types including two steel types in this paper and bearing steel SUJ2 which had been previously evaluated.

(1) Fatigue properties of base steel with increased manganese to S40C and boron-added steel (fracture probability 10%) after 10^8 cycles were similar with 636 MPa and 643 MPa, respectively, exhibiting no difference in shear fatigue properties.

- (2) S53C was the lowest both in fatigue strength at finite life and fatigue limit (442 MPa) of shear fatigue properties among the three steel types evaluated. On the other hand, M50NiL was the highest both in fatigue strength at finite life and fatigue limit (680 MPa).
- (3) The slopes of shear fatigue properties of the three steel types were not significantly different within these fatigue strength cycles.
- (4) Linear correlation was found between shear fatigue life within finite life (fracture probability 50%) at stress amplitude 700 MPa and rolling fatigue life L_{50} from previous rolling fatigue testing.

This paper has been edited based on the original manuscripts⁵⁾ and⁶⁾. We thank the Iron and Steel Institute of Japan and Japanese Society of Tribologists, who gave us the permission to publish it.

References

- G. Lundberg and A. Palmgren: DYNAMIC CAPACITY OF ROLLING BEARING, Acta Polytechnica, Mechanical Engineering Series, 1-3, (1947) 5-58.
- Noriaki Sakanaka, Yukio Matsubara, Yoshinobu Shimamura, Hitoshi Ishii: Rapid Evaluation of Shear Fatigue Properties of Rolling Bearing Steels for Lifespans Up to Gigacycle Range, NTN TECHNICALREVIEW, No. 79, (2011) 104-110.
- H. Ishii, K. Yamanaka and K. Tohgo: GIGA-CYCLE FATIGUE STRENGTH IN SOME HIGH STRENGTH STEELS BY ULTRASONIC FATIGUE TESTING, Material Science Research International, Special Technical Publication-1, (2001) 59-63.
- M. Yamaguchi: FIRST-PRINCIPLES STUDY ON THE GRAIN BOUNDARY EMBRITTLEMENT OF METALS BY SOLUTE SEGREGATION: PART1. IRON (FE) -SOLUTE (B, C, P, AND S) SYSTEMS, Metallurgical and Materials Transaction A, 42, 2, (2011) 319-329.
- Sakanaka, Matsubara: Impact of Boron on Shear Fatigue Properties of Induction Hardened Medium Carbon Steels for Lifespans Up to Gigacycle Range, CAMP-ISIJ, 26, (2013)316.
- Miwa: Relationship Between Shear Fatigue Life of Bearing Steel obtained from torsional fatigue test and Rolling Fatigue Life, Tribology Conference 2013 Autumn Proceedings (2013-10) E6.

Photo of author



Noriaki MIWA

Advanced Technology
R&D Center

2013 “CHO” MONODZUKURI Innovative Components Awards Nippon Brand Award

Parallel Link High Speed Angle Control Equipment

Hiroshi ISOBE, Yukihiro NISHIO, Seigo SAKATA, Naoya KONAGAI, Hiroyuki YAMADA

1. Introduction

NTN developed Parallel Link High Speed Angle Control Equipment (hereafter, equipment) applying the special parallel link mechanism of rotational 2-degrees-of-freedom, and applied this equipment to grease dispensing. This equipment was recognized for its ability to achieve high speed and highly accurate positioning in a broad operating range, with an operating angle of 90° and angle of traverse of 360°, and received the 2013 “CHO” MONODZUKURI Innovative Components Awards Nippon Brand Award.

2. Background

The parallel link mechanism adopted in this equipment was originally developed as a constant velocity joint for automobiles, achieving high operating angle with a maximum of 90°. Aiming for applications other than automobiles, we continued developing this parallel link mechanism as angle control equipment by combining actuators with it, and with an innovative driving mechanism and control methods, we could achieve smooth operation of rotational 2-degrees-of-freedom plus high speed/high accuracy operations¹⁾⁻⁵⁾. Recognized for its high speed and superior operability, it is used in the grease application mechanism in the production lines of automobile parts, where reduced tact time and high reliability are required.

3. Implementation on grease application equipment

Fig. 1 shows the equipment developed for grease application, and Fig. 2 shows an example of grease application equipment configuration where a dispenser for contact-less application is attached to the tip of this equipment. In this configuration, the equipment moves the work on the XY stage and controls the behavior of the dispenser. It achieves high speed application of around 10 points per second and automates the grease application process on workpieces with

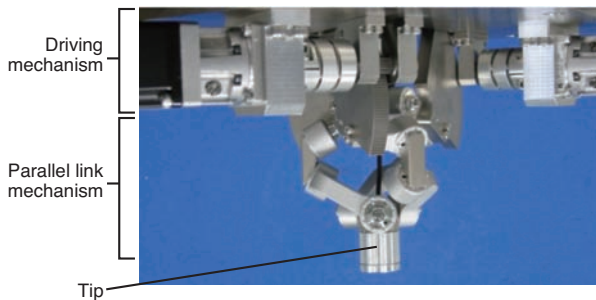


Fig. 1 Parallel link high speed angle control equipment

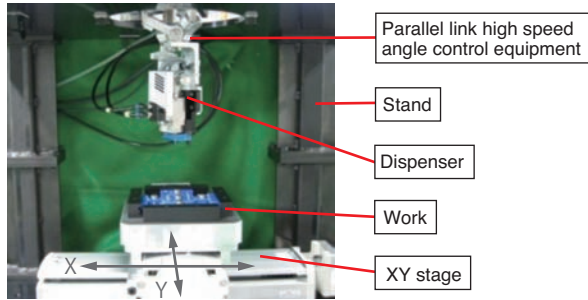


Fig. 2 System configuration example of grease dispensing

complicated shapes by enabling application at varying angles.

The equipment is capable of setting commanded angles by specifying XY coordinates on the operating stage, to facilitate teaching input tasks upon introduction into a new production line.

We hope that the equipment will be used in various fields such as medical, service, entertainment, etc. in addition to production facilities, and will contribute to further advancement of automation and robotization where Japan is competitive.

References

- 1) Keisuke Sone, Hiroshi Isobe, Koji Yamada: Wide Angle Active Link Equipment, NTN TECHNICAL REVIEW No. 71, (2003) 70-73.
- 2) Hiroshi Isobe, Yukihiro Nishio: Parallel Link High Speed Angle Control Equipment (PHACE), NTN TECHNICAL REVIEW, No. 80, (2012) 42-47.
- 3) Hiroshi Isobe: Parallel Link High Speed Angle Control Equipment – Basic Configuration and Application for Grease Dispensing, Machine and Tool, February Issue, (2013) 83-87.
- 4) Hiroshi Isobe, Yukihiro Nishio, Keisuke Sone, Hiroyuki Yamada, Yoshio Fujikawa: Parallel Link High Speed Angle Control Equipment, Proceedings of the Japan Society for Precision Engineering Spring Meeting in 2013, (2013) 809-810.
- 5) Hiroshi Isobe, Yukihiro Nishio, Seigo Sakata, Naoya Koganei, Hiroyuki Yamada, Yoshio Fujikawa: Parallel Link High Speed Angle Control Equipment—Implementation on Grease Application—, Proceedings of the Japan Society for Precision Engineering Spring Meeting in 2014, (2014) 1087-1088.

Photo of authors (presenters)



2013 Japan Powder Metallurgy Association, New Product Award in New Materials Division

Development of the Oil Seal Made of Sintered Metal for Variable Valve Timing Device

Yosuke SUGAI Toshihiko MOURI



1. Introduction

Variable valve timing devices for automobiles are used in various types of vehicles for fuel efficiency, processing of exhaust gas, etc. and demand is expected to increase particularly in the emerging markets.

Hydraulic variable valve timing devices are equipped with multiple oil seals, as shown in Fig. 1, to divide hydraulic chambers. Conventional oil seals are made of resin; however, we have developed oil seals made of sintered alloy and introduced them into the market. The characteristics required for oil seals are sealing capability and strength. If dimensional accuracy is not sufficient, oil may leak from the gaps with the surrounding components and affect the operating responsiveness of variable valve timing devices. Insufficient strength may cause deformation and damage to the devices.

The developed oil seals made of sintered metals received "The 35th Japan Powder Metallurgy Association, New Product Award in New Materials Division" which is awarded to superior new technologies in powder metallurgy. In this article, we present an overview of this development.

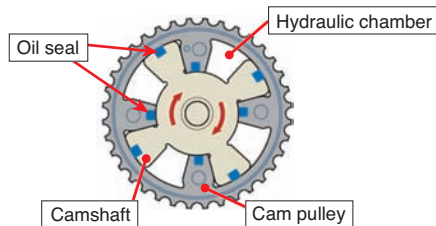


Fig. 1 Point-of-use of the oil seal

2. Features of the developed product

2.1 Good dimensional stability due to segregation-free processing

Ordinary ferrous sintered material, FG64, has unstable dimensional accuracy. This is due to segregation of graphite contained in the material which prevents proper flow of powder and leads to unstable compact weight during the molding process, resulting in reduced dimensional accuracy.

Therefore, we used ferrous powder and segregation-free processing to graphite to improve the powder flow and to stabilize the compact weight. This resulted in good dimensional stability.

2.2 Strength enhancement by mixing low-melting point metal

In order to ensure seal strength with sintered materials, a low melting point metal, tin (Sn), was selected and mixed in the optimum proportion. Since tin has good wettability with copper (Cu), when it is sintered below the melting point of Cu, it is diffused to facilitate bonding of ferrous powders, which improves strength of the sintered product.

Fig. 2 shows the comparison of transverse rupture strength as an index of the strength of seals.

Transverse rupture strength evaluates bend strength of the material by applying bending loads at three points on the test sample without cutouts. As a result, the developed material almost doubled in strength compared with the material made of resin.

2.3 Improved machinability and accuracy by optimized sintering conditions

In addition to the enhanced strength by adding low-melting point metals, we have added a sizing process to improve dimensional accuracy. This is possible by the optimization of the sintering conditions. Fig. 3 shows the dimensional accuracy. By ensuring the developed material made of almost only ferrite phase, we can achieve excellent sizing properties and required dimensional accuracy.

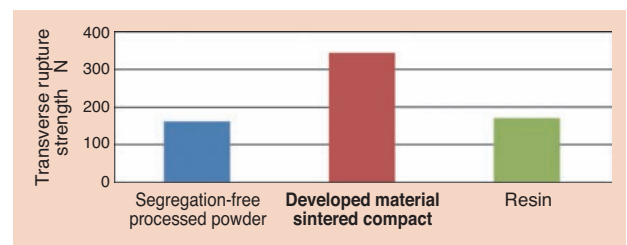


Fig. 2 Comparison of transverse rupture strength

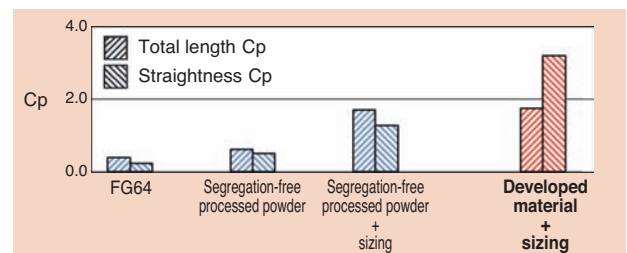


Fig. 3 Dimensional precision (Cp value)

3. Achieved results from the development

By using segregation-free graphite powder, the addition of tin and optimization of sintering conditions, we can achieve good dimensional accuracy and sealing abilities. We will continue our development of oil seals made of sintered metal to improve the function of variable valve timing equipment.

Photo of authors



Yosuke SUGAI

Engineering Dept.
NTN Powder Metal Corporation



Toshihiko MOURI

Engineering Dept.
NTN Powder Metal Corporation

2013 Japan Powder Metallurgy Association, Effort Prize

Sintered Hydrodynamic Bearing for Super Thin Fan Motor

Tadahiro UCHIYAMA Shinji KOMATSUBARA

1. Introduction

As mobile devices rapidly expand, the cooling fan motors used in these devices are becoming increasingly thin. The use of these devices is becoming much more diverse and the operating environment is also becoming much more challenging. Though the operating environment is becoming more challenging, the requirements for the bearings are to provide lower noise and more reliable operation than ever.

By leveraging high precision and high rigidity of the conventional sintered hydrodynamic bearings, we have developed sintered hydrodynamic bearings for super thin cooling fan motors (Fig. 1).

In this article, we present an overview of this product development, which received "2013 Japan Powder Metallurgy Association, Effort Prize."



Fig. 1 Appearance of sintered hydrodynamic bearing

2. Description of development

Sintered hydrodynamic bearings have a structure shown in Fig. 2. Sintered bearings have herringbone-like hydrodynamic grooves formed on the inner surface of the sleeve-shaped bearing rings where fluid lubrication film in the bearing clearance produces pressure (hydrodynamic pressure) by the rotation of the shaft to support the rotary shaft. In addition, as the material is the sintered alloy, lubricant is contained within the bearings resulting in a good anti-seizure property.

Fig. 3 shows an example of a super thin fan motor. The height of the motor is 4 mm and the length of the shaft must be 2 mm or less. When the length of the bearings is short, rigidity and supportive force are reduced; therefore, how to maintain bearing rigidity is the main challenge. We have focused on the specification of hydrodynamic grooves and their machining conditions. By optimizing the hydrodynamic grooves, we have succeeded in development of sintered hydrodynamic bearings for super thin fan motors with a shaft length of 2 mm or less.

2.1 Optimization of the hydrodynamic groove specification

As mentioned earlier, with shorter bearing length comes decreased bearing rigidity which may cause noise or short product life. Therefore, we created our own analytical program for theoretical analysis based on the rotor weight and motor structure, etc. which affect the bearing performance. We then optimized the design parameters such as hill/groove ratio of dynamic bearings, angle of groove and width of groove for super thin fan motors. We also conducted a verification test using motors to establish hydrodynamic bearing specification backed by theory and evaluation of the actual units in the early stage and significantly reduced the development and design time.

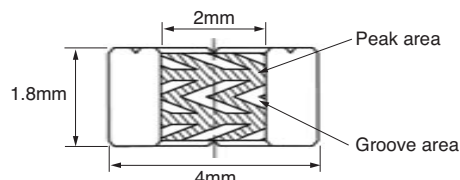


Fig. 2 Example of sintered hydrodynamic bearing

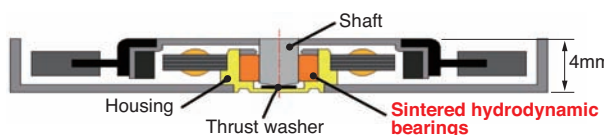


Fig. 3 Example of a super thin fan motor application

2.2 Optimization of the hydrodynamic groove machining conditions

In order to improve hydrodynamic bearing performance, we worked on higher precision molding for forming hydrodynamic grooves as a way to improve groove precision. We have optimized the hydrodynamic groove machining conditions for molding and also improved the molding precision. We also optimized hydrodynamic groove machining conditions for the bearings such as timing and machining margin during the dynamic groove machining process to obtain precise and stable groove depth and shape and enabled high precision machining of hydrodynamic grooves.

2.3 New development of lubricant oil

Due to the more severe operating conditions and property requirement, we also worked on improving the lubricant. We developed a lubricant oil which is appropriate for the bearings of super thin fan motors considering reduced rigidity in high temperature and increased bearing loss in low temperature, etc.

3. Conclusion

We have developed sintered hydrodynamic bearings for super thin fan motors by optimizing the design of the dynamic groove specification, optimized dynamic groove machining conditions and use of a newly developed lubricant oil. Its superior quietness and reliability were recognized and the bearings were widely adopted by fan motor manufacturers in Japan and abroad. These bearings are highly recognized by end users such as the PC manufacturers and expansion of further adoption can be expected.

Photo of authors



Tadahiro UCHIYAMA
Engineering Dept.
NTN Powder Metal Corporation



Shinji KOMATSUBARA
Fluid Dynamic Bearing Unit Dept.
Composite Material Product Division

2013 Japanese Society of Tribologists Effort Prize

Development of Ultrasonic Torsional Fatigue Tester for Rapid Shear Fatigue Property Evaluation of Rolling Bearing Steels

Noriaki MIWA

1. Introduction

As one of the stresses of rolling bearings governing crack generation before internal-originated flaking and its initial progress, we can point out almost completely reversed alternating shear stress acting repeatedly on the surface. The shear fatigue life can be obtained by torsional fatigue test. However, since the load frequency of the conventional torsional fatigue tester is low, evaluation up to the giga-cycle was practically impossible. Therefore, we developed an ultrasonic torsional fatigue tester (vibration frequency of 20000 Hz, completely reversed) aiming at rapid evaluation of the shear fatigue property of high strength steel for rolling bearings¹⁾. This achievement was published in the journal of Japanese Society of Tribologists, "Tribologist", and received the 2013 Japanese Society of Tribologists Effort Prize.

2. Production of ultrasonic torsional fatigue tester

Fig. 1 shows the configuration of the tester. The main components are a torsional vibration converter, amplifier and torsion amplitude magnifying horn. Since the rated output of the converter was small, the shape of the specimen and the amplitude magnifying horn needed to be adjusted. The specimen is dumbbell shaped and shear stress becomes largest on the surface of the smallest diameter area when torsional load is applied. Shear stress on the specimen is increased as the size of the specimen increases; however, resonance became unstable and we could not continue the test. Therefore, we limited the size of the specimen so that stable resonance is provided at up to 90% of the amplifier's output and increased the magnifying rate by improving the shape of the torsional magnifying horn so that high shear stress could be stably given.

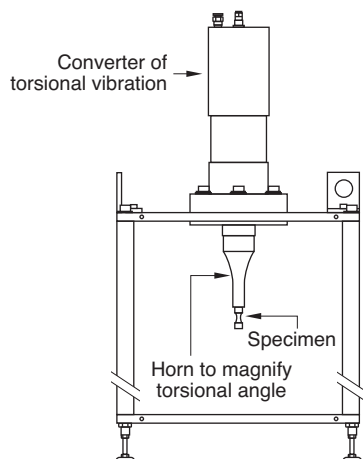


Fig. 1 Schematic of ultrasonic torsional fatigue tester

It is not possible to directly measure shear stress applied to the smallest diameter area of the specimen. Therefore, first we obtained the relationship between the maximum shear stress and torsional angle by FEM analysis, then the relationship between the amplifier output and torsional angle through experimenting, and finally, identified the relationship between the amplifier output and the maximum shear stress, to control the load stress.

3. Evaluation of bearing steel and estimation of fatigue limit contact pressure

Fig. 2 shows shear fatigue properties of SUJ2 up to giga-cycle regimes evaluated with the developed tester. We have devised an estimation method of fatigue limit contact pressure from the shear fatigue limit which is drawn from the obtained shear fatigue properties.

The fatigue limit contact pressure of SUJ2 estimated from the shear fatigue limit was almost identical with the ISO Standard.

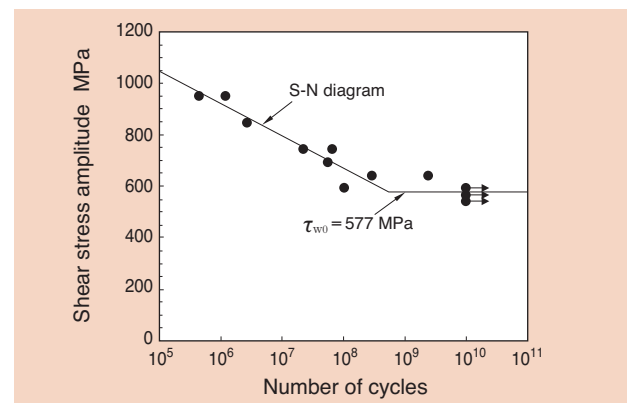


Fig. 2 Shear fatigue property of SUJ2 evaluated by developed tester

References

- 1) Miwa, Matsubara, Shimamura, Ishii, Tribologist, 58, (2013) 658-666.

Photo of author



Noriaki MIWA

Advanced Technology
R&D Center

Super Low Friction Hub Bearing

Significant reduction of hub bearing rotational friction during vehicle operation,
Results in approximately 0.3% improved fuel economy!



Features

33% reduction in bearing rotational friction (compared with the conventional units)

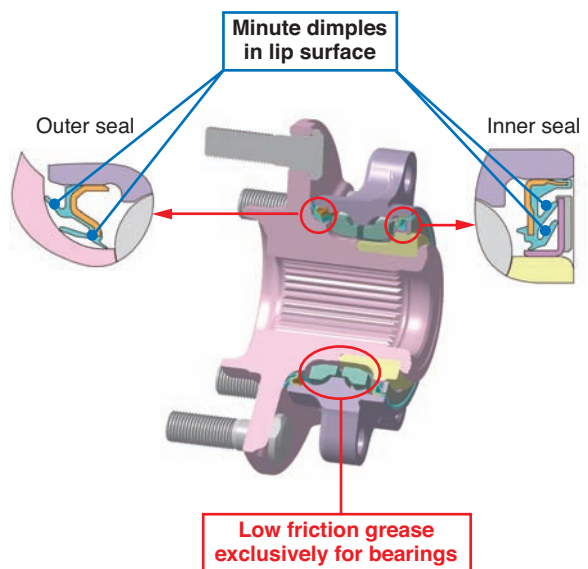
- (1) Newly developed low friction grease with improved ingredient composition and low viscosity made exclusively for bearings
- (2) Minute dimples implemented to the seal lip sliding surface

Applications

- Axles for passenger cars



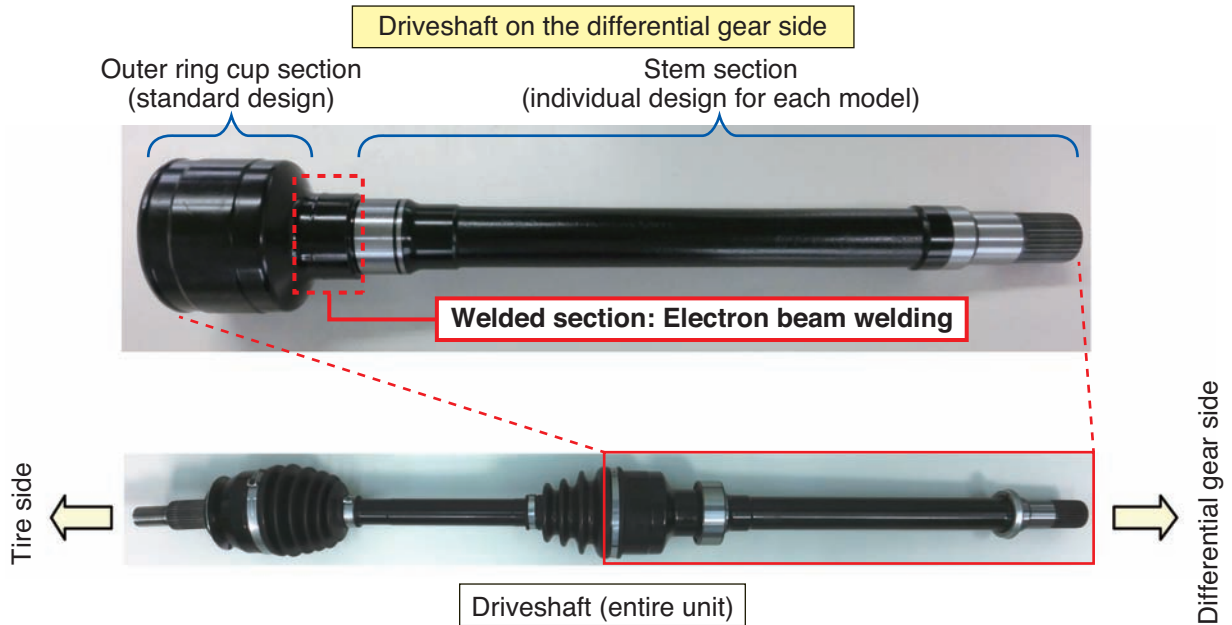
Structure



EBW Driveshaft

EBW : Electron Beam Welding

Contributes to shorter development lead time
for automobile manufacturers with an innovative new production method!



Features

Contributes to shorter development lead time for new models and higher reliability

- (1) Common outer ring cup section which had been different in vehicles in the past (only the stem is subject to individual designs)
- (2) Secure and high precision welding in a short time with electron beam welding

Applications

- Driveshafts for passenger cars



Structure

Characteristics of electron beam welding (compared with friction welding)

Item	Electron beam welding	Friction welding
Welding time	◎	○
Strength of welded section	◎	◎
Concentric accuracy of welded section	○	△
Secondary processing after welding	Not required	Required

◎Excellent ○Good △Fair

Low Section High Strength Press Pulley

By optimally shaping the design and improving press molding,
the industry's highest load resistance is achieved!

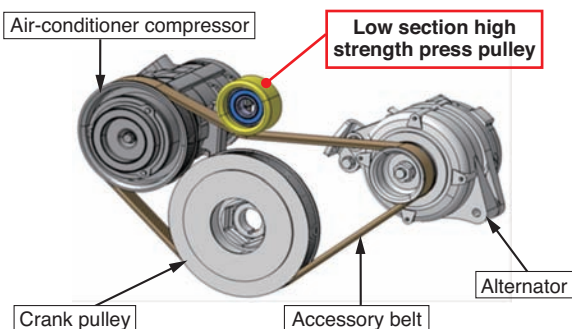


Features

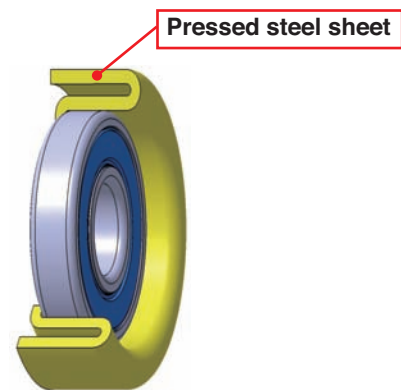
- (1) Steel sheets 1.5 times thicker than conventional press pulleys can be applied
 ⇒ **Improves the pulley load resistance by two times or more**
- (2) Low pulley section of approximately 70% of conventional products
 ⇒ **Improves bearing operating life and load capacity**
- (3) High durability under high temperature conditions and excellent wear resistance against foreign matters suitable for application in vehicles for emerging markets

Applications

- **Automobile engine accessory belt drive system**



Structure



- Optimal design achieved by utilizing analysis technology
- Improved press technology results in a reduced section and thicker sheets
- Revised thermal processing conditions for a stronger mold, preventing mold damage and seizure.

Long-life Needle Roller Bearing Unit

More than 10 times the operating life compared to conventional products with contaminated lubrication!



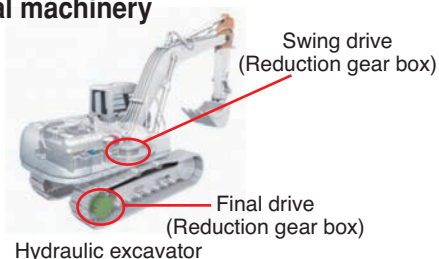
Features

Long-life roller bearing unit achieving more than 10 times the operating life with contaminated lubrication compared to conventional products

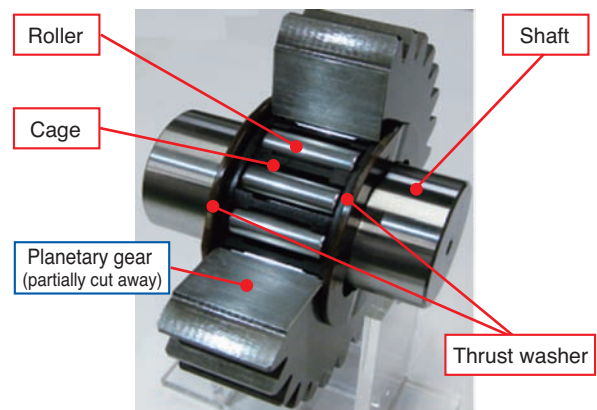
- (1) Special (heat treatment) for rollers and shafts for longer operating life with contaminated lubrication
- (2) Improved roller crowning shape to limit edge stress due to bearing installation error
- (3) Optimal design for the cage pocket shape to reduce introduction of contaminants
- (4) Added thrust washer discharge groove to improve contaminant discharge (oil discharge quantity: 6 times the conventional method)

Applications

- **Planetary reducers for construction and agricultural machinery**



Structure



Gear and bearing cut away
(planetary reducer)